TECHNISCHE UNIVERSITÄT WIEN
Vienna University of Technology

Diplomarbeit

Automated Evaluation for Corrosion Inhibitor Testing and All Solid–State Batteries With Doped Garnet–Type Electrolyte $Li_7La_3Zr_2O_{12}$

Ausgeführt am

Institut für Chemische Technologien und Analytik

der Technischen Universität Wien

unter der Anleitung von
Ao.Univ.Prof. Univ.Prof. Dipl.–Ing. Dr.techn. Wolfgang Linert
Ao.Univ.Prof. Dipl.–Ing. Dr.techn. Herbert Hutter

durch
Sabine Reither

Sparbach 3
2393 Sittendorf
Austria

Zusammenfassung

Diese Arbeit ist an der TU Wien und an der ETH Zürich entstanden und besteht daher aus zwei Teilen.

Der erste Teil wurde an der TU Wien durchgeführt und beschäftigt sich mit der Methodenverbesserung der Zyklovoltammetrie. Diese Methode wird für Tests der Inhibitorwirkung gegen Korrosion angewandt, um das Korrosionspotential und den Korrosionsstrom zu berechnen. Dazu müssen die gewonnenen Daten transformiert werden um den Tafel Plot zu erhalten und lineare Regressionen müssen an die Kurve gelegt werden. Dieser Prozess ist oft nicht einheitlich durchgeführt, da die Kriterien für die Regression nicht genau festgelegt sind.

Im Rahmen dieser Arbeit wurde daher ein Computerprogramm basierend auf MATLAB entwickelt, weches die einheitliche Auswertung übernimmt. Ein großer Vorteil dieser Automatsierung ist die dadurch erbrachte Zeitersparnis. Die Auswertung einer Messreihe mit zwei Zyklen konnte in weniger als einer Minute ausgewertet werden. Das erstellte Programm konnte sogar stark rauschende Signale verwerten.

Der zweite Teil der Arbeit wurde an der ETH Zürich durchgeführt und beschäftigte sich mit $Li_7La_3Zr_2O_{12}$ (LLZO), einem Feststoffelektrolyt mit Granat–Struktur. Durch Einbringen geringer Mengen an bestimmten Fremdelementen wie z.B. Ga kann die Struktur von tetragonal auf kubisch geändert werden. Die kubische Phase ist als Elektrolyt für Li–Ionen–Batterien sehr interessant, da sie Li–Ionen gut leitet.

Im Rahmen dieser Arbeit wurde an neuen Dotierungen geforscht und die erste funktionierende Batterie mit Feststoffelektrolyt hergestellt. Mit dieser Batterie wurde auch ein LED–Lämpchen zum Leuchten gebracht.

Summary

This work was executed at Vienna University of Technology and ETH Zürich. Therefore, it is split in two parts.

The first part was done at Vienna University of Technology and was dedicated to the method refinement of cyclic voltammetry. This method is used for corrosion inhibitor testing, especially for finding the corrosion potential and the corrosion current. First, the data needs to be transformed to get the Tafel plot. Next, the linear regression needs to be done. There does not exist an uniform method, therefore the regression might differ with the operator.

In this work a computer program based on MATLAB for data evaluation was developed. The big advantage is the saving of evaluation–time. A measurement with two cycles was evaluated in less than a minute. Even noisy data could be processed.

The second part of this work was done at ETH Zürich and was dedicated to the garnet–type electrolyte $Li_7La_3Zr_2O_{12}$ (LLZO). With the help of small amounts of doping, e.g. Ga, the structure could be changed from tetragonal to cubic. This cubic structure is interesting because of it high ionic conductivity for Li–ions. This phase can be used for the development of new all solid state Li–ion–batteries.

In this work new dopings were investigated. Furthermore, the first solid state battery was built and operated. This battery was also able to light a LED.

Contents

I. Method Refinement: Cyclic Voltammetry for Copper Working Electrodes **7**

1. Introduction **8**
1.1. Corrosion . . . 9
1.1.1. General Definitions and Reasons for Corrosion Science . . . 9
1.1.2. Thermodynamics and Kinetics . . . 10
1.1.3. Types of Corrosion . . . 12
1.1.4. Copper [1, p.1433–1452] . . . 13

2. Methodology **15**
2.1. Cyclic Voltammetry . . . 15
2.2. Making Electrodes . . . 16
2.3. Chemicals . . . 17

3. Results and Discussion **18**
3.1. Program for Evaluation of Data . . . 18
3.1.1. Flow Chart of the Tasks . . . 18
3.1.2. Generation and Transformation of Raw Data . . . 20
3.1.3. Extrema of Potential Data and Minima of the Tafel Plot . . . 21
3.1.4. Interpolation Areas, Interpolation and Point of Intersection(POI) . . . 25
3.1.5. Plotting of the Results . . . 27
3.2. Corrosion of Copper in Tap Water, NaCl and Ascorbic Acid Solutions . . . 29
3.2.1. Tap water . . . 29
3.2.2. NaCl . . . 34
3.2.3. Ascorbic Acid . . . 47
3.3. ZnO and 4–Methylimidazole as Corrosion Inhibitors for Copper . . . 54
3.3.1. ZnO . . . 54
3.3.2. 4–Methylimidazole . . . 61

4. Outlook **69**

II. Electrolyte for All Solid State Batteries **70**

5. Introduction and Background **71**
5.1. Historical Approach . . . 71
5.2. Lithium Lanthanum Zirconium Oxide (LLZO) . . . 73
5.2.1. Synthesis . . . 73

6. Methods and Materials **75**
6.1. Standard Work–flow . . . 75
6.1.1. Powder Synthesis . . . 75
6.1.2. Calcining . . . 76
6.1.3. Post–doping with Ga_2O_3 . . . 76
6.1.4. Pressing Pellets . . . 76
6.1.5. Pellet Sintering . . . 76
6.1.6. Pellet Preparation for Impedance Measurements . . . 76
6.2. Physical characterisation . . . 77
6.2.1. X-Ray Diffraction (XRD) . . . 77
6.2.2. Scanning Electron Microscope (SEM) . . . 77
6.2.3. Thermal Gravimetric Analysis (TGA) . . . 78
6.3. Electrochemical characterisation . . . 78
6.3.1. Electrochemical Impedance Spectroscopy) . . . 78
6.4. Chemicals . . . 80

7. Results and Discussion **82**
7.1. Sol–Gel Synthesis . . . 82
7.2. Na doped LLZO . . . 83
7.3. Calcium–Doped and Calcium/Gallium–Doped LLZO . . . 85
7.3.1. $Li_{7.2}Ca_{0.2}La_{2.8}Zr_2O_{12}$ . . . 85
7.3.2. $Li_{6.9}Ga_{0.2}Ca_{0.5}La_{2.8}Zr_2O_{12}$ . . . 88
7.3.3. $Li_6Ga_{0.5}Ca_{0.5}La_{2.5}Zr_2O_{12}$ . . . 89
7.4. Batteries . . . 95
7.4.1. $LiCoO_2$ as cathode material . . . 97
7.4.2. $LiFePO_4$ as cathode materials . . . 101

8. Conclusion and Outlook **104**

Part I.

Method Refinement: Cyclic Voltammetry for Copper Working Electrodes

1. Introduction

Copper is a metal with a long history of usage. The earliest evidence on usage was found in western Asia and dated back to 8000 B.C.E.[2] The reason for this was that copper was available in pure metallic form and was easily formed because of its low hardness. The Latin word cuprum derived from the large copper mines on Cyprus and translated as "Metal of Cyprus"[2].

The invention of the first copper alloy, bronze, marked a new age in history. The use of this material was important for military and cultural purposes. The invention of how to make iron not only from meteorites but also from ores, changed the material of weapons from bronze to iron and steel. Furthermore, copper was used for decorative and cultural reasons. The great comeback of copper occurred with the general understanding of electricity and the invention of electrical devices and wires. Copper has a high thermal and electric conductivity and can be formed easily. Till today copper is an important material and often can not be easily substituted by other metals [3].

Nevertheless, the corrosion of copper represents a major problem in the industry. In case of corrosion the copper metal dissolves to copper ions and electrons and can be re-deposited at places with high electric field strength. As a consequence metal depositions are formed leading to so–called dendrites.

In general copper is quite a noble metal with a standard electrode potential at 25 °C of +0.337 V [4, p.77] for the chemical reaction 1.1.

$$Cu^{2+} + 2e^{-} \rightarrow Cu \tag{1.1}$$

In this work the corrosion of copper should be minimized by selected additives. The main target is to define a standard method for testing the corrosion inhibition efficiency by cyclic voltammetry, which is a promising and often used analytical method in this field of study [5][6][7]. However, the main problem is that there is no standard procedure for the evaluation of the measurement data. Therefore, a program/code for an automatic data processing was implemented using MATLAB.

Values like the corrosion potential and the corrosion current were automatically calculated from the raw data by the use of Tafel plot to characterize the corrosion inhibition efficiency.

1.1. Corrosion

Corrosion of metals is a well-known phenomenon and occurs everyday varying in speed, mechanisms and visibility. The reason for this are the different chemical kinetics and mechanisms of the corrosion reactions. Especially the free reaction enthalpy is important to determine the direction of the viewed chemical reaction. Nevertheless, the free reaction enthalpy can not give a statement about the kinetics of the corrosion reaction.

1.1.1. General Definitions and Reasons for Corrosion Science

Our industry is based on the usage of a variety of materials, which should be chemically and physically stable for as long as possible. That this is not possible is well known from reality. The reasons for corrosion are numerous and are highly influenced by temperature and humidity often enhanced e.g. by the corrosive effect of the polluted air. For that reason it is very important to know the working conditions and the surrounding environmental influences of the usage of the material [8].

Corrosion describes a reaction at a phase boundary leading to damage of the material [9, p.1]. Normally, people think about metal corrosion when talking about corrosion. Even so, the definition of corrosion applies to all kinds of materials, like for example plastics or glass.

Corrosion is a chemical process that requires:

1. an anode reaction: $Me \rightarrow Me^{n+} + ne^{-}$ (Oxidation)
2. a cathode reaction: $Me^{n+} + ne^{-} \rightarrow Me$ (Reduction)
3. the electrolyte, in touch with both anode and cathode and therefore able to transfer the ion current
4. a conductive connection of anode and cathode for transferring electrons.

To inhibit corrosion, one of these four requirements need to be absent. This can be done for example by protective layers on the anode and/or cathode to separate the electrolytes from the corrosive electrolyte.

The general reaction equation of the anode is given in equation 1.2.

$$M \rightarrow M^{z+} + ze^{-} \tag{1.2}$$

Here, M, M^{z+} and e^{-} refer to the metal, the metal ion and the transferred electrons. The cathodic reaction is described in equation 1.3.

$$M^{z+} + ze^- \rightarrow M \tag{1.3}$$

Summarized, anodic reactions release electrons which are consumed by the cathodic reactions in the system.

As mentioned before, the free reaction enthalpy ΔG is important to determine in which direction a reaction takes place. It is connected to the electrode potential, E, shown in equation 1.4. Here F is the Faraday Constant.

$$\Delta G = -zEF?? \tag{1.4}$$

If the value of ΔG is nearly zero, the driving force of the reaction will be small to non-existent. If ΔG becomes a negative value, the reaction is called exergonic,i. e. a spontaneously occurring reaction. Reactions like the burning of fuels with oxygen to carbon dioxide and water or the rusting of iron are exothermic reactions. A ΔG which is positive characterizes an endergonic reaction [10].

1.1.2. Thermodynamics and Kinetics

Literature for this subsection were [11], [10], [12], [8] and [4].

One of the most important values in connection with the ΔG is the electrochemical potential $\tilde{\mu}$. It is defined by the equation 1.5.

$$\tilde{\mu} = \mu + zF\phi \tag{1.5}$$

μ is called the chemical potential or partial molar energy and is a form of potential energy that can be absorbed or released in a chemical reaction [13].ϕ is the is the local electrostatic potential. In case of an uncharged species, which means $z = 0$, the electrochemical potential has the same value as the chemical potential.

$$\nu_A A + \nu_B B + \cdots \rightarrow \nu_Z Z + \nu_Y Y + \cdots \tag{1.6}$$

$$\Delta G = \nu_Z \tilde{\mu_Z} + \nu_Y \tilde{\mu_Y} + \cdots - [(-\nu_A)\tilde{\mu_A} + (-\nu_B)\tilde{\mu_B} + \cdots] = \sum_k \nu_k \mu_k \tag{1.7}$$

Concerning equation 1.7 it can be seen in that ΔG is the sum of all $\nu_k \mu_k$ in case of considering the whole chemical reaction in 1.6 where the electrical charges of the involved phases do not change. In case of a single electrochemical half-cell this condition is not given while for a Daniell cell it is fulfilled.

The chemical potential can also be written as

$$\mu_k = \mu_k^0 + RT \ln A_k \tag{1.8}$$

with A_k as the activity of the component A. If 1.8 is inserted in 1.7, it leads to

$$\Delta G = \sum \nu_k \mu_k^0 + RT \ln \Pi A_k^{\nu_k} \tag{1.9}$$

and with

$$\sum \nu_k \mu_k^0 = \Delta G^0 \tag{1.10}$$

where ΔG^0 is called free standard-state free energy of formation. So ΔG is also defined by

$$\Delta G = \Delta G^0 + RT \ln \Pi A_k^{\nu_k} \tag{1.11}$$

The electrode potential can be calculated combining equation 1.4 and 1.11:

$$E = E^0 - \frac{RT}{zF} \ln \Pi A_k^{\nu_k} \tag{1.12}$$

Equation 1.12 is a form of the Nernst equation and makes it possible to calculate the value of E at different temperatures and concentrations. The concentration is mathematically connected to the activity by a linear equation with the activity coefficient as proportional coefficient. The standard electrode potentials (E^0)are measured against a defined reference potential (0 V) i.e. the potential of the standard hydrogen electrode (SHE) at 25 °C. Table 1.1 gives a selection of some standard electrode potentials.

Table 1.1.: Some standard electrode potentials at 25 °C (part of table in [4, p.77])

Electrode	Standard electrode potential vs. SHE
$Au^{3+} + e^- = Au$	+ 0.771
$Cu^+ + e^- = Cu$	+0.520
$Cu^{2+} + 2e^- = Cu$	+ 0.337
$2H^+ + 2e^- = H_2$	0.000
$Fe^{2+} + 2e^- = Fe$	–0.440
$Zn^{2+} + 2e^- = Zn$	–0.763

Metals like copper with positive standard electrode potentials are called noble metals, while metals with negative potentials like zinc are called ignoble metals.

A form of graphical presentation of thermodynamic data is the Pourbaix diagram, also called potential-pH diagram. The Pourbaix diagram is used in corrosion science, electrodeposition, geological processes and hydrometallurgical extraction processes representing the relative stabilities of solid phases and soluble ions in aqueous environment [4, p.78]. A typical Purbaix diagram is shown in Figure 1.1. The two parameters given in the Pourbaix diagram are the electrode potential (E) on the y–axis and the pH of the

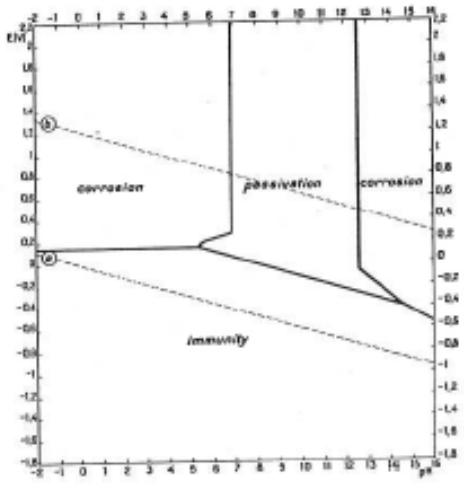

Figure 1.1.: Domains of corrosion, immunity and passivation of copper, at 25 °C [14].

environment on the x–axis.

Three important areas can be seen in these diagrams:

1. In the area of immunity, no corrosion occurs due to a stable species of the metal.
2. The second area describes the corrosion of the metal. Here, soluble ions form.
3. When an insoluble solid reaction product is stable (e.g. oxides) and forms a layer on the metal, the metal is protected. This area is called passivity.

The temperature dependence of the kinetics of a corrosion process can be described by an Arrhenius's equation:

$$r = A \exp \frac{-\Delta G^*}{RT} \tag{1.13}$$

Here, A is a constant and ΔG^* is the activation energy. If equation 1.4 is applied, and r is exchanged with i, the electric current, then equation 1.14 is obtained:

$$i = k \exp \frac{-\Delta G^*}{RT} = k \exp \frac{zFE^*}{RT} \tag{1.14}$$

The constant A has changed in the process and instead there is a new constant k.

1.1.3. Types of Corrosion

Theoretically uniform corrosion should occur on solids, but in reality selective corrosion of small areas is common [15]. Macroscopically seen, the corrosion happens on the whole

surface with the same corrosion rate. In reality, the macroscopically flat surface is finely structured. Therefore, local corrosion takes place.

The reasons for this selective type of corrosion are either differences in the electrolyte like pH value or the concentration of dissolved oxygen or some local defects in the metal. Normally there are lots of grains and face boundaries, since industrially used metals are normally not in the form of a perfect single crystals.

Two well–known types of local corrosion are shallow corrosion and pitting corrosion.

Both types are related to contact corrosion. It occurs often if metals have a noble metal coating. If the coating is damaged, the noble metal coating will act as the cathode and the non–coated metal acts as the anode. Because of the huge cathode and the small anode formed, a huge driving force for corrosion between both occurs. This leads to the formation of holes.

The ratio of the depth to the diameter of the hole decides the name of the corrosion type. For swallow corrosion the diameter is huge and the depth is small, while it is the other way for pitting corrosion [15].

Another way to group corrosion phenomena is at which pH–Value they occur.

Acid corrosion happens when a solid and clean metal is attacked by a non-oxidizing acid. In this case the metal starts to dissolve. During this process hydrogen gas develops [9, p.122].

In neutral or alkaline environment combined with the precence of dissolved oxygen, oxygen corrosion occurs. The oxygen is reduced and corrosion products of the metal are formed [9, p.134-135]. This corrosion products can form protection layers on top of the metal.

1.1.4. Copper [1, p.1433–1452]

Like mentioned above copper is a metal with high electronic and thermal conductivity. It is quite noble but can react easily with other elements, i.e. with oxygen, over time. In fact, there is always a thin copper oxide layer on the top of the copper metal under normal environmental conditions.

When copper reacts with oxygen two different kinds of oxides can be formed, depending on the oxidation state of the copper. Both forms are insoluble in water but soluble even in light acids and in ammonia–containing solutions due to copper–ammonia complexes. With hydroxides copper forms a blueish, fluffy solid ($Cu(OH)_2$). One of the two possible oxides of copper is Cu_2O. Cu_2O is a orange to brown coloured solid with a cubic crystal structure It is a semiconductor with a band gap of around 2 V. The other

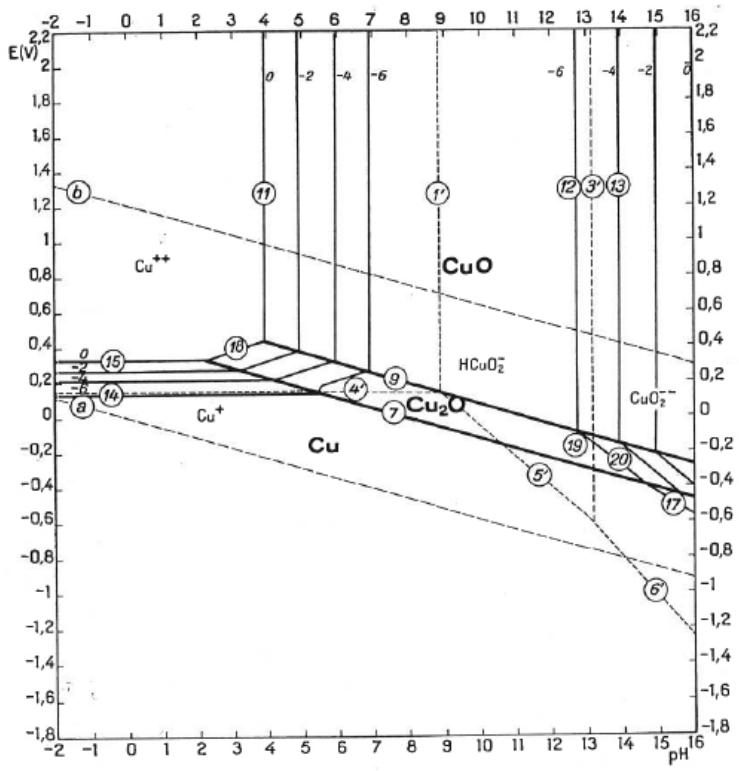

Figure 1.2.: Potential–pH equilibrium diagram for the system copper–water at 25 °C.

oxide of copper is CuO. CuO is a black solid with a monoclinic crystal structure. It is used as a catalyst or as an electrode in batteries or is also taken as a pigment.

The Figure 1.2 shows a potential–pH equilibrium diagram considering Cu, Cu_2O and CuO in water. From the data of this figure the zones of immunity (Cu), corrosion (Cu–ions) and passivation (Cu–oxides) can be found.

2. Methodology

2.1. Cyclic Voltammetry

The method chosen to investigate the corrosion characteristics of copper in a corrosive medium was cyclic voltammetry. In corrosion science this technique is a standard method to gather information about corrosion systems and is often supplemented by impedance spectroscopy. Other applications for cyclic voltammetry in chemistry are the study of chemical reactions to gain information about the stability of intermediate and final products, reversibility and electron transfer kinetics or to get substance specific information like formal reduction coefficient or diffusion coefficient [8].

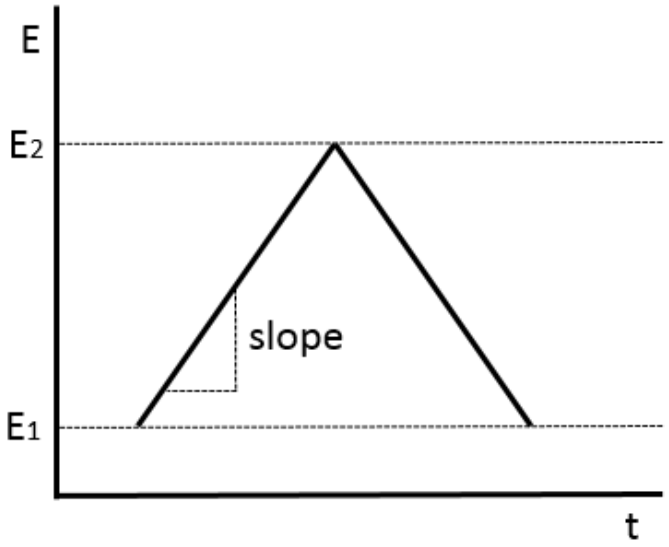

Figure 2.1.: Schematic representation of a typical potential cycle between two selected potentials (E_1 and E_2).

For the cyclic voltammetry experiment a potential is applied to the working electrode which changes over time. The current is recorded and afterwards often normalised by the area of the electrode. This helps to compare the results of different experimental set–ups. The potential applied to the working electrode cycles between at least two values with a given slope, like shown in Figure 2.1. The boundary potentials (smallest and highest

applied potential (E_1 and E_2)) have to be chosen carefully.It is essential that these selected potentials include the potentials for the relevant electrochemical phenomena.

Also, the slope has to be chosen with consideration. There can be huge differences in the results measured with different voltage sweep rates. The voltage sweep rate affects the reaction of the sample greatly, so it is important to measure at different rates or already know the system well enough to choose the right sweep rate for the experiment.

Cyclic voltammetry also has special requirements for the reaction itself and the electrolyte solution. Most of the theory used in voltammetry is based on completely reversible reactions. If the investigated reaction is not reversible, the theoretical approach has to be a different and more difficult one. It is also a common practice to use a so–called support electrolyte to negate the influence of outer electrical fields on the experiments. A support electrolyte is a electrolyte with a lot of ions.

For the evaluation of the data the operator needs a lot of experience. Recently powerful simulation programs were developed to understand the processes in detail. Nevertheless, a profound knowledge and understanding of corrosion is needed to perform a reasonable interpretation.

In this master thesis the behaviour of copper in different electrolytes and voltage sweep rates (10 mv/s and 20 mV/s) were examined in the voltage range of -1.8 to 1.3 V. The recorded current profile was measured against the Hg/Hg_2SO_4 reference electrode. To get insight into the influence of the dissolved oxygen concerning copper corrosion, the experiments were performed with and without dissolved oxygen, i.e. purging with nitrogen, in the solution.

2.2. Making Electrodes

The working and the counter electrode were self–made. The following process was used to prepare the electrodes:

- The first step is to clean a piece of wire of the selected material from organic compounds. Therefore, the wire was heated in a flame.
- For the platinum counter electrode at least half of the platinum wire is wrapped around a steel wire. For conductivity, the wires were connected with a silver paste.
- The wires are molten in a glass capillary in a way, that the electrode material is strongly embedded in a thin layer of glass at one side. For the platinum wire the embedded side has to be the one where only platinum is present.

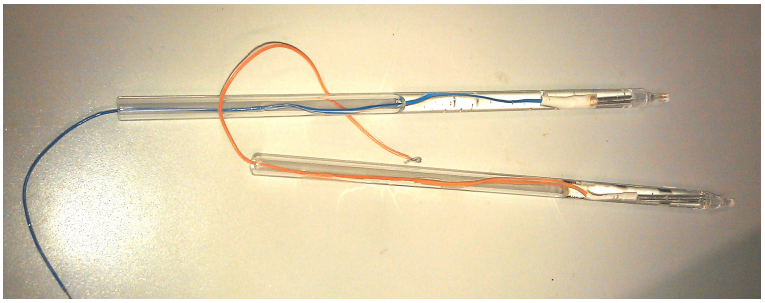

Figure 2.2.: Image of two self–made electrodes.

- The copper wire and the steel wire are connected to a long isolated wire on the end opposite to the glass embedding. The connection is fixated by soldering and sheathed by a shrink sleeving.
- The whole wire construction is embedded in a glass tube using the EpoFix Resin and EpofixHardener (25:3 mixing ratio).
- The electrodes are smoothed and honed using sand paper, grade P4000.

The electrodes are shown in Figure 2.2.

2.3. Chemicals

- **EpoFix Resin**
  Contains: Bisphenol–A–epichlorhydrin, epoxy resin (number average molecular weight $\leq$ 700), oxirane, mono[(C12–14–alkoxy)methyl]derivs.
  (Struers)
- **Epotix Hardener**
  Contains: Triethylentetraamin, 2–(2–Aminoethylamino)ethanol
  (Struers)
- **Zinc oxide** (98%)
  CAS–No.: 1314–13–2
  (Alfa Aesar)
- **4–Methylimidazole** (98%)
  CAS–No.: 822–36–6
  (Alfa Aesar)
- **Ascorbic acid**
  CAS–No.: 50–81–7

3. Results and Discussion

3.1. Program for Evaluation of Data

In corrosion science the point of intersection in the Tafel plot from measurements of cyclic voltammetry is an important characteristic value which holds both, qualitative and quantitative information. Therefore the point of intersection is used for comparing different materials in reference to their corrosion resistance or for the characterisation of corrosion inhibitors. It is crucial to find this characteristic value in a reproducible way. Furthermore, it is important to make sure there is an experimental set–up to allow the same edge conditions, as well as the same processing and evaluation of the data recorded from the measurement. Many different ways to process data are found in literature. For the data processing computational methods are preferred, due to the fact that a computer program works with strict criteria for data processing, ensuring the reproducibility of the task and minimizes the time for data processing.

The first step to program a code for processing the measurement data is to choose a suitable programming language. Programming languages like Python [16] or C# [17] are widely-used and powerful tools. The user needs to be aware of many concepts of programming, i.e. the assigning of storage space for variables. The output of the data in form of pdf-files or images also need some knowledge. An easier way for beginners in programming a code is the use of MATLAB which is the short form of 'Matrix Laboratory'. The program written in MATLAB can be used by either typing the program name in the control window of MATLAB or by opening the program in MATLAB and pressing the 'Run'–Button. Because of the easy use, MATLAB is taken as the program for processing the recorded data measured by cyclic voltammetry. Another advantage of this program is the simple translation of the implemented MATLAB code to a Python or C# program.

3.1.1. Flow Chart of the Tasks

The operating principle of the implemented MATLAB code is shown in Figure 3.1. The working tasks of loading the raw data and calculating the characteristic value of the point of intersection due to the Tafel Plot have been simplified using smaller tasks.

The first draft of the flow chart is shown in Figure 3.1 where the task of the program is separated into six smaller tasks: Getting the raw data from the file, transforming y–axis to obtain the Tafel Plot, finding the minimum value of the Tafel Plot, defining the area of regression, calculation of the point of intersection and the data output in form of plots

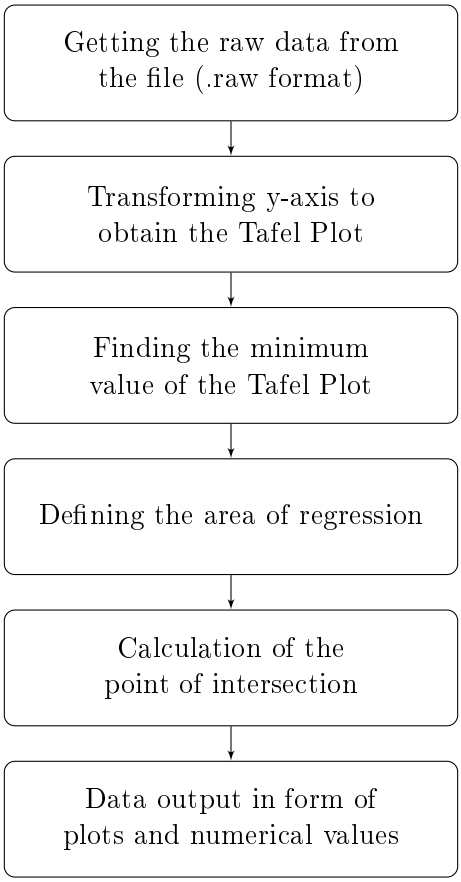

Figure 3.1.: Tasks to be performed.

and numerical values.

The beginning is the acquisition of the raw data to the local memory of the program. Furthermore, the name of the measurement file should be saved for the labelling of the output data and the plots. As a result they are clearly assigned to the input data.

The second step should be the transformation of the data in a way that the Tafel Plot can be used for data analysis. Within this step the potential versus the $Hg/HgSO_4$ reference electrode has to be transformed to the potential versus normal hydrogen electrode. This is an important step to easily compare the results from other working groups in the literature [18][7][5].

For making the data processing reproducible, the criteria for choosing the areas of data for the regression have to be always the same. The idea for this program was to find the absolute minima in the Tafel plot in every cycle (means the zero–point in the

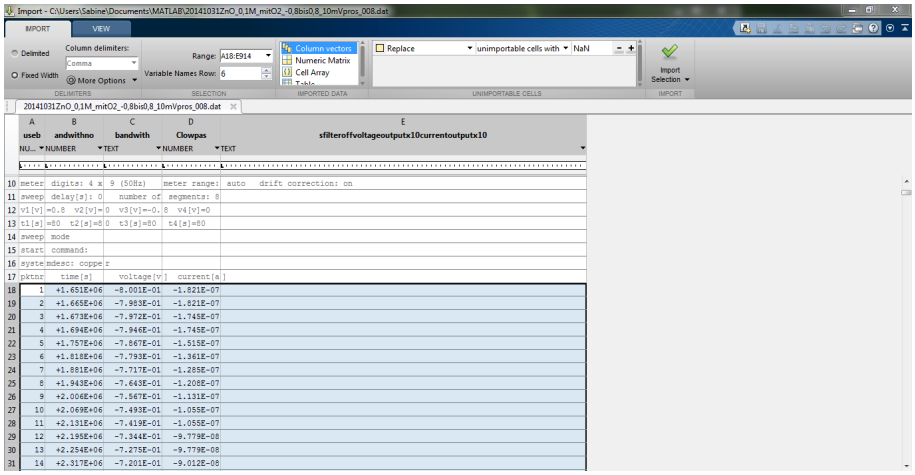

Figure 3.2.: A characteristic .dat file opened with MATLAB's import data function

non–transformed data). This minimum is used as a point of origin for finding an area with a certain distance to both sides of this point. Here, the area of 10 to 80 mV to both sides of the point of origin were chosen. In this area, there is no influence from diffusion. This kind of formulation has the advantage of a stable program, even when measurement conditions change. It is not dependent on the number of data points. however, there is one disadvantage: If there are only two points in the desired area, the regression is done only with these two points.

After the regression is done, the point of intersection of the chosen regression lines have to be selected, which can be done by simple math. The results are the corrosion potential and the corrosion current. Furthermore the resulted slopes of the regression lines give information about the behaviour of the inhibitor (anodic or cathodic). The corrosion current gives information on the corrosion rate.

The final task is the output of the archived information in form of plots and a tabular or a text file. For this thesis the program should be able to show the points of intersection and the regression lines in Tafel plots with the transformed data.

3.1.2. Generation and Transformation of Raw Data

The raw data is provided in the file format of .dat with some header lines describing the information about the measurement and the data in form of space–separated numerical values. 3.2 symbolically shows a characteristic .dat file opened with the import data function of MATLAB. For the implemented code the processes of opening the raw data and saving the raw data to the local memory should be done automatically. For this task the used code is shown in Listing 3.1.

Listing 3.1: Getting the data from the raw data file

```
fid = fopen(filename);
data = importdata(filename, ' ', 17);
fclose(fid);
xdata = data.data(:,3);
ydata = data.data(:,4);
```

Listing 3.2: Getting the path of the file

```
[FileName, PathName] = uigetfile('*.dat', 'File Selector');
filename = [PathName FileName];
```

For processing of the raw data, the file has to be opened by the program described by the first line of the code. Here, the file *filename* is opened. If the file of the raw data is saved in the same folder as the program, the name of the file will be sufficient for opening. Otherwise the path where the file is found has to be included too. Due to the fact that the file of raw data normally is not saved in the same folder as the MATLAB program, the task mentioned above is done with the code shown in Listing 3.2. With the command *uigetfile* it is possible to choose a file from the computer in a simple way.

After selecting and opening a file, the data is imported by the *importdata* command (second row of Listing 3.2). Here, the separator is specified (in this case just a space) and the number of headlines has to be given (here it is 17). The data is saved as the variable *data*. Then the file is closed again with the next command *fclose(fid)*. The values for potential are named *xdata*, while the current is named *ydata*.

The potential of every data point is transformed by adding 0.65. This transformation of the raw data changes the potential of $Hg/HgSO_4$ to the one versus NHE (Normal Hydrogen Electrode). The y–axis in the Tafel plot shows the logarithmic current per area. Therefore, the data is first divided by the area of the working electrode followed by the logarithm from the absolute value of the result. The code is given in Listing 3.3– the first line of the code transforms the potential, the second line transforms the current. The electrode is shaped as a circle. Therefore the area of the electrode is easily calculated by the formula $(d/2)^2 * \pi$. Here, d refers to the diameter (0.0125 cm).

Listing 3.3: Data Transformation

```
U = xdata + 0.65;
Ii = log(abs(ydata/((0.0125/2)^2*pi)));
```

3.1.3. Extrema of Potential Data and Minima of the Tafel Plot

Like mentioned above, it is important to find the minima of the Tafel plot. This operation is easy for the human operator by plotting the data and finding the minima. For

the computer, this process needs to be translated in a more systematic process.

When people look at the data of cyclic voltammetry measurements, they normally have more than one cycle and they normally look at the minima of every single cycle. Due to the face that measurement effects like random noise cause many minima, the random noise has to be eliminated by smoothing the raw data (see Listing 3.4).

Listing 3.4: Smoothing the raw data and transforming it afterwards

```
iN=15;
In = conv(ydata,ones(iN,1)./iN,'same');
Itrans = log(abs(In/((0.0125/2)^2*pi)));
```

The smoothing is done by a convolution corresponding to the polynomial multiplication. In MATLAB the command *conv* is used. The word *'same'* in the brackets means that the resulting vector should have the same length as the first vector. In this case *ydata* is entered.

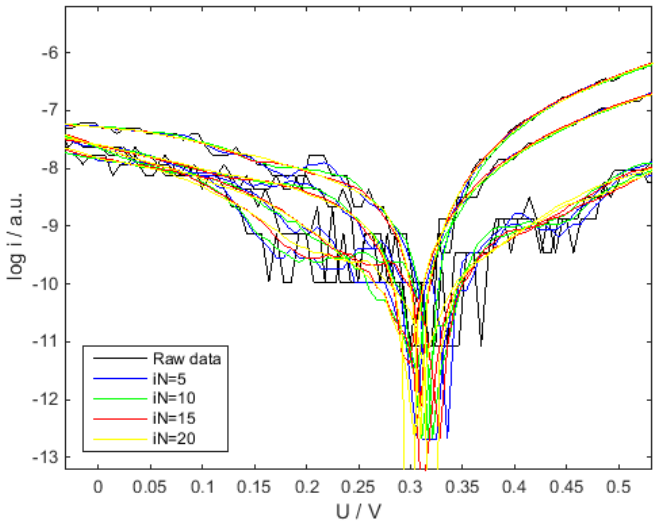

Figure 3.3.: Tafel plot with raw data and smoothed data with different iN.

Figure 3.3 shows a zoom into a Tafel plot. The raw data and the smoothed data with different iN(5, 10, 15, 20) are plotted. iN is the size of the multiplication vector. It can be seen easily that a small iN leads to little smoothing. Nevertheless, the data is close to the raw data. High value of iN leads to an extremely smooth curve and a loss of chemical information of the raw data. In this work the optimum value of iN turned out to be 15.

Afterwards, for separating the cycles, the position (means number of data point) of

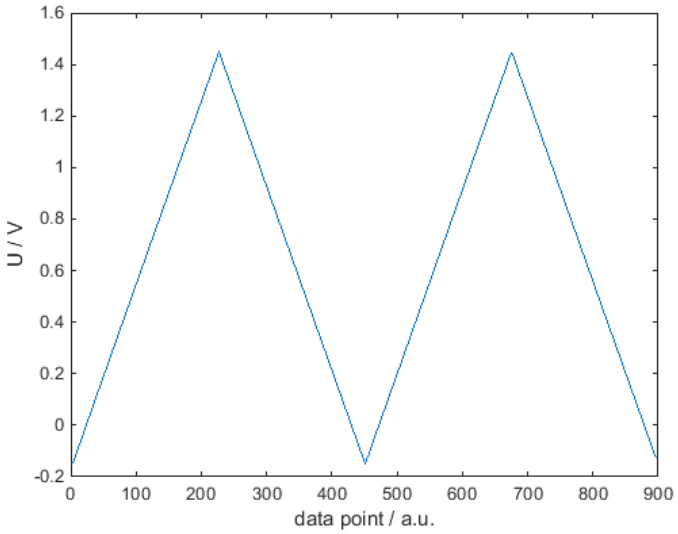

Figure 3.4.: The Potential which changes linearly during the measurement. The slope between the extrema is strictly monotonic – normally a characteristic for cyclic measurements in voltammetry.

the extrema of potential have to be found. This is done by the code given in Listing 3.5.

Here, the position in the data array, the value of the potential at the extrema and the corresponding current per area of the smoothed curve are obtained in the matrix C. Additionally, the first and the last point of the data should be included in the matrix C. The first three lines of the code insert the first measured data point in the matrix C. The last three lines add the last point in the raw data at the end of the matrix C. The construction of the for–loop coupled with the if–condition is used to find the local maxima of the curve. This is possible due to the fact that the slope between the maximum and minimum values of the applied potential is strictly monotonic. This is shown in Figure 3.4. Figure 3.4 shows the value of the applied potential plotted over the number of the data point.

Listing 3.5: Code for finding Extrema of Potential

```
az=length(U);
n1=1;
C =[1,U(n1),Itrans(n1)];

for k = 2:1:length(U)-1
    if (U(k-1)<U(k) && U(k)>U(k+1)) || (U(k-1)>U(k) && U(k)<U(k+1))
        n1 = n1+1;
        C(n1,1) = k;
```

```
        C(n1,2) = U(k);
        C(n1,3) = Itrans(k);
    end
end

C(n1+1,1) = az;
C(n1+1,2) = U(az);
C(n1+1,3) = Itrans(az);
```

The k in Listing 3.5 describes as the counter number repeating the for–loop. k is set from *2* to *length(U)-1* with the step size 1. The data value before and after the chosen value have also to be considered, therefore the boundary values have to be considered separately. This is done by adding them to the matrix separately.

The slope between the desired extrema is either strictly monotonic increasing or decreasing. The if–condition checks exactly this condition. If an extremum is identified, the desired values (position, potential and current of the smoothed curve) will be written in the matrix C.

This receiving matrix is used afterwards in the Code of Listing 3.6. Here, the raw data is separated into different pieces of data to find the absolute minimum in the Tafel plot. Like before for Listing 3.5 a counter number and a matrix for calculating the defined results are initialised. Afterwards a for–loop is used to find the desired values and write the identified values in the matrix. This matrix is named *Min*. In the matrix *Min* three values are recorded. The first value describes the index where the minima is found in the whole set of the data. The second value describes the corresponding potential. The third is the value of the smoothed current at the minimum. After this step all important values for the interpolation are received from the raw data.

Listing 3.6: Finding minima in the smoothed data for the Tafel plot

```
c = 1;
Min = zeros(c,3);

for k = 2:1:length(C)
    e = C(c);
    f = C(c+1);
  [M,I] = min(Itrans(e:f));
  Min(c,1) = I+e-1;
  Min(c,2) = U(I+e-1);
  Min(c,3) = M;
  c = c+1;
end
```

3.1.4. Interpolation Areas, Interpolation and Point of Intersection(POI)

The interpolation areas are chosen to be on both sides of the minimum in the distance of around 0.01 to 0.08 V. Note that this area is normally not affected by diffusion. However, it is greatly affected by changes of the surface. This effect is not included in the data processing, since the exact area of the surface in each cycle is not known. Furthermore, the chemical composition of the surface can be changed during the experiment. This leads to a deviation of the points of intersection of the different cycles among each other and should be kept in mind when interpreting the results.

Listing 3.7: Code for defining the corner points for the interpolation area

```
for k = 1:1:length(Min)
    if abs(U(1)-U(Min(c,1)))>0.08 && abs(U(length(U))-U(Min(c,1)))>0.08
        d =1;
        while abs(U(Min(c,1))-U(Min(c,1)-d)) < 0.08
            d = d+1;
        end

        reg(e,1) = Min(c,1)-d;
        reg(e,2) = U(Min(c,1)-d);
        e = e+1;

        d = 1;
        while abs(U(Min(c,1))-U(Min(c,1)-d)) < 0.01
            d = d+1;
        end

        reg(e,1) = Min(c,1)-d;
        reg(e,2) = U(Min(c,1)-d);
        e = e+1;

        d =1;

        ...
```

The code Listing 3.7 is the first part of the structure to find the corner points of the interpolation. It is done with a combination of for–loops as well as if– and while–conditions. It works as an iterative search until the given condition is not fulfilled. Then the position of the value in the original matrix and the value itself are saved to a matrix called *reg*. The matrix *reg* is used for the interpolation. Using the above mentioned way, the code is resistant to little changes in the starting point. Listing 3.8 describes the interpolation of the data over the defined areas.

Listing 3.8: Interpolation over the defined areas.

```
for  k = 1:1:(length(reg)/2)
    x = U(reg(c):reg(c+1));
    y = Itrans(reg(c):reg(c+1));
    p = polyfit(x,y,1);
    Fit(d,1) = p(1);
    Fit(d,2) = p(2);
    yfit = p(1) * x + p(2);
    yresid = y - yfit;
    SSresid = sum(yresid.^2);
    SStotal = (length(y)-1) * var(y);
    rsq = 1 - SSresid/SStotal;
    Fit(d,3) = rsq ;
    XFIT{1,d} = x;
    XFIT{2,d} = yfit;
    XFIT{3,d} = y;
    c = c+2;
    d = d+1;
end
```

The interpolation is implemented with the *polyfit*–command. This command is already implemented in MATLAB. The *polyfit*–command should perform as a linear fit. This is done by setting the third argument of the *polyfit*–command as one. The slope(*p(1)*) and the axis intercept(*p(2)*) are then written in the matrix *Fit*. The coefficient of determination(COD) of the linear fit function is calculated and added to the matrix in form of a single number. A coefficient of 0 means no correlation. A coefficient of 1 signifies a perfect linear correlation and a perfect fit. Additionally the values of x, y and of the linear fit are saved. This will be important for plotting the obtained values.

Listing 3.9: Finding the point of intersection

```
for k = 1:2:length(Fit)
    if Fit(c)>0 && Fit(c+1)>0 || Fit(c)<0 && Fit(c+1)<0
        c= c+1;
    else
    syms x y
    A = [-1*Fit(c,1) 1; -1*Fit((c+1),1) 1];
    B = [Fit(c,2); Fit((c+1),2)];

    X = linsolve(A,B);

    inters(b,1) = X(1);
    inters(b,2) = X(2);
```

```
        c = c+2;
        b = b+1;
        end
end
```

In a next step the correct pair of slopes and axis intercepts have to be selected for the calculation of the point of intersection (Listing 3.9).

With the *linesolve*-command a linear equation system can be solved. For this, the linear fit function has to be in the form $-kx + y = d$ and the value of x has to be specified. For this reason, A and B are defined. The resulting values, the coordinates of the point of intersection, are saved in the matrix *inters*.

3.1.5. Plotting of the Results

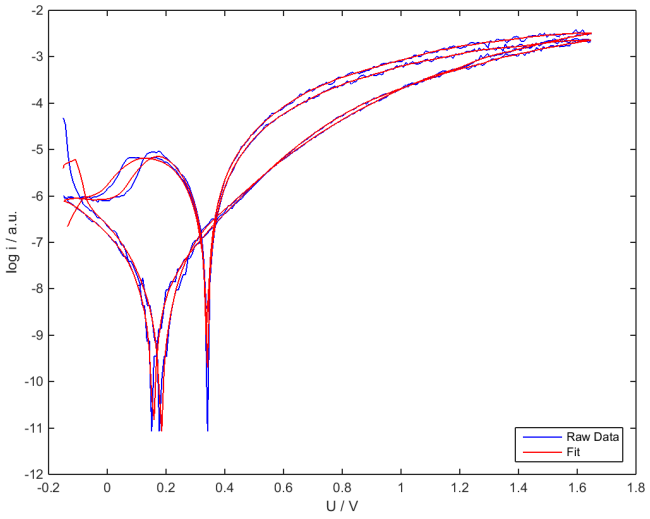

Figure 3.5.: Raw data and fitted data measured in tap water.

Here, the user should be able to choose a directory for the data storage. The code for choosing a folder is given in Listing 3.10. The plots should be generated automatically and saved to the given folder. In addition, the pictures should be named similar to the original data file without the typical ending of the data format.

Listing 3.10: Selecting the folder to save the plots to and preparation for the name of the plots.

```
directory_name = uigetdir('c:\data\', 'Save graphics to ...');
[pathstr,name,ext] = fileparts(filename);
```

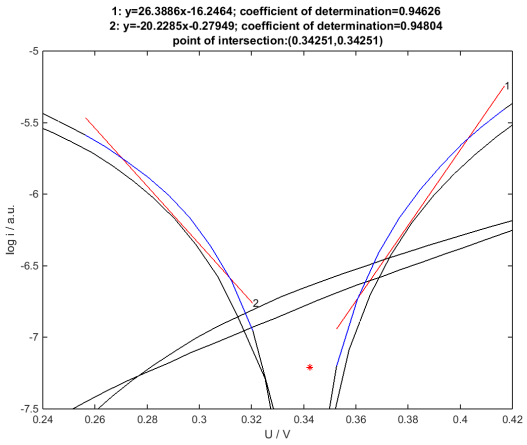

Figure 3.6.: Fitted data curve (black) with areas of regression (blue), regression lines (red) and point of intersection. Data measured in tap water.

Figure 3.5 shows a plot with the raw data curve (blue) and the smoothed curve (red). Figure 3.6 shows the fitted curve (black), the areas for regression (blue), the regression lines (red) and the point of intersection. The equations for the regression lines and the coordinates of the point of intersection are shown above Figure 3.6.

With the help of this program the time processing the data and getting the desired plots and the point of intersection of the fits is done in less than one minute. That is a great improvement for this task in time in contrast to the evaluation by hand. Furthermore, the possibility to make mistakes while doing the evaluation is also minimised.

3.2. Corrosion of Copper in Tap Water, NaCl and Ascorbic Acid Solutions

The influence of tap water, NaCl and an organic acids on the behaviour of copper corrosion was tested.

It is known, that dissolved CO_2 in the water leads to the formation of a coating on copper [4]. The NaCl–solution was used to make the effect of pitting corrosion visible. The ascorbic acid was chosen to investigate the effect of an organic, acidic chemical compound on copper.

3.2.1. Tap water

A large number of different ions are dissolved in tap water. In Vienna the water is analysed regularly and the last published analysis on *wien.at*[**?**] states that the main ions found in the tap water are calcium, magnesium and sulfate. Additionally chloride, nitrate, sodium and potassium are found. Furthermore, CO_2 is dissolved in the tap water leading to the existence of the carbonate ion in the water.

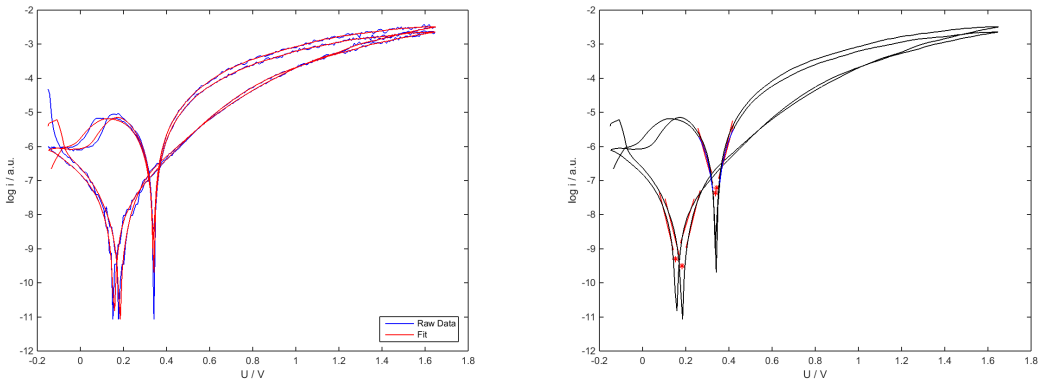

(a) Exemplary raw data curve and smoothed curve. (b) All area of regression, regression lines and points of intersections.

Figure 3.7.: Exemplary plots for tab water The plots for every single fit alone from (b) are shown in Figure 3.8.

The understanding of the chemical composition of the electrolyte is important for the interpretation of the acquired data. Sulfate as well as carbonate can react with copper ions, forming insoluble solids. The precipitate acts as protection layer on the surface of the metal. This effect is often used in water pipes and heat exchanging devices to prevent corrosion and prolong the lifetime of these devices [4]. Sulfate reacts with copper ions into a black solid ($CuSO_4$), while carbonate and copper form a green to mint coloured

solid ($CuCO_3$). A black layer can also be formed, i.e. by CuO. These corrosion products of copper are also often seen on copper statutes and on copper roofs.

The sweep rates and potential ranges were varied for the experiments. Experiment 1 in Table 3.3 was measured at with a sweep rate of 2 mV/s in the range of -0.8 to 1 V. Experiment 2 was measured with 20 mV/s in the range of -0.8 to 1.3 V. Experiment 3 was measured with the rate of 10 mV/s in the range of -0.5 to 1.3 V. Experiment 4 was measured with the rate of 10 mV/s in the range of -0.8 to 1 V. The above mentioned potentials are measured against the $Hg/HgSO_4$ reference electrode, while the results given in Table 3.3 were converted to the potential of the normal hydrogen electrode. All measured curves look quite similar. As a consequence, the existence of a sweep rate dependent reaction is excluded.

Experiment 1 was done after purging the electrolyte with nitrogen. The electrolyte was also purged with nitrogen during the experiment. After this experiment, a green coloured layer on top of the copper electrode could be obseved. It is assumed that a $CuCO_3$ layer was formed.

A black layer was observed after doing the same procedure with oxygen. It can also be seen from the achieved data in Table 3.3 that there are differences between the values for the point of intersection. The value for y_{POI} is more negative treated with oxygen. This means that the corrosion current is lower. If oxygen is present in the electrolyte, the corrosion potential(x_{POI}) is increasing. The formed carbonate layer was removed by rinsing with water. The sulfate or oxide layer was removed by the treatment with an abrasive paper. The changes in the corrosion current and the corrosion potential could be connected to the formation of the different protective layers.

After the formation of a sulfate or oxide layer the corrosion potential is shifted to a smaller, more cathodic value. This behaviour of shifting the corrosion potential towards more cathodic values is typical for protective layers which are more noble than the bulk material. In general, these layers show better corrosion resistance than the bulk material. Nevertheless, they are prone to pitting corrosion due to defect sites.

In Figure 3.7 the plots treated with oxygen are shown. The difference in the data measured with rising and falling potential, as well as the quality of the fits and the correct placement of the points of intersection can be seen easily. Towards higher potentials the curves get flat and smooth. This is typical for a process influenced by diffusion. In Figure 3.8 the areas of the fits are zoomed in and the calculated point of intersection at the time is given. Above the plots the linear equation of the fits are given together with the coordinates of the point of intersection. The coefficients of determination (COD) for this electrolyte are higher than 0.9, which means a good quality of the fits.

Table 3.1.: Mean values for x_POI and y_POI for nitrogen treated tap water.

Total mean value	
x_POI	y_POI
$0.321V \pm 0.051V$	-7.147 ± 0.770
Mean for anodic measured values	
x_POI	y_POI
$0.281V \pm 0.041$	-7.794 ± 0.459
Mean for anodic measured values	
x_POI	y_POI
$0.361V \pm 0.002$	-6.499 ± 0.236

Table 3.2.: Mean values for x_POI and y_POI for oxygen treated tap water.

Total mean value	
x_POI	y_POI
$0.263V \pm 0.085V$	-8.170 ± 1.042
Mean for anodic measured values	
x_POI	y_POI
$0.186V \pm 0.032V$	-9.116 ± 0.369
Mean for anodic measured values	
x_POI	y_POI
$0.340V \pm 0.002$	-7.224 ± 0.097

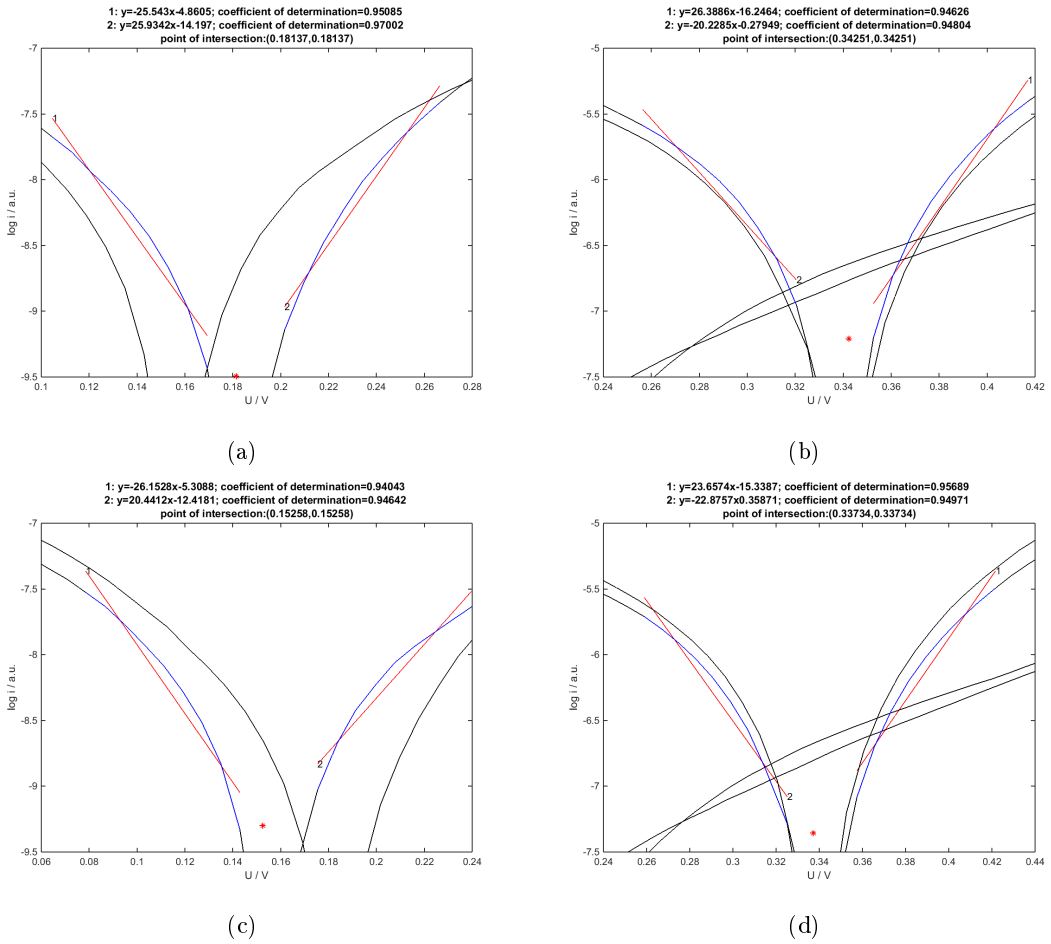

Figure 3.8.: The plots show the smoothed cure in the back(black), the areas used for the interpolation (blue) and the fits(red), that lead to the point of intersection. The corresponding numerical results are listed in Table 3.3 Experiment 4.

Table 3.3.: Results for tap water as electrolyte. k, d and COD for the fits and x and y of the POI are given.

Experiment	k_1	d_1	COD_1	k_2	d_2	COD_2	x_{POI}	y_{POI}
1	-29,5328	0,056752	0,97318	21,8675	-14,4388	0,97009	0,28201	-8,2719
	23,8519	-15,4303	0,95477	-21,7378	0,96858	0,95284	0,35971	-6,8506
	-21,2809	-0,063985	0,96522	24,8412	-15,4976	0,95226	0,33462	-7,1851
	22,924	-14,6931	0,96228	-23,0026	1,8879	0,94608	0,36103	-6,4168
2	-22,5494	-1,5815	0,95817	23,0634	-14,058	0,94816	0,27353	-7,7494
	26,1869	-15,898	0,94816	-20,6163	1,1381	0,9631	0,36399	-6,3661
	-23,9234	-2,3705	0,95029	22,3522	-13,2017	0,96293	0,23406	-7,97
	23,0227	-14,6206	0,96068	-22,8032	1,817	0,95357	0,3587	-6,3624
3	-23,5652	-3,2373	0,94734	22,5062	-13,8005	0,96739	0,22928	-8,6403
	21,5133	-14,5324	0,96791	-24,5327	1,1607	0,94258	0,34081	-7,2004
	-20,7305	-502489	0,96574	26,7592	-13,9134	0,95985	0,18245	-9,0312
	20,6932	-14,1586	0,96367	-24,5252	0,204	0,94175	0,33974	-7,1282
4	-25,543	4,8605	0,95085	25,9342	-14,194	0,97002	0,18137	-9,4932
	26,3886	-16,2464	0,94626	-20,2285	-0,27949	0,94804	0,34251	-7,208
	-26,1528	-5,3088	0,94043	20,4412	-12,4181	0,94642	0,15258	-9,2992
	23,6574	-15,3387	0,95689	-22,8757	0,35871	0,94971	0,33734	-7,3581

3.2.2. NaCl

Pitting corrosion is a common issue in industry. If chloride ions are present in the electrolyte, pitting corrosion will be formed. Chloride ions are small and penetrate easily through the noble oxide to the bulk material. Chloride can react with copper in two different ways. With copper(I) chloride forms the in water insoluble white to greyish coloured solid CuCl, whereas copper(II) and chloride form a brown to green-blueish solid which is very soluble in water. Copper(I) and copper(II) are always in equilibrium. Soluble ions are getting distributed by diffusion in the electrolyte. Therefore, there always is a lack of the soluble form directly next to the electrode. The protection layer formed by chlorides is normally quite thin [4][**?**].

For pitting corrosion to occur, most parts of the surface are passivated and act as cathodes. In small areas, the protective layer is damaged. The bulk material is exposed to the solution. Chloride ions can be starters for pitting corrosion by diffusing to local anodes. There, the area is charged positive (anodes). Chloride reacts with H^+–ions, resulting in the formation of HCl. The pH is getting more acid. This normally leads to a faster corrosion process and to the formation of holes in the metal.

In this experiment a NaCl solution (0.1 M or 1 M) was used. The sweep rate was always 20 mV/s in a range of -1 to 1.3 V. The given potentials are against $Hg/HgSO_4$, while the results are given against the normal hydrogen electrode. The experiments were performed at room temperature.

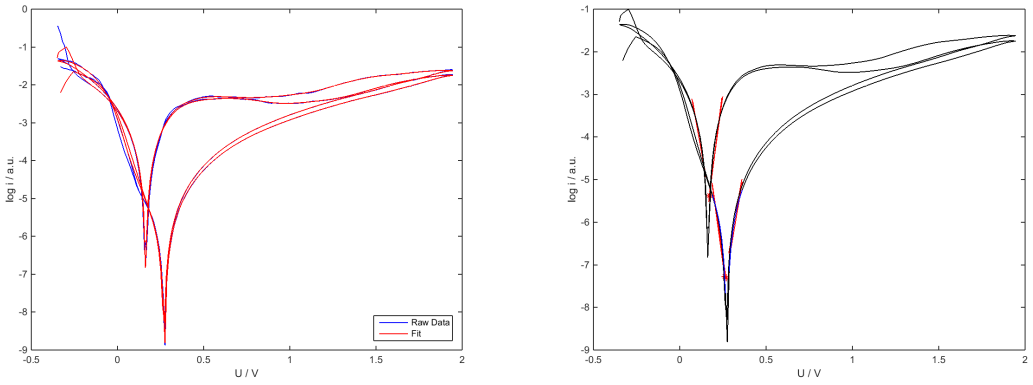

(a) Exemplary raw data curve and smoothed curve. (b) All area of regression, regression lines and points of intersections.

Figure 3.9.: Exemplary plot of 0.1 M NaCl–solution treated with oxygen. The two groups of the points of intersection are clearly visible.

Tables 3.6 and 3.7 show the results of the evaluation of the data with the NaCl–concentration of 0.1 M. The corresponding plots are shown in Figure 3.9, Figure 3.10,

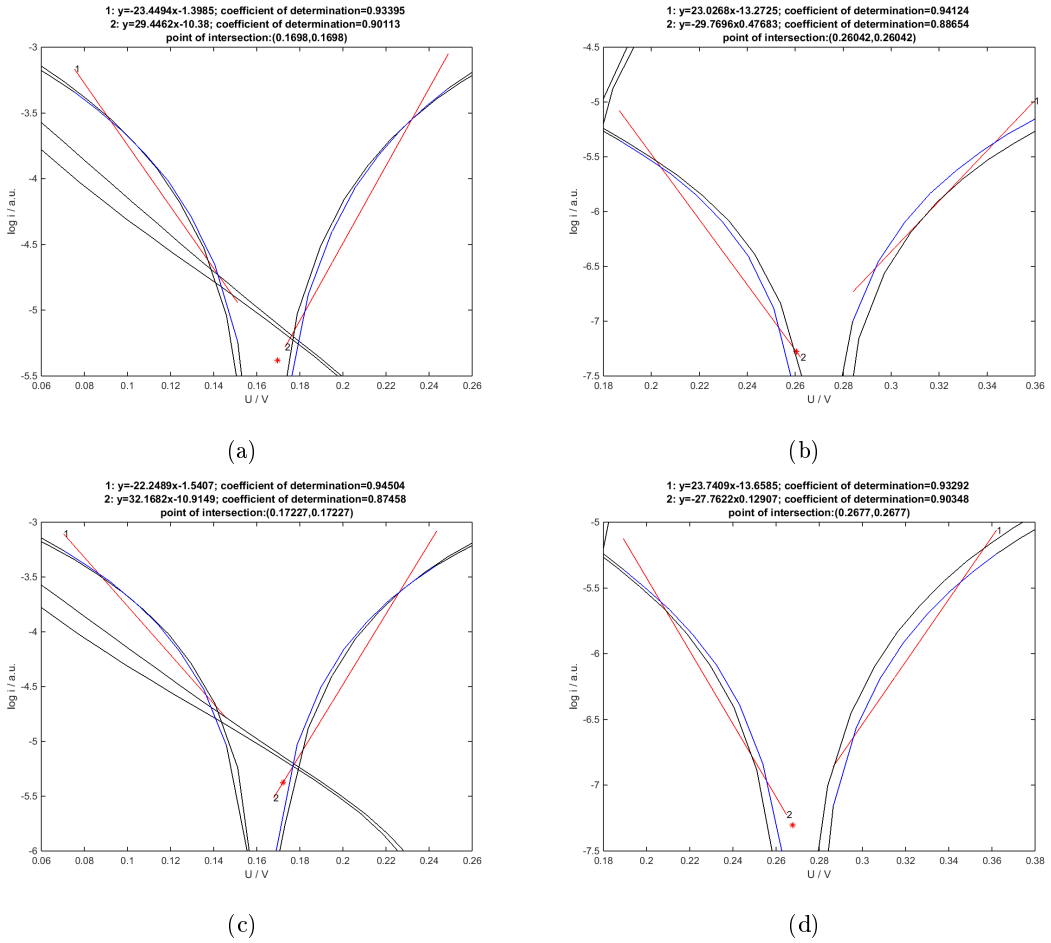

Figure 3.10.: 0.1 M NaCl solution treated with oxygen. The corresponding numerical results are listed in Table 3.6 Experiment 2.

Figure 3.11 and Figure3.12. Again the solution was also tested with oxygen as well as with nitrogen.

If the results of Table 3.6 are combined with the form of the curve in Figure 3.9 it can be assumed that chemical reactions occurred while rising the potential. The curve in the left plot in Figure 3.9 shows a curvy line between 0.1 and 1.5 V, which is expected for a diffusion controlled process. The corrosion potential is shifted to a smaller value leading to the assumption that a protective layer is formed during the experiment.

The difference between the oxygen and nitrogen treated solutions can be seen by comparing the Figures 3.9 and 3.11. In both cases, anodic and cathodic measured data forms groups. However, the difference between the two groups is bigger in case of the oxygen treated solution. The anodic measured corrosion current for the oxygen–treated solution

Table 3.4.: Mean values for x_POI and y_POI for oxygen treated 0.1 M NaCl–solution.

Total mean value	
x_POI	y_POI
$0.214V \pm 0.069V$	-5.637 ± 0.914
Mean for anodic measured values	
x_POI	y_POI
$0.152V \pm 0.017V$	-4.966 ± 0.389
Mean for anodic measured values	
x_POI	y_POI
$0.276V \pm 0.028V$	-6.308 ± 0.779

Table 3.5.: Mean values for x_POI and y_POI for nitrogen treated 0.1 M NaCl–solution.

Total mean value	
x_POI	y_POI
$0.245V \pm 0.091V$	-4.780 ± 0.271
Mean for anodic measured values	
x_POI	y_POI
$0.150V \pm 0.005V$	-4.585 ± 0.275
Mean for anodic measured values	
x_POI	y_POI
$0.324V \pm 0.009V$	-4.942 ± 0.130

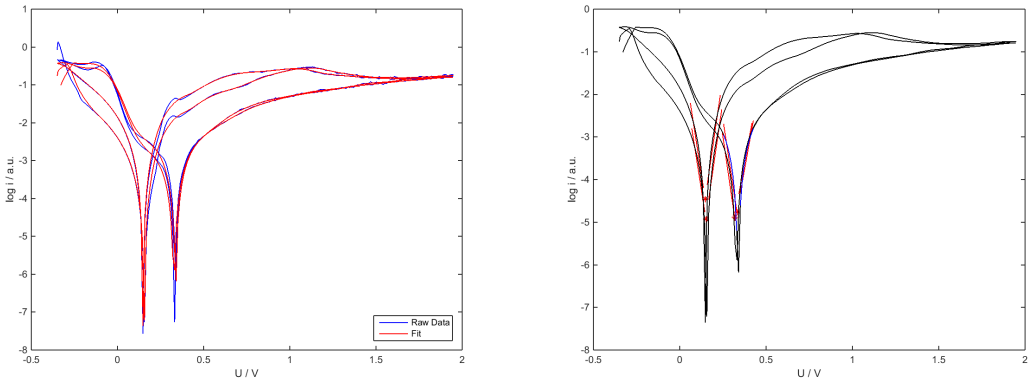

(a) Exemplary raw data curve and smoothed curve. (b) All area of regression, regression lines and points of intersections.

Figure 3.11.: Examplary plot of 0.1 M NaCl–solution treated with nitrogen. The raw data of two curves is curvy on the right (anodic) branch.

is lower than the average corrosion current. This leads to the assumption that a protective layer is built.

The quality of the fit is not as good as for the data for the tap water. Most of the fits show a coefficient of determination of around 0.90.

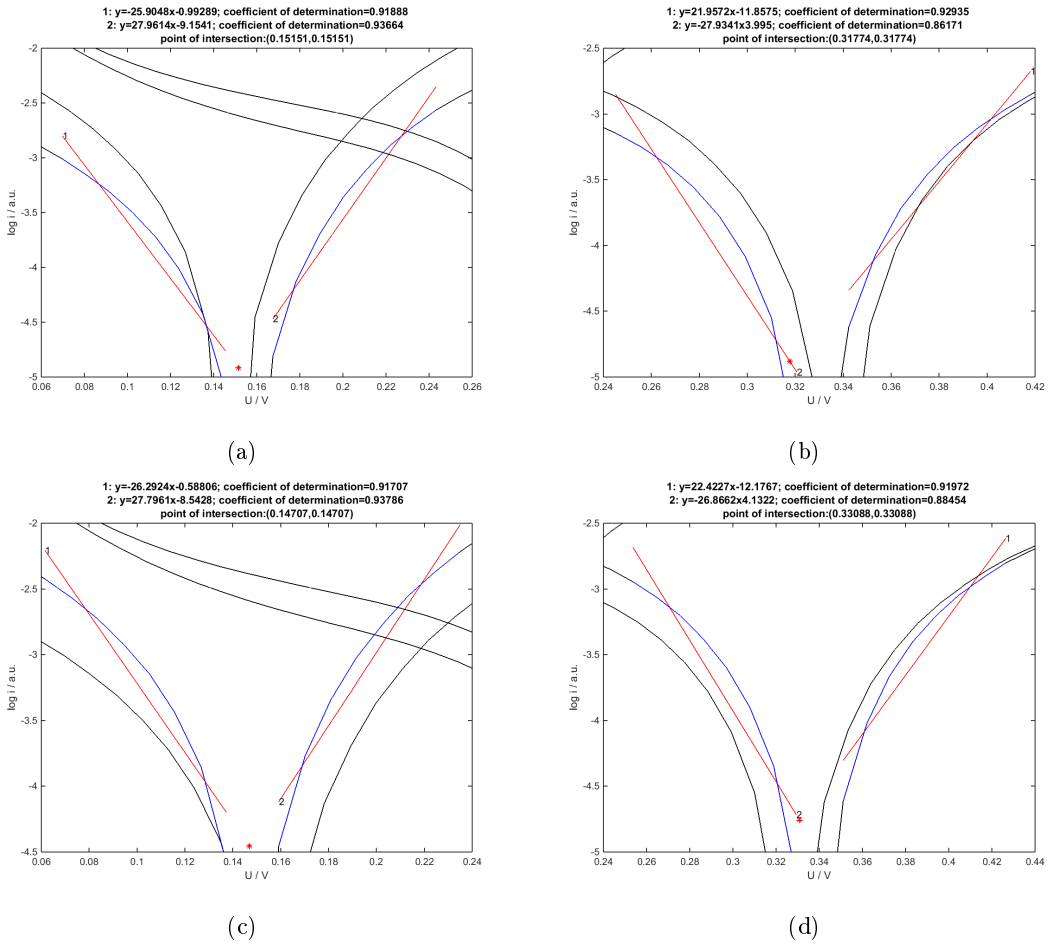

Figure 3.12.: 0.1 M NaCl solution treated with nitrogen. The corresponding numerical results are listed in Table 3.7 Experiment 3.

Table 3.6.: The results of the measurement with electrolyte being 0.1 M NaCl in water treated with oxygen. One point of intersection in the first paragraph was not found.

Experiment	k_1	d_1	COD_1	k_2	d_2	COD_2	x_{POI}	y_{POI}
1	-22,756	-2,3203	0,90631	24,0924	-8,1909	0,87532	0,12569	-5,1626
	29,0151	-12,6063	0,94045	-29,546	1,4209	0,95394	0,23953	-5,6563
	-21,7163	-1,3042	0,93603	33,4991	-9,4516	0,87694	0,14756	-4,5086
	32,5171	15,0037	0,92143	-21,9339	0,11513	0,93907	0,27343	-6,1125
2	-23,4494	-1,3985	0,93395	29,4462	-10,38	0,90113	0,1698	-5,3801
	23,0268	-13,2725	0,94124	-29,7696	0,47683	0,88654	0,26042	-7,2758
	-22,2489	-1,5407	0,4504	32,1682	-10,9149	0,87458	0,17227	-5,3734
	23,7409	-13,6585	0,93292	-27,7622	0,12907	0,90348	0,2677	-7,303
3	-28,4077	-0,61304	0,89866	24,9518	-8,4167	0,9471	0,14625	-4,7676
	32,2829	-15,9318	0,87341	-20,5964	0,5823	0,93265	0,3123	-5,8499
	-23,8425	-1,0483	0,93439	31,2667	-9,2614	0,9206	0,14903	-4,6016
	22,3682	-12,4611	0,92701	-28,1007	2,9111	0,88889	0,30459	-5,648

Table 3.7.: The results of the measurement with electrolyte being 0.1 M NaCl in water treated with nitrogen. One point of intersection in the first paragraph was not found.

Experiment	k_1	d_1	COD_1	k_2	d_2	COD_2	x_{POI}	y_{POI}
1	29,4814	-14,8506	0,87665	19,3957	1,2346	0,90535	0,3291	-5,1484
	-25,4765	-0,62578	0,92888	28,5296	-8,4028	0,92811	0,144	-4,2945
	27,7169	-14,2564	0,88307	-20,7004	1,9298	0,91019	0,3343	-4,9905
2	-22,4728	-1,3423	0,9403	3202783	-9,8591	0,9053	0,15556	-4,8381
	21,2012	-11,6324	0,92672	27,9643	3,8234	0,84432	0,31436	-4,9676
	-22,5279	0,99295	0,9435	32,8061	-9,4119	0,89494	0,15215	-4,4205
	22,5242	-12,0466	0,92612	-26,9823	3,6395	0,86819	0,31685	-4,9098
3	-25,9048	-0,99289	0,91888	17,9614	-9,1541	0,93664	0,15151	-4,9177
	21,9572	-11,8575	0,92935	-27,9341	3,995	0,86171	0,31774	-4,8808
	-26,2924	-0,58806	0,91707	27,7961	-8,5428	0,93786	0,14707	-4,4548
	22,4227	-12,1767	0,91972	-26,8662	4,1322	0,88454	0,33088	-4,7574

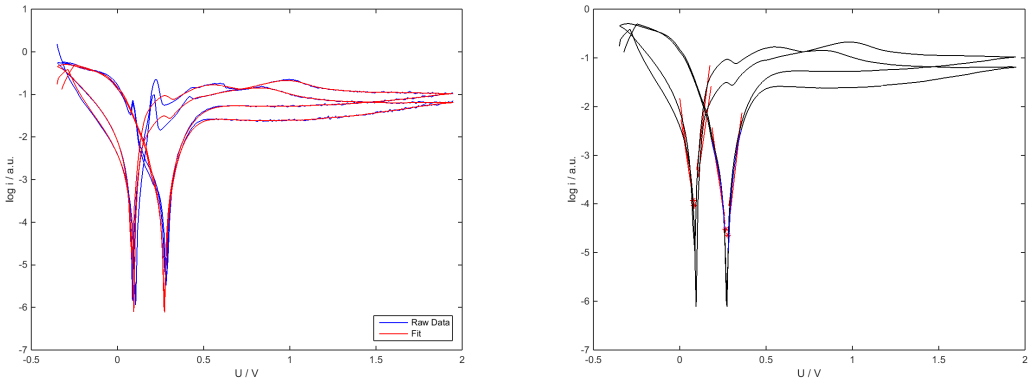

(a) Exemplary raw data curve and smoothed curve. (b) All area of regression, regression lines and points of intersections.

Figure 3.13.: Exemplary plot for 1 M NaCl solution treated with oxygen.

The same experiments were done using a 1M NaCl solution. By increasing the concentration of the NaCl solution, two trends are expected:

- The corrosion current rises.
- The corrosion potential decreases.

The noise of the raw data on the anodic side is big. Especially in Figure 3.14, the curves are noisy. In Figure 3.11 the noise exists, but is smaller . This behaviour was also observed in Figure 3.15, the 1M NaCl solution with oxygen. It can be seen, that the current per area is rising very fast when the potential is increased only a little. Therefore it is assumed, that this is a sign of pitting corrosion.

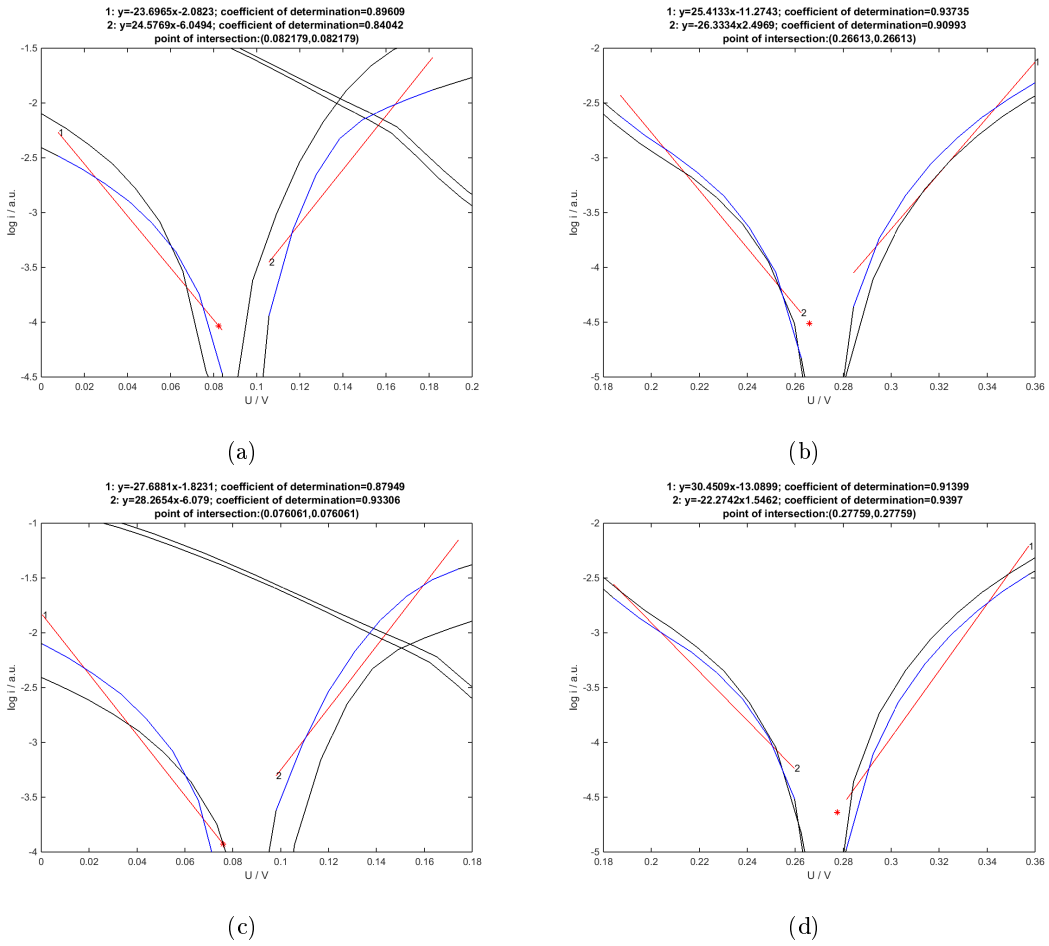

Figure 3.14.: 1 M NaCl solution treated with oxygen. The corresponding numerical results are given in Table 3.6.

Table 3.8.: Mean values for x_POI and y_POI for oxygen treated 1 M NaCl–solution.

Total mean value	
x_POI	y_POI
$0.190V \pm 0.108V$	-3.973 ± 0.442
Mean for anodic measured values	
x_POI	y_POI
$0.077V \pm 0.004V$	-3.759 ± 0.266
Mean for anodic measured values	
x_POI	y_POI
$0.284V \pm 0.016V$	-4.148 ± 0.501

Table 3.9.: Mean values for x_POI and y_POI for nitrogen treated 1 M NaCl–solution.

Total mean value	
x_POI	y_POI
$0.200V \pm 0.108V$	-4.155 ± 0.501
Mean for anodic measured values	
x_POI	y_POI
$0.090V \pm 0.019V$	-3.787 ± 0.421
Mean for anodic measured values	
x_POI	y_POI
$0.292V \pm 0.030V$	-4.461 ± 0.335

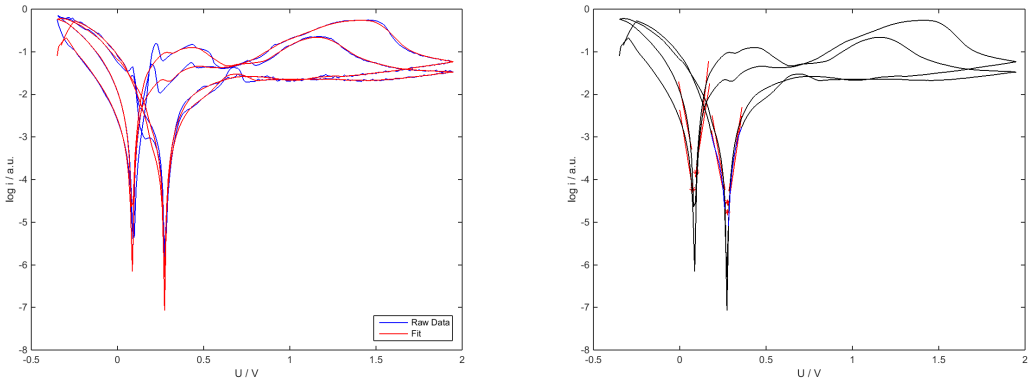

(a) Exemplary raw data curve and smoothed curve. (b) All area of regression, regression lines and points of intersections.

Figure 3.15.: Exemplary plot for 1 M NaCl solution treated with nitrogen.

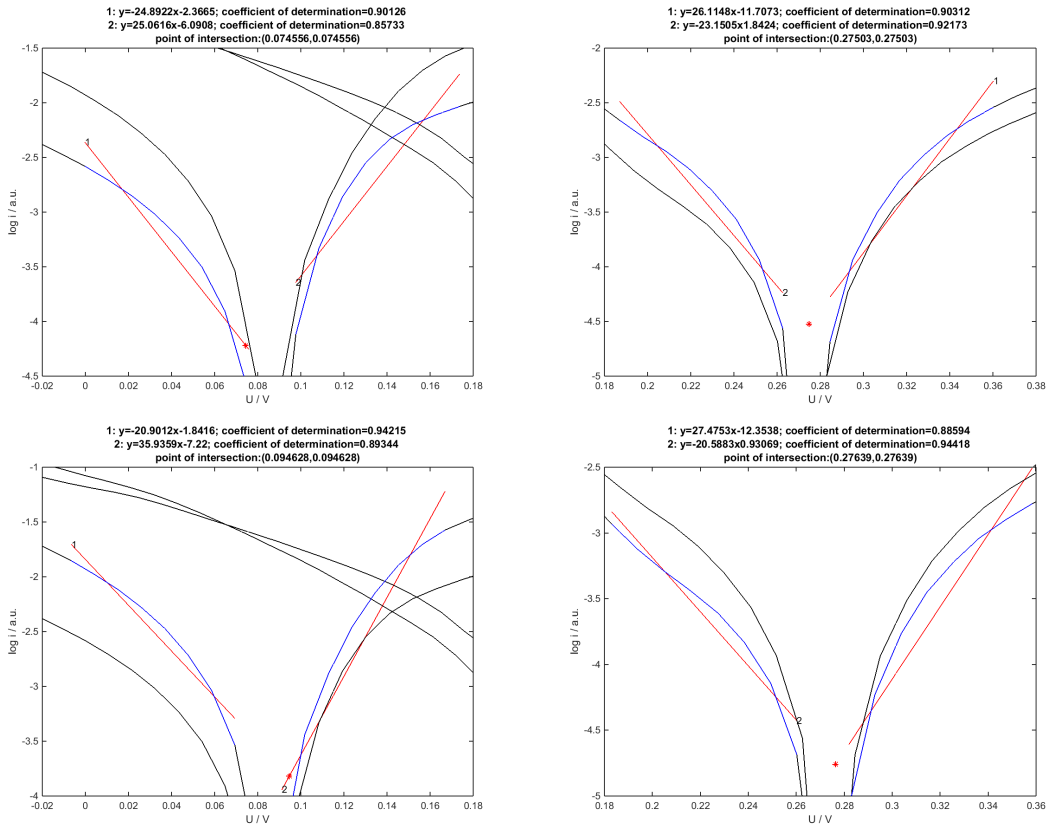

Figure 3.16.: 1 M NaCl solution treated with nitrogen. The corresponding numerical results are given in Table 3.6.

Table 3.10.: The numerical results of the data measured with an electrolyte of 1 M NaCl in water treated with oxygen. One point of intersection in the first paragraph was not found.

Experiment	k_1	d_1	COD_1	k_2	d_2	COD_2	x_{POI}	y_{POI}
1	21,074	-10,1398	0,93069	-28,9168	3,6764	0,8538	0,27693	-4,3038
	-24,8776	-1,9869	0,8996	30,4405	-6,1913	0,94952	0,076004	-3,877
	24,2903	-11,2031	0,92846	-26,3584	2,9748	0,88974	0,27993	-4,4036
2	-23,6965	-2,0823	0,89609	24,5769	-6,0494	0,84042	0,082179	-4,0297
	25,4133	-11,2743	0,93735	-26,3334	2,4969	0,90993	0,26613	-4,5111
	-27,6881	-1,9231	0,87949	28,2654	-6,079	0,93306	0,076061	-3,9291
	30,4509	-13,0899	0,91399	-22,2742	1,5462	0,9397	0,27759	-4,637
3	-19,914	-2,1488	1	12,8992	-4,4663	1	0,070626	-3,5553
	19,3029	-9,5689	1	-11,5755	0,14457	1	0,31457	-3,4967
	-13,6924	-2,3284	1	14,925	-4,5755	1	0,078523	-3,4036
	9,0411	-6,132	1	-21,6408	2,6726	1	0,28696	-3,5375

Table 3.11.: The numerical results of the data measured with an electrolyte of 1 M NaCl in water treated with oxygen. One point of intersection in the first paragraph was not found.

Experiment	k_1	d_1	COD_1	k_2	d_2	COD_2	x_{POI}	y_{POI}
1	24,0553	-10,8413	0,93688	-27,6056	2,6634	0,88317	0,26141	-4,553
	-24,5489	-1,5839	0,90829	29,3082	-5,4803	0,94388	0,072347	-3,3599
	24,8263	11,8253	0,91589	-22,884	1,6382	0,89914	0,28219	-4,8195
2	-24,8922	-2,3665	0,90126	25,0616	-6,098	0,85733	0,074556	-4,2223
	26,1148	-11,7073	0,90312	-23,1505	1,8424	0,92173	0,27503	-4,5248
	-20,9012	-1,8416	0,94215	35,9359	-7,22	0,89344	0,094628	-3,8194
	27,4753	-12,3538	0,88594	-20,5883	9,3069	0,94418	0,27639	-4,7598
3	-12,2579	-2,718	1	21,3458	-6,7162	1	0,11898	-4,1764
	13,1809	-8,2649	1	-15,5962	0,954	1	0,32036	-4,0423
	-18,3588	-1,7333	1	11,3445	-4,3628	1	0,088526	-3,3585
	13,7675	-8,701	1	-15,1911	1,0475	1	0,33664	-4,0664

3.2.3. Ascorbic Acid

Ascorbic acid, i.e. vitamin C, is an organic acid with a pK_s–value of 4.25. This acid is easily oxidised and often used as antioxidant. Furthermore, ascorbic acid has a good solubility in water.

All measurements were done with a sweep rate of 20 mV/s in the range from -1 to 1.3 V against the $Hg/HgSO_4$ reference electrode at room temperature.

The difference in the measured average potential is not as big as observed with the NaCl–solutions. The form of the curve is smooth and has a logarithmic form. Therefore, a diffusion controlled process is expected (see Figure 3.17).

When comparing the results of the two measurement series with oxygen and with nitrogen, no significant difference can be observed. The average corrosion current is also small compared comparable to the corrosion current measured in tap water. Here, an influence of oxygen or nitrogen on the corrosion process of copper is negligible.

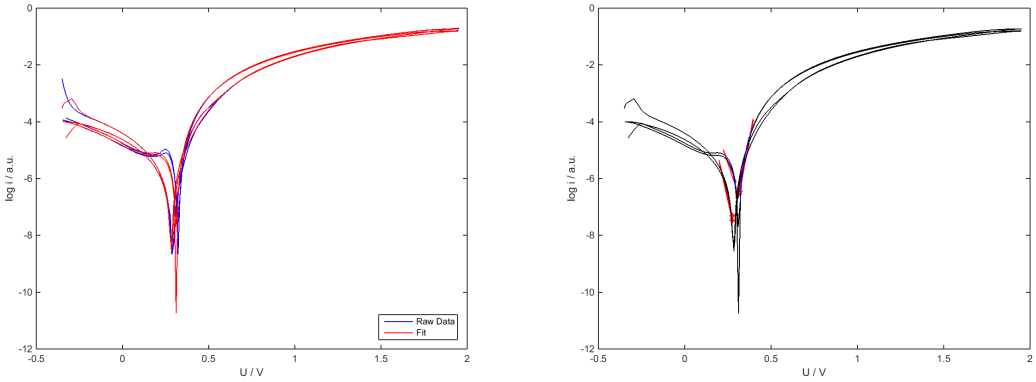

(a) Exemplary raw data curve and smoothed curve. (b) All area of regression, regression lines and points of intersections.

Figure 3.17.: Exemplary plot for 0.1 M ascorbic acid treated with oxygen.

Table 3.12.: Mean values for x_POI and y_POI for oxygen treated 0.1 M ascorbic acid solution.

Total mean value	
x_POI	y_POI
$0.298V \pm 0.020V$	-6.986 ± 0.476
Mean for anodic measured values	
x_POI	y_POI
$0.280V \pm 0.008V$	-7.429 ± 0.139
Mean for anodic measured values	
x_POI	y_POI
$0.316V \pm 0.005V$	-6.543 ± 0.098

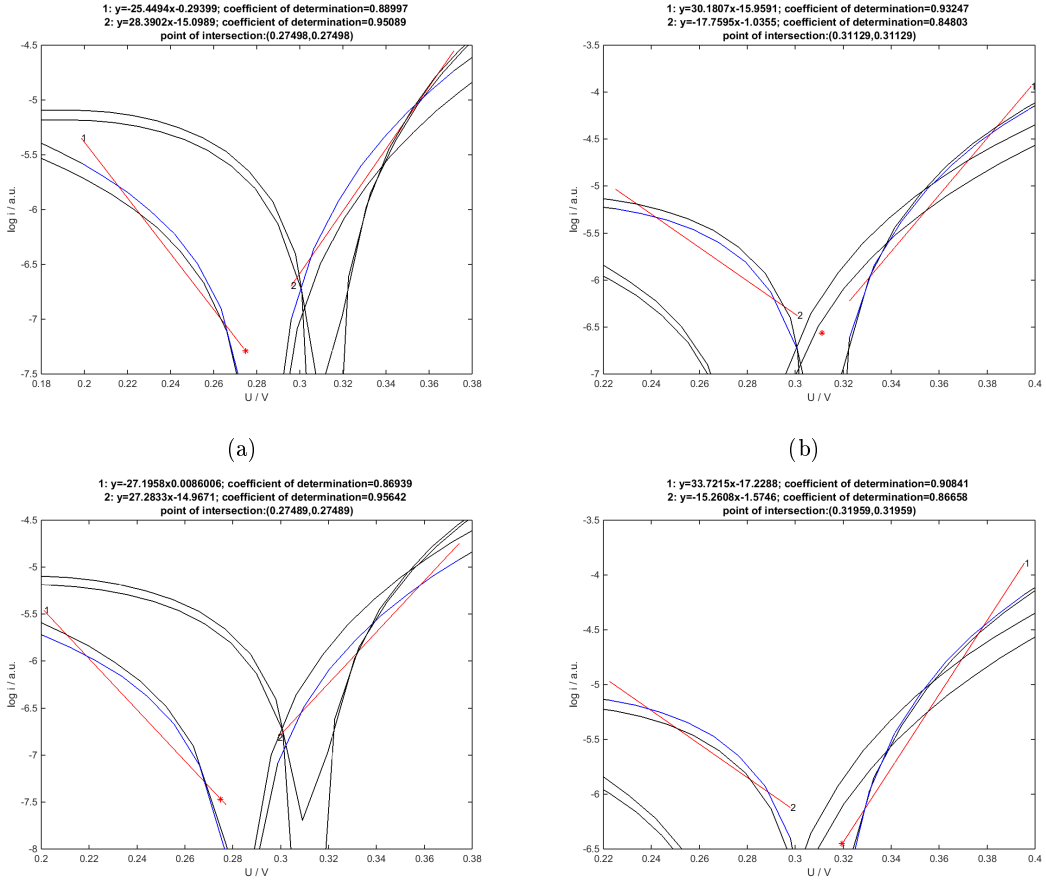

Figure 3.18.: 0.1 M ascorbic acid treated with oxygen. The corresponding numerical results are given in Table 3.14.

Table 3.13.: Mean values for x_POI and y_POI for nitrogen treated 0.1 M ascorbic acid solution.

Total mean value	
x_POI	y_POI
$0.293V \pm 0.150V$	-7.005 ± 0.540
Mean for anodic measured values	
x_POI	y_POI
$0.286V \pm 0.009V$	-7.312 ± 0.517
Mean for anodic measured values	
x_POI	y_POI
$0.303V \pm 0.016V$	-6.596 ± 0.181

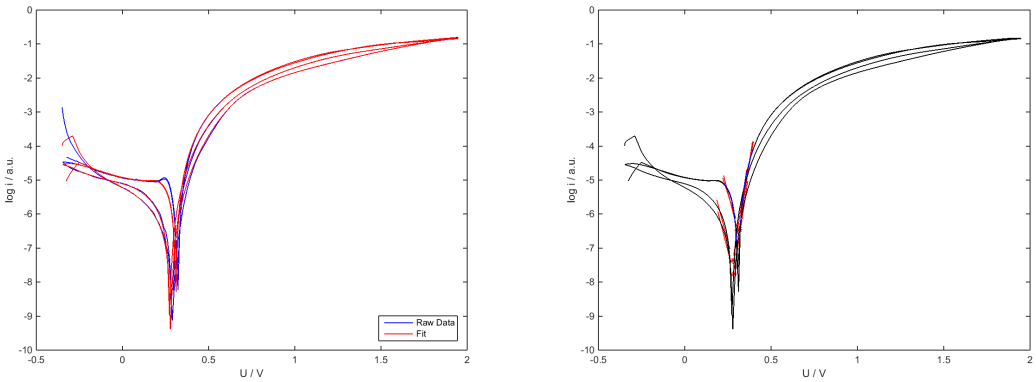

(a) Exemplary raw data curve and smoothed curve. (b) All area of regression, regression lines and points of intersections.

Figure 3.19.: Exemplary plot for 0.1 M ascorbic acid treated with nitrogen.

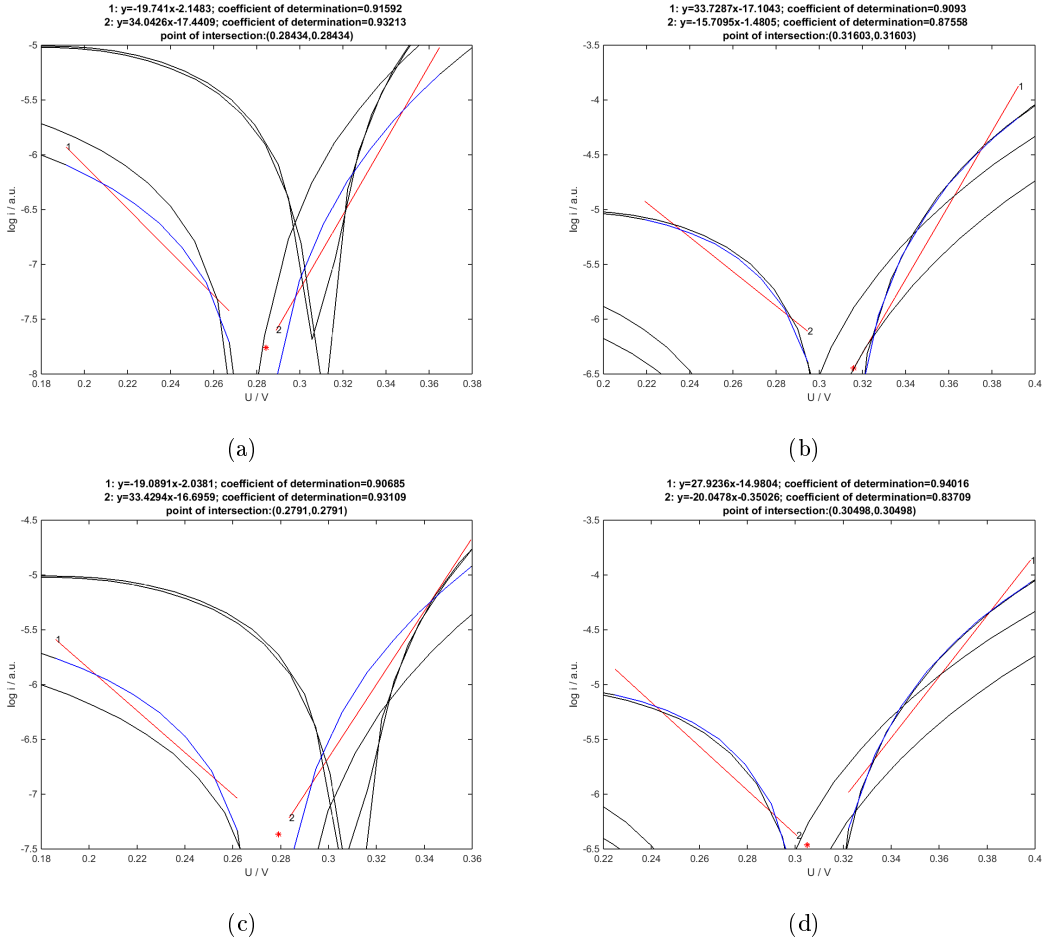

Figure 3.20.: 0.1 M ascorbic acid treated with nitrogen. The corresponding numerical results are given in Table 3.15.

Table 3.14.: Numerical results of the 0.1 M ascorbic acid solution treated with oxygen.

Experiment	k_1	d_1	COD_1	k_2	d_2	COD_2	x_{POI}	y_{POI}
1	-20,8283	-1,542	0,92636	32,8746	-16,6416	0,92881	0,28117	-7,3983
	34,4114	-17,6532	0,90681	-15,5352	-1,7015	0,87696	0,31937	-6,6631
	-21,0989	-1,6155	0,92688	32,6986	-16,985	0,92929	0,28569	-7,6433
	27,787	-15,2281	0,93918	-20,3215	-0,33746	0,84401	0,30952	-6,6274
2	-25,4494	-0,29399	0,88997	28,3902	15,0989	0,95089	0,27498	-7,2921
	30,1807	-15,9591	0,93247	-17,7595	-1,0355	0,84803	0,31129	-6,564
	-27,1958	0,0086006	0,86939	27,28336	-14,9671	0,95642	0,27489	-7,4672
	33,7215	-17,228	0,90841	-15,2608	-1,5746	0,86658	0,31959	-6,4518
3	-26,3483	-0,16287	0,88367	28,0756	-14,8502	0,94982	0,26987	-7,2735
	30,1658	-16,0276	0,92961	-17,8648	-0,92852	0,85616	0,31436	-6,5446
	-21,2625	-1,2729	0,93053	33,0885	-17,1865	0,92206	0,29279	-7,4984
	33,391	-17,1611	0,90554	-15,3788	-1,459	0,87025	0,32196	-6,4105

Table 3.15.: Numerical results of the 0.1 M ascorbic acid solution treated with nitrogen.

Experiment	k_1	d_1	COD_1	k_2	d_2	COD_2	x_{POI}	y_{POI}
1	-17,9664	-1,4024	0,92201	35,7439	-17,7064	0,89205	0,30355	-6,8562
	27,098	-14,5037	0,94873	-22,9472	-0,29762	0,84341	0,28387	-6,8115
	-26,8963	0,9003	0,85107	25,1782	-13,7406	0,95094	0,28115	-6,6617
	25,7839	-14,0799	0,95039	-25,8825	0,54464	0,82587	0,28306	-6,7816
2	-19,741	-2,1483	0,91592	34,0426	-17,4409	0,93213	0,29434	-7,7614
	33,7287	-17,1043	0,9093	15,7095	-1,4805	0,87558	0,31603	-6,4452
	-19,0891	-2,0381	0,90685	33,4294	-16,6959	0,93109	0,2791	-7,3659
	27,9236	-14,9804	0,94016	-20,0478	-0,35026	0,83709	0,30498	-6,4644
3	-18,8611	-1,7502	0,91285	33,5394	-16,6056	0,91786	0,2835	-7,0973
	30,8643	-16,0861	0,91979	-17,1145	-1,0339	0,86509	0,31373	-6,4031
	-20,8899	-1,0938	0,90075	30,6601	-15,6297	0,93454	0,28198	-6,9843
4	-27,8963	-0,46	0,87148	29,3653	-16,3954	0,96226	0,27829	-8,2233
	-27,5173	0,23921	0,87938	26,6002	-15,0734	0,95663	0,28295	-7,5469
	27,4806	-15,4333	0,9344	-20,7807	-0,045424	0,86415	0,31885	-6,6713

3.3. ZnO and 4–Methylimidazole as Corrosion Inhibitors for Copper

As inhibitors two substances, namely ZnO and 4–Methylimidazole, were used. ZnO is an inorganic inhibitor found in protective coatings. ZnO is well–known for forming bulky layers and therefore hindering the diffusion of aggressive ions [4].

The group of imidazoles is used as corrosion inhibitors for cooling or heating water circulation systems [19][20].

3.3.1. ZnO

Like mentioned above ZnO forms a protective, bulky white layer on top of the metal [1][21][4][22]. In contrast to the metal Zn, the ZnO layer is quite noble and used in a wide range of fields, e.ag. as a pigment for white colour or for drying wounds in form of salves or plasters in medicine. ZnO also prevents bacterial attacks [1].

Concerning acidic environment ZnO dissolves into the ions O^{2-} and Zn^{2+}. The Zn–ions are able to react with chloride, carbonate or sulfate to form a protective layer on top of the metal which should be protected. The formed protective layer is often a mixture of different chemical compounds. Strong bases can also dissolve ZnO by forming zincate [1].

For the experiments a suspension of 0.1 M ZnO in deionized water was used. The measurement were made with a sweep rate of 20 mV/s in an area from -1 to 1.3 V $vs. Hg/HgSO_4$ reference electrode at room temperature.

Note that a noisy curves were recorded. Nevertheless, the point of intersection could be determined.

The results of the data obtained from suspension treated with oxygen and nitrogen are quite similar. This leads to the assumption, that oxygen is not essential in the reaction for the formation of the protective layer. The strong noise in the raw data can be an indication for the formation of a bulky layer on top of the electrode. After the experiment was finished and the electrode was taken out of the electrolyte a white film was observed on top of the electrode. This film was easily rinsed with water.

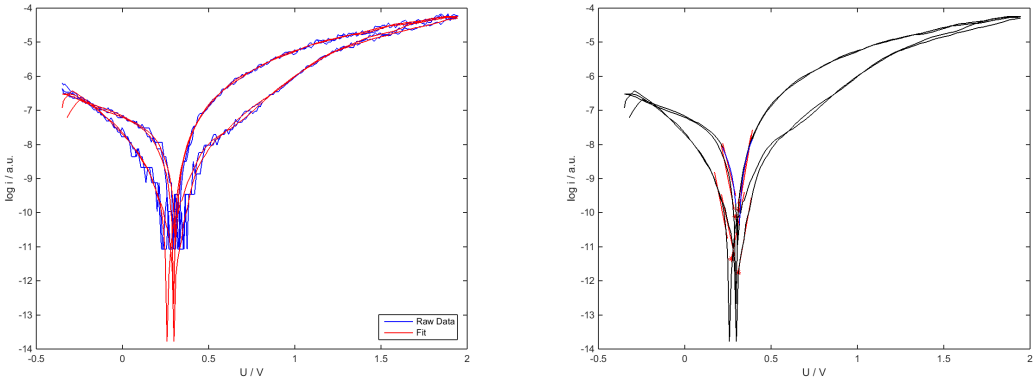

(a) Exemplary raw data curve and smoothed curve. (b) All area of regression, regression lines and points of intersections.

Figure 3.21.: Exemplary plot for 0.1 M ZnO suspension treated with oxygen.

Table 3.16.: Mean values for x_POI and y_POI for oxygen treated ZnO suspension.

Total mean value	
x_POI	y_POI
$0.300V \pm 0.021V$	-10.166 ± 0.945
Mean for anodic measured values	
x_POI	y_POI
$0.286V \pm 0.017V$	-10.894 ± 0.513
Mean for anodic measured values	
x_POI	y_POI
$0.314V \pm 0.014V$	-9.437 ± 0.661

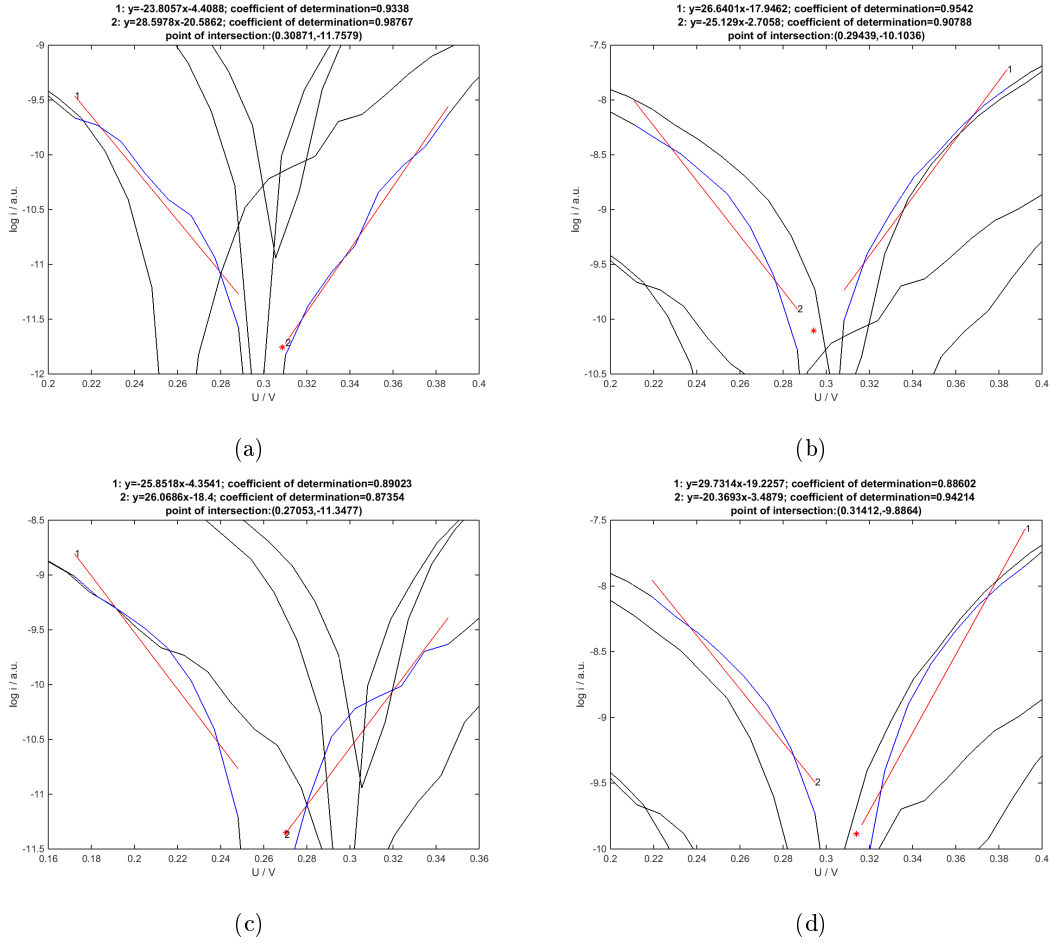

Figure 3.22.: 0.1 M ZnO suspension treated with oxygen. The corresponding numerical results are given in Table 3.18.

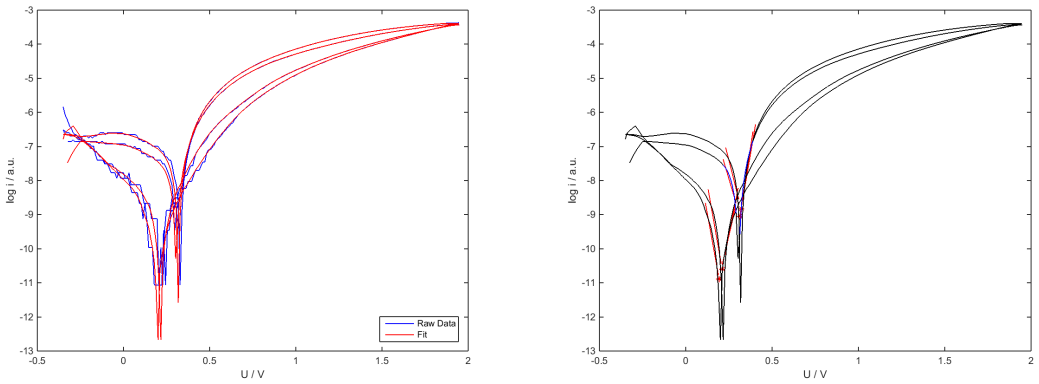

(a) Exemplary raw data curve and smoothed curve. (b) All area of regression, regression lines and points of intersections.

Figure 3.23.: Exemplary plot for 0.1 M ZnO suspension treated with nitrogen.

Table 3.17.: Mean values for x_POI and y_POI for nitrogen treated ZnO suspension.

Total mean value	
x_POI	y_POI
$0.273V \pm 0.071V$	-9.517 ± 0.794
Mean for anodic measured values	
x_POI	y_POI
$0.208V \pm 0.029V$	-10.228 ± 0.380
Mean for anodic measured values	
x_POI	y_POI
$0.338V \pm 0.017V$	-8.806 ± 0.226

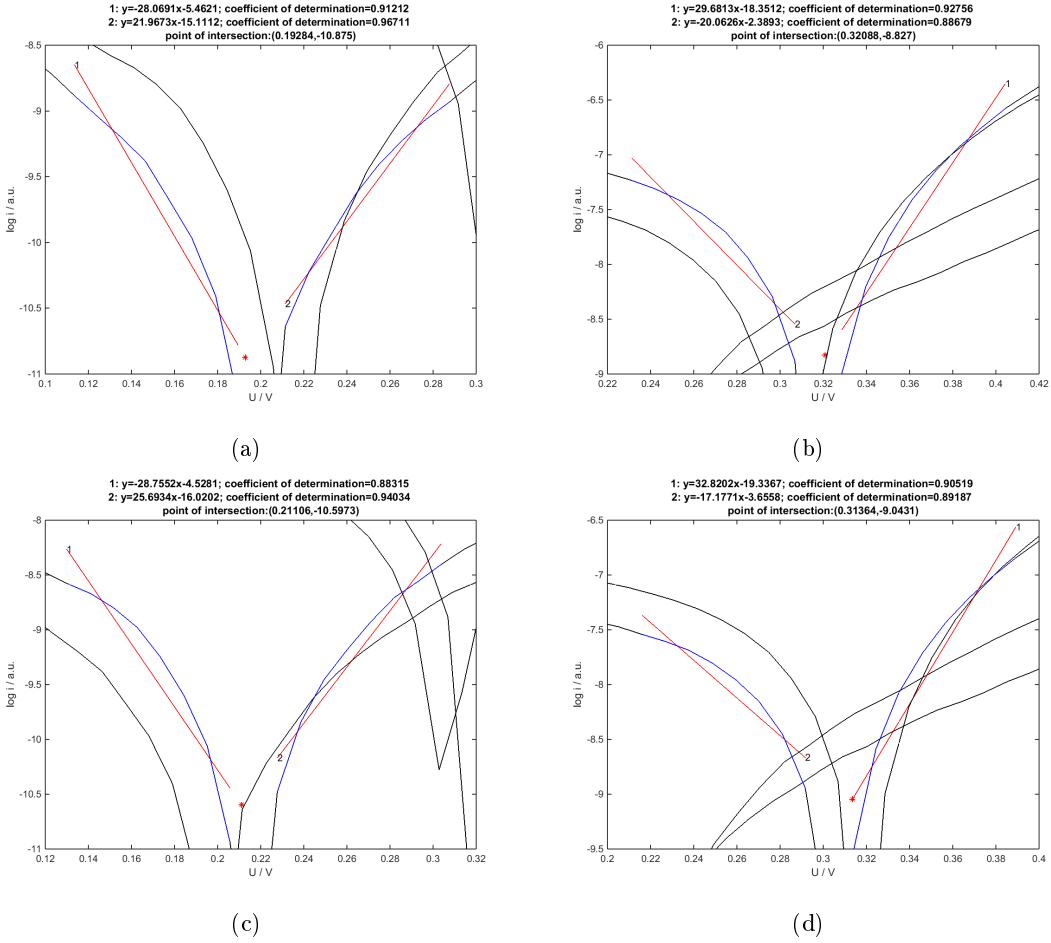

Figure 3.24.: 0.1 M ZnO suspension treated with nitrogen. The corresponding numerical results are given in Table 3.19.

Table 3.18.: Numerical results of the 0.1 M ZnO suspension treated with oxygen.

Experiment	k_1	d_1	COD_1	k_2	d_2	COD_2	x_{POI}	y_{POI}
1	-23,8057	-4,4088	0,9338	28,59780	-20,58620	0,98767	0,30871	-11,7579
	26,6401	-17,9462	0,9542	-25,129	-2,7058	0,90788	0,29439	-10,1036
	-25,8518	-4,3541	0,89023	26,0686	-18,4	0,87354	0,27053	-11,3477
	29,7314	-19,2257	0,88602	-20,3693	-3,4879	0,94214	0,31412	-9,8864
2	-31,8579	-1,6453	0,90335	22,5457	-17,6199	0,88643	0,29363	-10,9998
	24,6191	-17,3548	0,95289	-28,0976	-1,7498	0,86172	0,29602	-10,0671
	-23,1313	-4,7488	0,92822	29,6212	-18,9708	0,94034	0,2696	-10,985
	33,1511	-20,3233	0,9069	-20,3639	-3,7776	0,95076	0,30918	-10,0736
3	-26,7727	-3,4984	0,91918	25,2671	-17,8976	0,88773	0,2767	-10,9063
	24,6577	-16,4224	0,95327	-27,5134	-0,070731	0,83847	0,31342	-8,6941
	-29,6056	-1,5805	0,88425	21,7523	-16,4306	0,95489	0,28915	-10,1409
	27,3355	-17,6527	0,9425	-23,9094	-0,63557	0,87761	0,33208	-8,5753
4	-23,2054	-3,2346	0,92306	28,8334	-19,4119	0,9284	0,31087	-10,4484
	33,3431	-20,1865	0,88962	18,7433	-2,8967	0,92714	0,33194	-9,1185
	-30,5679	-2,361	0,88016	24,8526	-17,2368	0,94887	0,26842	-10,5659
	26,7143	-17,5339	0,94104	-24,0277	-1,2818	0,88963	0,32029	-8,9776

Table 3.19.: Numerical results of the 0.1 M ZnO suspension treated with nitrogen.

Experiment	k_1	d_1	COD_1	k_2	d_2	COD_2	x_{POI}	y_{POI}
1	-28,0691	-5,4621	0,91212	21,9673	-15,1112	0,96711	0,19284	-10,875
	29,6813	-18,3512	0,92756	-20,0626	-2,3893	0,88679	0,32088	-8,827
	28,7552	-4,5281	0,88315	25,6934	-16,0202	0,94034	0,21106	-10,5973
	32,8202	-19,3367	0,90519	-17,1771	-3,6558	0,89187	0,31364	-9,0431
2	-25,8635	-6,1644	0,90422	23,4643	-14,0963	0,89864	0,1608	-10,3232
	27,2489	-17,6355	0,93611	-22,1546	-1,0636	0,88753	0,33544	-8,4951
	-28,6296	-3,5734	0,86089	25,8112	-16,0185	0,95825	0,2286	-10,1181
	30,8612	-19,6048	0,91162	-19,4624	-1,3596	0,9019	0,36256	-8,4159
3	-20,3272	-5,4423	0,92538	32,7782	-18,2179	0,89101	0,24057	-10,3324
	27,818	-18,197	0,91414	-23,01446	-1,3092	0,91151	0,33224	-8,9556
	-26,4846	-5,2871	0,91757	24,022	-14,1869	0,94252	0,17621	-9,954
	24,6825	-17,3034	0,93756	-26,8528	0,28266	0,90192	0,34124	-8,8807
4	-22,7803	-4,8144	0,93379	27,119	-15,7235	0,91838	0,21862	-9,7947
	24,4424	-17,2775	0,9403	-26,516	0,21317	0,90673	0,34323	-8,888
	-25,8344	-3,6548	0,90607	26,4398	-16,1429	0,90911	0,2389	-9,8265
	31,5424	-20,2589	0,88887	-20,6692	-1,5279	0,92782	0,35875	-8,943

3.3.2. 4–Methylimidazole

4–Methylimodazole is a heterocyclic substance and precursor for many chemically synthesized drugs. It is a yellow and soluble in water. Because of the heterocycle of the 4–Methylimidazole an acid–base–interaction with metals and is observed. Therefore a protection layers on top of the metals can be formed.

The experiments were carried out with a 10 mM 4–Methylimidazole–solution at a sweep rate of 20 mV/s in the range from -1 to 1.3 V $vs. Hg/HgSO_4$ reference electrode at room temperature.

From the data above it can be concluded, that this inhibitor needs no oxygen to fully activate its inhibition effect. In the Figures **??** and 3.23 the corrosion current is nearly constant for a large voltage range. This is typical for inhibitors which only have an inhibition effect in a certain potential window and are destroyed by exceeding this window. When the electrode was taken out of the electrolyte, no visible change to the copper electrode could be noticed. A thin monoayer of azole on top of the metal must be formed. This observations are in accordance with the literature.

It should be noticed that this inhibitor is only used in a concentration of 10 mM and the experiment still shows changes to better corrosion resistance. Therefore 4–Methylimidazole is a promising substance for corrosion inhibition.

Table 3.20.: Mean values for x_POI and y_POI for oxygen treated 4–Methylimidazole solution.

Total mean value	
x_POI	y_POI
$0.265V \pm 0.052V$	-9.594 ± 0.602
Mean for anodic measured values	
x_POI	y_POI
$0.270V \pm 0.038V$	-9.791 ± 0.196
Mean for anodic measured values	
x_POI	y_POI
$0.259V \pm 0.067V$	-9.396 ± 0.815

Table 3.21.: Mean values for x_POI and y_POI for nitrogen treated 4–Methylimidazole solution.

Total mean value	
x_POI	y_POI
$0.235V \pm 0.053V$	-9.054 ± 0.712
Mean for anodic measured values	
x_POI	y_POI
$0.240V \pm 0.044V$	-9.435 ± 0.730
Mean for anodic measured values	
x_POI	y_POI
$0.230V \pm 0.065V$	-8.672 ± 0.492

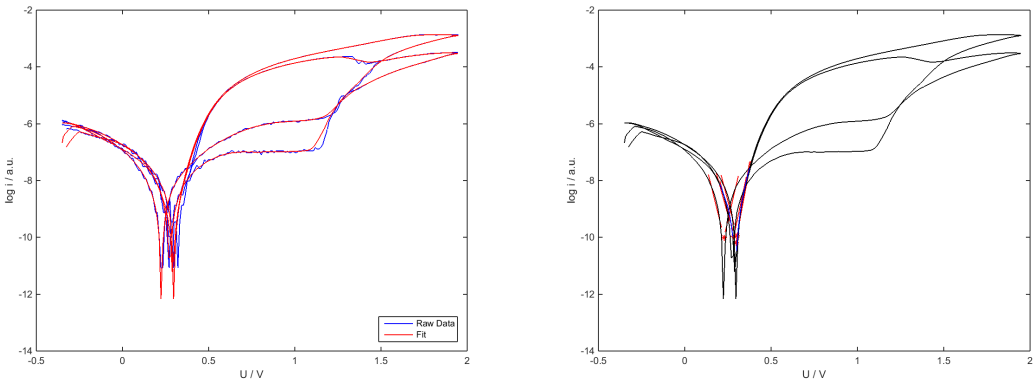

(a) Exemplary raw data curve and smoothed curve. (b) All area of regression, regression lines and points of intersections.

Figure 3.25.: Exemplary plot for 10 mM 4–Methylimidazole–solution treated with oxygen.

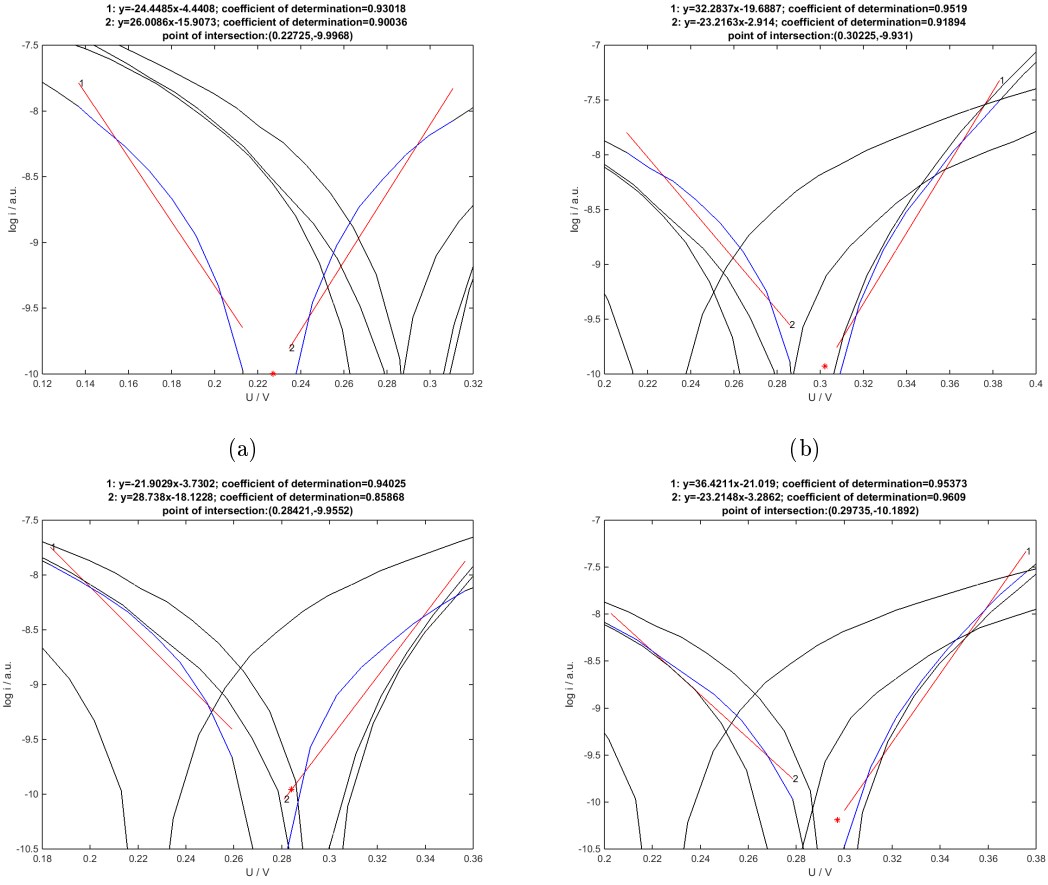

Figure 3.26.: 10 mM 4–Methylimidazole–solution treated with oxygen. The corresponding numerical results are given in Table 3.23 Experiment 1.

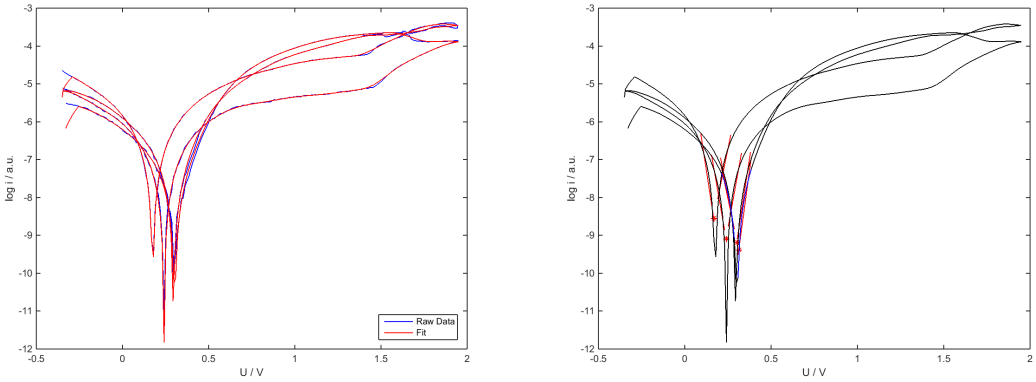

(a) Exemplary raw data curve and smoothed curve. (b) All area of regression, regression lines and points of intersections.

Figure 3.27.: Exemplary plot for 10 mM 4–Methylimidazole–solution treated with oxygen.

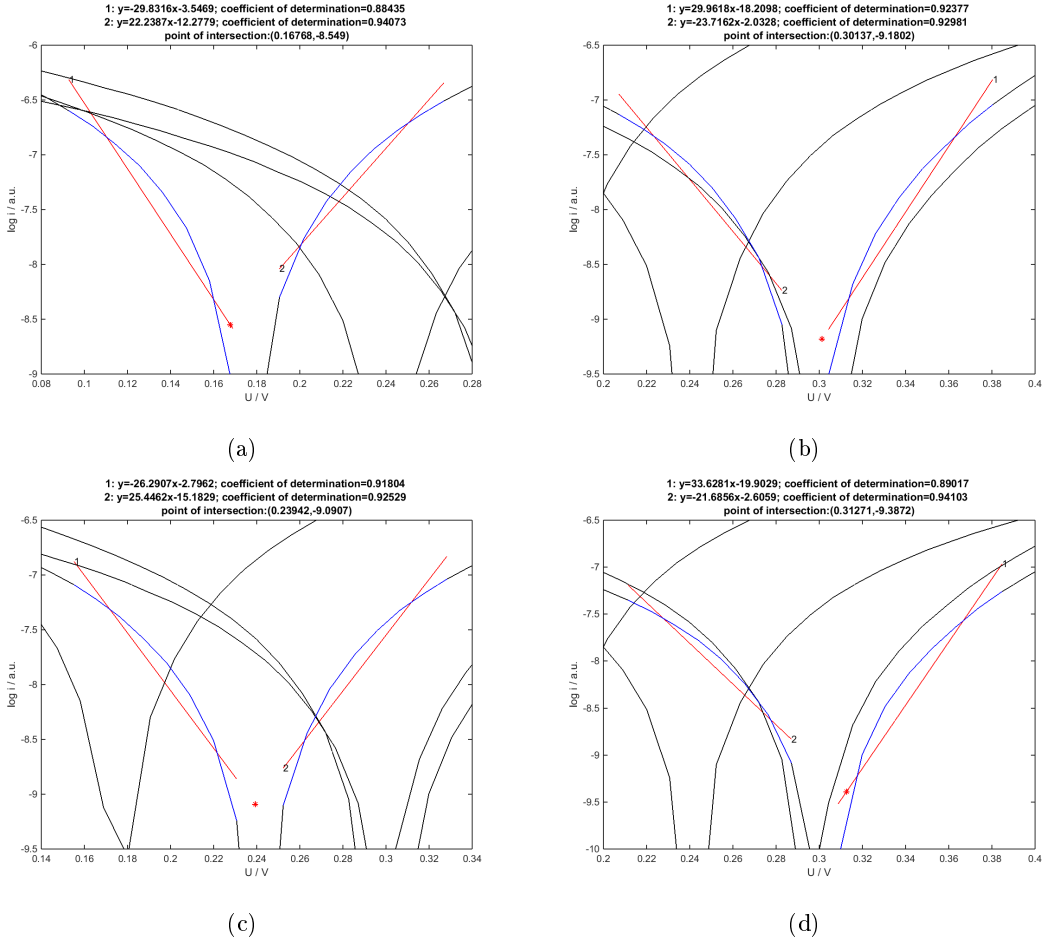

Figure 3.28.: 10 mM 4–Methylimidazole–solution treated with nitrogen. The corresponding numerical results are listed in Table 3.23 Experiment 1.

Table 3.22.: Numerical results of the 10 mM 4–Methylimidazole–solution treated with oxygen.

Experiment	k_1	d_1	COD_1	k_2	d_2	COD_2	x_{POI}	y_{POI}
1	-24,4485	-4,4408	0,93018	26,0086	-15,9073	0,90036	0,22725	-9,9968
	32,2837	-19,6887	0,9519	-23,2163	-2,914	0,91894	0,30225	-9,931
	-21,9029	-3,7302	0,94025	28,738	-18,1228	0,85868	0,2841	-9,99552
	36,4211	-21,019	0,95373	-23,2148	-3,2862	0,9609	0,29735	-10,1892
2	-31,8663	-2,4471	0,87022	21,115	-14,7736	0,92489	0,23266	-9,8611
	28,9353	-18,1696	0,97108	-29,216	-1,3965	0,91362	0,28844	-9,8235
	-26,4092	-2,6638	0,92554	23,2516	15,9846	0,92306	0,26824	-9,7477
	33,0468	-19,9527	0,95885	-25,1328	-1,8802	0,91726	0,31063	-9,6873
3	-13,4798	-5,7939	1	15,4351	-13,7802	1	0,2762	-9,517
	21,0264	-12,7184	1	-9,0663	-6,288	1	0,21369	-8,2254
	-12,5014	-5,5018	1	16,6231	-15,1186	1	0,3302	-9,6297
	13,4289	-10,4455	1	-18,4973	-5,8684	1	0,14337	-8,5203

Table 3.23.: Numerical results of the 10 mM 4–Methylimidazole–solution treated with nitrogen.

Experiment	k_1	d_1	COD_1	k_2	d_2	COD_2	x_{POI}	y_{POI}
1	-29,8316	-3,5469	0,88435	22,2387	-12,2779	0,94073	0,16768	-8,549
	29,9618	18,2098	0,92377	-23,7162	-2,0328	0,92981	0,30137	-9,1802
	-26,2907	-2,7962	0,91804	25,4462	-15,1829	0,92529	0,23942	-9,09097
	33,6281	-19,9029	0,89017	-21,6856	-2,6059	0,94103	0,31271	-9,3872
2	-18,1812	-4,7885	1	12,598	-12,0462	1	0,2358	-9,0756
	13,4887	-10,8914	1	-17,1124	-4,975	1	0,19334	-8,2835
	-11,4519	-5,8512	1	20,2252	-15,269	1	0,29731	-9,256
	13,6981	-11,0979	1	-16,4353	-4,993	1	0,2026	-8,3227
3	-12,403	-7,5975	1	16,5526	-14,2532	1	0,22986	-10,4484
	14,1908	-10,5097	1	-16,0566	-6,0994	1	0,14581	-8,4406
	-19,7121	-4,858	1	11,7497	-13,3705	1	0,27057	-10,1915
	15,2583	-11,8286	1	-13,6098	-5,3764	1	0,22351	-8,4182

4. Outlook

A program for fast and reproducible data evaluation was developed and tested for corrosive copper/electrolyte systems, like tap water, NaCl–solutions with different concentrations (1M and 0.1M), ascorbic acid solution, ZnO suspension and 4–Methylimidazole. Even systems with much noise in the raw data were able to be processed, like shown in the case of the ZnO–suspension. All experiments were show also good reproducibility.

In this work a code for MATLAB was implemented for data processing and acquiring the linear fits used for the automated calculation of the point of intersection. The received plots and their coefficients of determination of around 0.9 show clearly the quality of the fits for the linear regression.

Nevertheless, there were some sets of not fully processed raw data caused by incorrect operation or by a bug in the program. The next step is to find and fix the bug of the implemented code.

Part II.

Electrolyte for All Solid State Batteries

5. Introduction and Background

5.1. Historical Approach

Modern day lithium secondary batteries have their origins in the 1960s and 1970s when the main energy source these days, oil, was short due to the first energy crises [23]. It was the first time people noticed fossil fuels were limited and so they were looking for ways to substitute these with new technologies to produce, store and convert energy. The use of fossil fuels also had big ecological disadvantages since burning oil, coal or gas leads to the emission of huge amounts of CO_2 and other pollutants into the atmosphere which plays an important role in global warming [24]. In addition to this ecological aspect, the interest in new mobile applications of energy grew larger and the demand of high power and energy batteries was born[25].

From theoretical considerations lithium based batteries were the most suitable to meet the given requirements since Li is the alkali metal that is both, the most electro positive ($-2.04V$ versus standard hydrogen electrode)and the lightest ($M = 6.94g/mol$ and $\rho = 0.534g/cm^3$) metal. It has also very high thermal and electrical conductivity and the highest specific heat of any solid element which makes it in total very favourable for energy storage systems [26]. It was used for primary batteries soon but for secondary batteries it wasn't suited because of safety risks related to dendrite growth during recharging leading to short circuits and considerable heat[27]. Since the electrolyte used was organic and flammable, Li metal as anode material could not be used in secondary batteries.

To overcome this problem the electrode or the anode or both needed to be modified, leading to researchers looking for new concepts and finding intercalation materials for anodes[28]. In the beginning it was believed that only two–dimensional materials (best would be layered–type materials) would work. Two examples of more or less working intercalation anodes are TiS_2[29] and alloys of Li with Al[30, p.1916]. TiS_2 was chosen for its layered structure and showed good cyclic properties[31], but still had the problem of dendrite growth while alloys with Al showed no dendrite growth at all but had bad cyclic properties due to extreme changes in its volume in charged and de-charged state. The discovery of the three–dimensional intercalation material V_6O_{13}[31] which has a framework structure showed that higher–dimensional intercalation structures also worked and new materials as electrodes were discovered by using this knowledge.

The concept of the Li–ion or rocking–chair technology was stated in the end of the 1980s and early 1990s based on the research of Murphy et. all. and solved the problem of dendrites[30]. The cause for this was the presence of Li in its ionic rather than its metallic form. But this was also combined with the disadvantage of higher potentials for the anode which led to the need for cathode materials with even higher potential, found

in layered or three-dimensional-type transition-metal oxides.

The second approach for solving the problems Li secondary batteries posed was to replace the liquid electrolyte. The first step was the use of dry polymer electrolyte, which led to Li solid polymer electrolyte (Li–SPE)batteries but required high operating temperatures thus making these batteries interesting only for non-portable devices. For combining the advantages of both fluid and polymer electrolyte, a Li hybrid polymer electrolyte was created consisting of a polymer matrix swollen with liquid solvent and a salt[32].

In 1991, the commercially available Li-ion battery was created by Sony Corporation which had a high potential as well as high gravimetric energy density[33]. Miniaturisation was the next step to take for the wider use of Li secondary batteries and this resulted in thin film batteries. Dependant of the company which produced the battery many different combinations of anode, electrolyte and cathode were available[34]. Lithium phosphonitroxide glass was developed and became the standard solid electrolyte for thin film batteries. The progress in polymer chemistry made it possible to develop Li–HPE batteries with many different shapes having the additional advantages of flexibility and lightness.

Today Li-ion batteries are used in many areas of application because of their high energy density and high potentials[**?**]. They are preferred for mobile devices like mobile phones and portable omputers and other high value electronic devices and have become a big topic for powering vehicles in form of hybrid or fully electrical engines as well. For this last application even higher potentials and higher gravimetric and volumetric energy densities are needed. There is also a necessity of further miniaturization which cannot be archived by liquid electrolytes. Also, the state of the art polymer–based films saturated with organic solvents state a safety risk because of the organic solvent they are mostly flammable and hazardous and they have a voltage limit due to their electrochemical stability.

The new challenge is to find a solid electrolyte with good Li^+ mobility and Li-ion conductivity, no mentionable electric conductivity and chemical inertness toward outer factors (e.g. humidity and atmospheric gases) and and the electrodes. Especially the inertness toward Lithium-metal is really important and in addition the electrolyte shouldn't change is volume due to phase transitions at the operation temperature range and shouldn't degenerate over time[35].

Only a small group of materials show the desired properties[36]. Garnet structures containing lithium of the formula $Li_xM_2M'_3O_{12}$ are one of these few materials and have been gaining attention in this field of application. They show high ionic conductivity values of around $10^{-4}Scm^{-1}$ at room temperature and are insulators for electronic conduction [37].

5.2. Lithium Lanthanum Zirconium Oxide (LLZO)

The garnet-type $Li_7La_3Zr_2O_{12}$ (LLZO)[37] is used as a solid electrolyte and is known to occur in a low-conducting tetragonal and a high conducting cubic phase [38], with the ionic conductivity differing by two orders of magnitude. It shows great stability against Li metal and the as a cathode material commonly used $LiCoO_2$ and the band gap of about 5 V makes this material a bad electronic conductor. Because of this, LLZO is a promising material.

The tetragonal LLZO is the theoretically stable structure of pure LLZO while the cubic structure is attained by stabilisation through doping. This originally happened without the intention to do so by contamination from the alumina–oxide–crucibles. It was found, that Al-ions penetrated the LLZO powder at higher temperatures and thus stabilized the cubic face, leading to a drastic increase in ionic conductivity [39].

For the all solid–state batteries LLZO doped with Ga was used. This doping is known in Literature [40][41][42][43].

Since the ionic conductivity is influenced by the diffusion of Li ions in the structure different kind of doping can give even higher ionic conduction when the following three thoughts are considered [44][45][46]:

- If there are ions with large radii in the structure, the lattice parameters get bigger, leading to Li being able to move easier and faster
- By introducing some elements, vacancies can be introduced to the structure leading to higher mobility of the Li ions
- A low oxidation state of doping elements leads to an increase of Li in the structure, forming a Li–stuffed garnet structure.

5.2.1. Synthesis

There are two by literature commonly known ways to synthesize LLZO, the synthesis from solid oxides and the synthesis from nitrates and metal–organic precursors.

The first way is a typical solid–state synthesis with metal–oxides as precursors. The advantages are the high availability of the metal–oxides and their generally good stability. The synthesis is done by mixing the powders by grinding or ball–milling without or better with solvent. The calcination temperature is usually higher than with nitrates as precursors and the resulting powders normally have bigger grain size.

The second method is named after Pechini and has nitrates or metal–organic precursors which are dissolved in a solvent and often complexing agents, like citric acid, are added. After stirring the mixture for a while the solvent is evaporated and the resulting powder is used for calcination, which can usually be done at lower temperatures than with metal–oxide precursors. This results in smaller grain size. A disadvantage is the availability

and the stability of the precursors. Nitrates are often hygroscopic and metal–organic components can be degenerating because of oxygen and humidity over time. Another disadvantage is the release of nitrogen oxides while heating.

6. Methods and Materials

The samples were prepared by a synthesis method developed on base of the Pechini method. The details are given in the section Work–flow. For characterisation of the synthesized powders, Powder–X–Ray Diffraction was used and for the measurement of the ionic conductivity Electrochemical Impedance Spectroscopy was used. Furthermore, Secondary Electron Microscopy was done on chosen samples to get further information on the sample while Thermal Gravimetric Analysis was used to get a better understanding of the calcining process of the LLZO with new dopant.

6.1. Standard Work–flow

Most of the time a standardized Work–Flow was used for the preparation of the samples for getting reproducible results. Changes in this Work–Flow where made when problems were encountered and are pointed out at the crucial parts in the result chapter.

6.1.1. Powder Synthesis

For the powder synthesis, a modified Pechini synthesis was used. The reactants were nitrides or metal–organic precursors. For 0.1 Mol of LLZO the the following synthesis steps were done:

→ 200 mL deionized water where added and the solution was stirred at $65°C$ with a stirring speed of 400 rounds per minute for 15 minutes.

→ 100 mL ethanol (p.a.) were added and the mixture was stirred for 30 minutes.

→ 150 mL ethanol (p.a.) were added, the solution was heated to $70°C$ and stirred for 2 h.

→ 150 mL ethanol (p.a.) were added and the temperature was raised to $95°C$ and the stirrer turned down to 100–200 rounds per minute. Like this the solvent was evaporated over night.

→ On the next day the powder was grinded and dried for at least six hours on a heating plate at $95°C$.

→ The raw powder was then filled into glas flasks and stored under nitrogen.

For the synthesis of undoped LLZO the solution was murky after the addition of water and became clear when ethanol was first added. The colour of the raw powder varied from white to yellowish.

6.1.2. Calcining

The calcining was done in a box furnace (RT-1100°C). The gas used for flushing during the calcination was synthetic air for Al_2O_3–crucibles and nitrogen for glassy carbon–crucibles.

For undoped LLZO for up to 1.5 g a temperature of 670°C for 15 h with ramp rates of 3 K/min were used to attain the tetragonal phase. For bigger amounts of sample the Lanthanum Zirconium Oxide (LZO), a precursor of LLZO, was formed. With the addition of different dopants, the temperature to attain the desired product changed at unchanged calcination time and the ramp rate. The product was analysed by XRD.

6.1.3. Post–doping with Ga_2O_3

For post–doping 20 mol% of Ga in the form of Ga_2O_3 were added to the LLZO and grinded throughly. Afterwards the powder or the pellets pressed from this powder needed to be heated to at least 650°C (dependent on the original LLZO powder used) to obtain the cubic faced LLZO.

6.1.4. Pressing Pellets

Pellets were pressed in two steps, first with an uni–axial press and afterwards with a hydrostatic press.

For pellets with a diameter of 11 mm around 300 mg powder were used, while for pellets with a diameter of 13 mm around 500 mg of powder were used. The pellets were pressed at the uni–axial press at 35 kN for 2–3 minutes and bagged in two layers of plastic condoms without any air trapped inside. The hydrostatic press was operated at 1000 kN for 4–5 minutes.

6.1.5. Pellet Sintering

Pellets were sintered in Al_2O_3–crucibles at temperatures ranging from $800 - 1000°C$, depending on the dopant with a holding time of 8 h and a ramp rate of 3 K/min. As purging gas normally synthetic air was used. Afterwards the density of the pellet is measured and an XRD of the cover powder is made.

6.1.6. Pellet Preparation for Impedance Measurements

For impedance measurements the pellets were prepared by the following procedure:

- The pellet is sputtered with platinum at both sides.
- Afterwards, on top of the platinum sputtering, two layers of platinum paste (thinned with ethanol p.a.) are applied and the pellet is dried at 13 mbar for 30 min at 75°C.

- Platinum wires are fixated by a ceramic two component adhesive one on each side of the pellet and the construction is dried at the same temperature as before for 45 minutes to one hour.
- Both sides of the pellets are again painted with platinum paste dissolved in ethanol, with focus on the area where the platinum wire touches the pellet. The whole pellet with the wires is then dried again for around one hour.

6.2. Physical characterisation

6.2.1. X-Ray Diffraction (XRD)

X-rays are used to measure the density of electrons in a crystalline structure by diffraction. With the help of the diffraction pattern the crystal structure itself and the disorder can be estimated, but some additional knowledge about the composition of the sample is needed to fully characterise it.

To get a diffraction pattern, several conditions have to be fulfilled. One is the existence of some kind of crystalline order in the sample and the other is the use of X-rays with the right wavelength for analysis. The wavelength has to be in the same order of magnitude (1–100 angstroms) as the spacings in between the atomic layers of the sample. If these conditions are met it comes to a pattern formed from constructive and destructive interference, occurring in specified directions described by Bragg's law (also see Figure 6.1):

$$2 * d * sin\theta = n * \lambda \tag{6.1}$$

For this work a transmission powder XRD with a copper radiation of 1.54060 $\AA$ and a curved germanium (111) monochromator was used. The generator was operated at 40 kV and 35 mA.

6.2.2. Scanning Electron Microscope (SEM)

The Scanning Electron Microscope is a microscope where the image is produced by scanning the sample with a focused electron beam and getting information from signals produced from this effect. Common available machines are able to image a sample by collecting secondary electrons and get elemental information via EDX. Another possibility would be analysing backscattered electrons or luminescence.

SEM is a very sensitive surface technique with which pictures with a resolution of less than 1 nm can be made by a raster scan pattern and also has some information on sample depth.

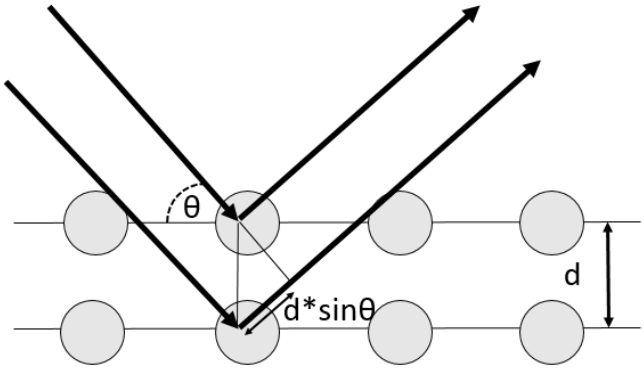

Figure 6.1.: Theoretic principle of XRD.

A little drawback of this technique is that only electronically conductive samples can be measured, because electronically isolating samples would get charged during the measurement process leading to strong repulsive interaction with the electrons of the scanning beam. Therefore electronically isolating samples have to be metallized before being measured. Usually this is done with a thin layer of sputtered gold.

6.2.3. Thermal Gravimetric Analysis (TGA)

TGA is a analytical method which measures the mass of a sample as a function of temperature. The parameters are the amount of sample used, the temperature range and the heating rate. It gives information about physical phenomena like vaporization, sublimation, absorption, adsorption or desorption and chemical phenomena like chemisorption, desolvation and decomposition and gas releasing reactions (e.g. CO_2 release from a carboxylic acid). In many cases this analysis is coupled to a infrared spectroscopy cell or to a mass analyser to get more information about released gases and decomposition products.

The TGA used during this work doesn't have other analytical methods coupled. Dilatometry curves were recorded with a TA Instruments DIL 806 optical dilatometer at a constant heating rate of 10 K/min.

6.3. Electrochemical characterisation

6.3.1. Electrochemical Impedance Spectroscopy)

Electrochemical impedance spectroscopy (EIS) is a tool for investigating the electrical and electrochemical properties of materials by comparing the behaviour of the real system

to a model system made up of defined circuit elements like resistors, capacitors and inductors. The elements in the model system represent physical properties in the observed sample and the results of the measurement can often be related to complex materials variables– e.g. mass transport, chemical reactions, corrosion and dielectric properties. EIS is a standard analysis method in industrial quality control for paints, emulsions, electroplating, thin–film technology and more. In scientific research it is amongst others used for battery characterisation.

The measurement itself is simple and automated but the interpretation of the data is often non–trivial and the requirements for the measured system are high. There are three types of IS measurement approaches with different electrical stimuli used. The most used one is to apply a single-frequency voltage or current and measuring the response of the system by determining the phase shift and amplitude of the resulting current. It is important to work with small signals, resulting in having linear behaviour, so that the modelling with ideal circuit elements is acceptable. Since there is normally more than one model circuit that describes the system it is important to think carefully about the elements used in the model circuit and what process they stand for. Good results can be attained by good experiment design combined with varying measuring parameters and combining the results archived from this method with results from other measurement methods, e.g. SEM or AFM.

Common IS measurement systems determine Z as a function of ω over a large frequency range and the phase difference φ between the voltage and the current. The impedance is often plotted in form of the Nyquist Plot where the real and the imaginary part of the impedance are plotted (Figure 6.2). These parts are calculated through

$$Re(Z) = |Z| * cos(\varphi) \tag{6.2}$$

and

$$Im(Z) = |Z| * sin(\varphi). \tag{6.3}$$

.

In this work the impedance measurement system Gamry Reference 600 was used in both potentiostatic and galvanostatic mode. The software for data evaluation and fitting the equivalent circuits was ZVeiw (Scribner Electronics).

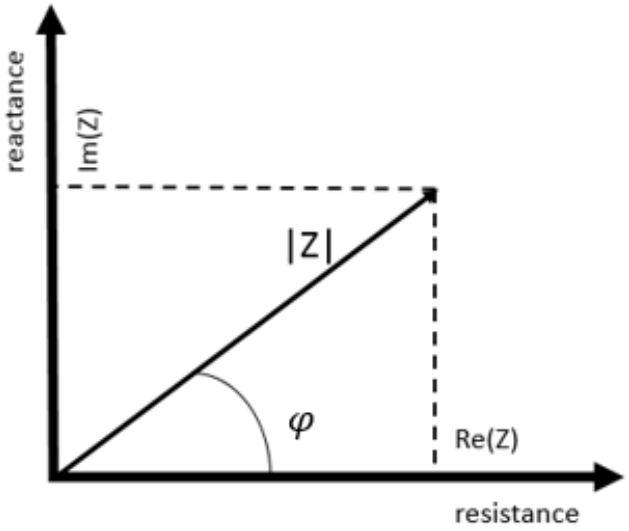

Figure 6.2.: Nyquist Plot

6.4. Chemicals

- **Lithium Nitrate** (99,995%)
  CAS–No.:7790–69–4
  Merk
- **Lanthanum(III)nitrate hexahydrate** (99,995%-trace metal basis)
  CAS–No.:10277–43–7
  Acros Organics
- **Zirconium 2,4-pentanedionate**
  CAS–No.:17501–44–9
  ABCR GmbH & Co.KG
- **Sodium Nitrate** (puriss. p.a. ISO ≥99,5%)
  CAS–No.:7631–99–4
  Sigma Aldrich
- **Zirconium(IV)ethoxide** (99+%)
  CAS–No.:18267–08–8
  STREM CHEMICALS
- **Zirconium(IV)acetylacetonate** (98%)

CAS–No.:17501–44–9
abcr GmbH

- **Gallium(III)oxide** (puriss, made out of Ga 99.99%)
  CAS–No.:12024–21–4
  Fluka Chemie AG

- **Calcium nitrate tetrahydrate** (99%)
  CAS–No.:13477–34–4
  abcr GmbH & Co.KG

- **Ethanol** (pusiss, p.A. $\geq$ 99.8%)
  CAS–No.:64–17–5
  Sigma Aldrich GmbH

7. Results and Discussion

7.1. Sol–Gel Synthesis

Sol–gel synthesis is used in many areas of applications, among other things to produce solids with small particle size. The synthesis normally used, the Pechini method, is a deviation of a sol–gel synthesis. To decrease the particle size even further the idea to try a traditional sol–gel synthesis was executed [47].

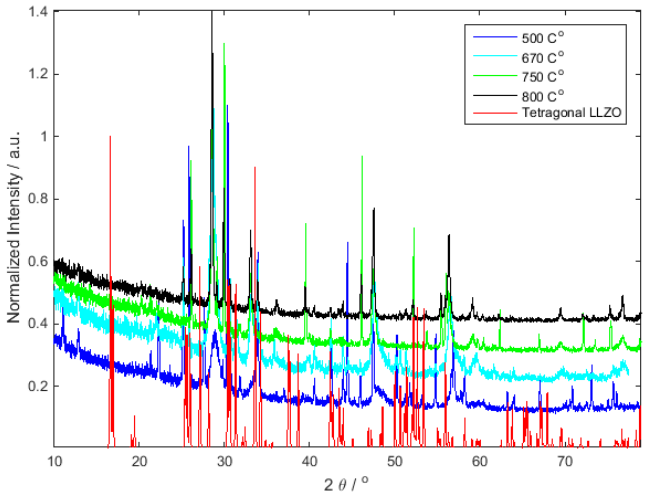

Figure 7.1.: XRD of the calcined sol–gel powders and the XRD pattern of the tetragonal phase of LLZO for comparison. All patterns are normalized in intensity and the sol–gel powders and are shifted in y–direction by 0.1 a.u. for better visibility.

LLZO without any dopant should be synthesized with propionic acid being the solvent and acting as chelating agent. 0.005 mol of product were synthesized. The procedure was as described below:

- $Li(NO_3)$ and $La(NO_3)_3 * 6H_2O$ were dissolved in about 5 mL of propionic acid and stirred for three hours in a closed glass bottle at 400 rpm at 80°C.
- $Zr(EtO)_4$ was dissolved in about 20 mL of propionic acid and stirred in a closed glass bottle for three hours at 400 rpm at 80°C.

- Afterwards the two solutions were combined and stirred for another hour in a closed bottle at $80°C$.
- 40 mL of deionized water were added to the solution and the solvent was evaporated at $95°C$ at the stirring speed of 170 rpm.

A white powder was obtained and calcined at four different temperatures: $500°C$, $670°C$, $750°C$ and $800°C$. The XRD of the attained powders are displayed in Figure 7.1.
In Figure 7.1 can be easily seen that the synthesis failed, since none of the patterns of the calcined powders are similar to the reference pattern. The calcination temperature was raised from $500°C$ to $800°C$ because at low temperature the precursor maybe would not have reacted completely, but when raising the temperature the XRD pattern of the attained powders did not change to the desired tetragonal LLZO. The only thing seen in Figure 7.1 is that the reflexes are broad at $500°C$ and getting narrower as the temperature increases. At $800°C$ all reflexes are sharp and narrow.

During calcining an abnormal foaming of the powder was observed. This led to fluffy powder that was looking like a sponge with a network of calcined powder and air in between. Because of this the amount of powder calcined in one run was very limited. There could have been impurities in one of the chemicals or the deionized water which led to this foaming and to not attaining the tetragonal LLZO. Another reason could be the evaporation of Li during calcining.

7.2. Na doped LLZO

To attain cubic faced LLZO, dopant elements are needed which for example change the lattice parameter or the number of Li vacancies. To find out if the change of lattice parameter alone can lead to cubic LLZO the Li–side was doped with sodium. If the cubic phase could be attained by only this doping than the change of the lattice parameter alone is sufficient, otherwise there has to be an additional condition met or the concentration or the dopant have to be changed.

For this short experiment 0.5 mol Na were doped, resulting in the composition of $Li_{6.5}Na_{0.5}La_3Zr_2O_{12}$. The calcination temperatures were chosen to be $765°C$ and $900°C$, since no cubic phase was attained at $765°C$. In Figure 7.2 the result of the XRD analysis can be seen. The LLZO is still tetragonal and the XRD pattern has additional reflexes compared to the tetragonal LLZO which indicate impurities. It was not possible to find out the composition and quantity of the impurities. Since the cubic phase could not be attained, the change of the lattice parameter only is not sufficient for the formation of cubic LLZO. Nevertheless, sodium as dopant is not completely useless. If the cubic face is already stabilized, sodium might be used to enlarge the crystal lattice and contribute in this way to higher ionic conductivity. This is possible since the ionic conductivity is caused by diffusion of Li–ions and diffusion is easier if the diffusion paths are bigger.

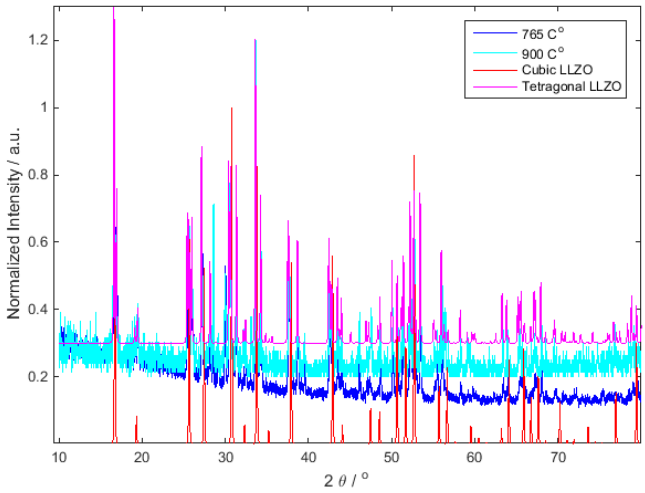

Figure 7.2.: XRD of the calcined Na doped LLZO powder at two different temperatures and the XRD pattern of the tetragonal and cubic phase of LLZO for comparison. All patterns are normalized in intensity and are shifted in y–direction by 0.1 a.u. for better visibility.

7.3. Calcium–Doped and Calcium/Gallium–Doped LLZO

With the dopant calcium more than one concentration and synthesis way was tried. Calcium and gallium were both doped to exchange places with lanthanum, resulting in the chemical formula of $Li_wGa_xCa_yLa_zZr_2O_{12}$ for the product. To test if only calcium is sufficient to create cubic face LLZO one synthesis was done with only calcium as dopant. Afterwards the product could also be post–doped with gallium.

7.3.1. $Li_{7.2}Ca_{0.2}La_{2.8}Zr_2O_{12}$

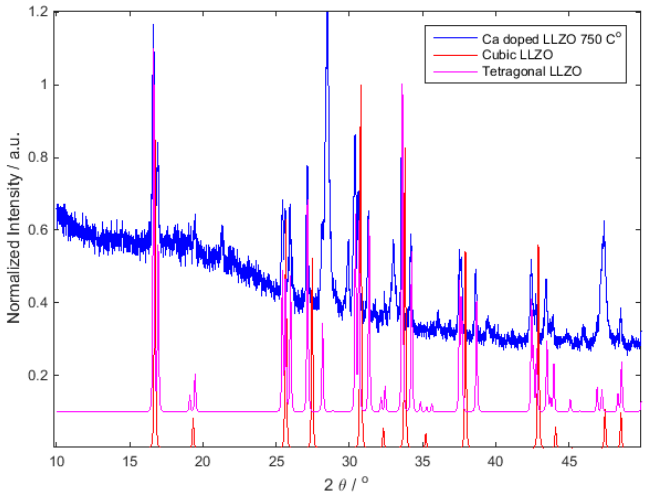

Figure 7.3.: XRD of the calcined Ca doped LLZO powder at 750°C and the XRD pattern of the tetragonal and cubic phase of LLZO for comparison. All patterns are normalized in intensity and are shifted in y–direction by 0.1 a.u. for better visibility.

0.005 mol of $Li_{7.2}Ca_{0.2}La_{2.8}Zr_2O_{12}$ were synthesized by the normal method described in the work–flow in the experimental part. $Ca(OH)_2$ was used right from the start of the synthesis to introduce calcium into the product.

Figure 7.5 shows the XRD pattern of the Ca doped LLZO after calcining at 750°C. The XRD shows many impurities and a still tetragonal LLZO. The impurities are most likely a combination of substances. Reflexes belonging to lanthanum zirconium oxide could be found, but there are still reflexes which cannot be identified. The impurities are likely to come from the $Ca(NO_3)_2$ which was from an old batch and already changed colour from pure white to light brown. It can be that the impurities prevent the conversion into the cubic phase, which was tested by the already known post–doping with Ga_2O_3. In Figure 7.6 the XRD of the post–doped (0.5 mol Ga per formula unit) and calcined Ca–LLZO powder is shown. The phase of the LLZO changed to cubic structure which is visible especially in the area of $16 - 17°$, where the double reflex from the tetragonal

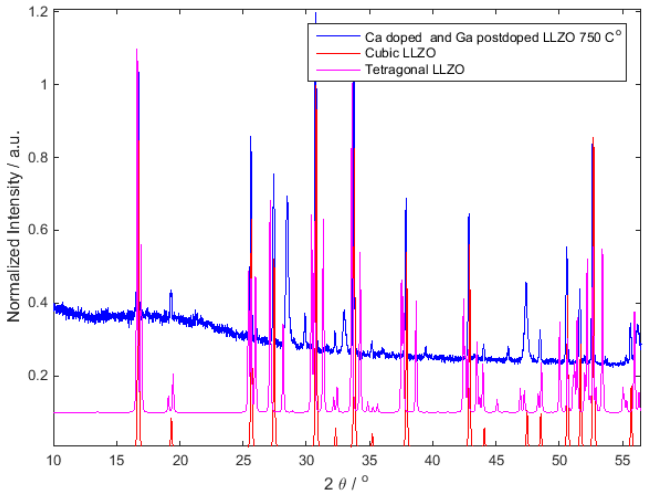

Figure 7.4.: XRD of the two times at 750°C calcined Ca doped and Ga postdoped LLZO powder and the XRD pattern of the tetragonal and cubic phase of LLZO for comparison. All patterns are normalized in intensity and are shifted in y–direction by 0.1 a.u. for better visibility.

phase changes to one, and in the area of 25 to 35°, where the cubic phase has four big, characteristic reflexes.

Even though there are many impurities the phase transition is still able to take place. This concludes that calcium alone is not able to change the face of LLZO from tetragonal to cubic, when applied in the concentration of 0.2 per formula unit.

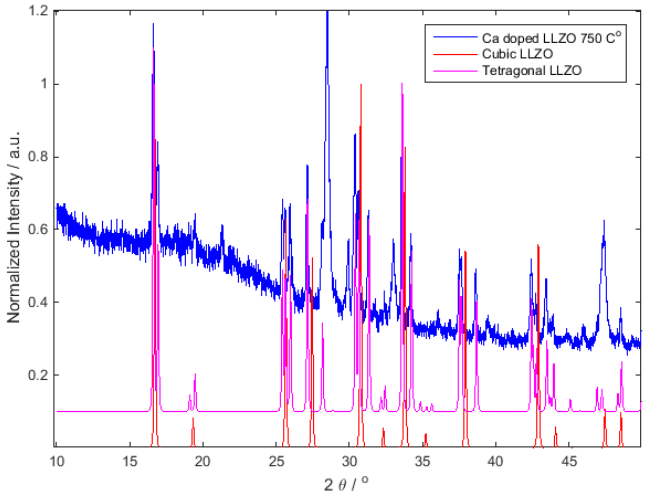

Figure 7.5.: XRD of the calcined Ca doped LLZO powder at 750°C and the XRD pattern of the tetragonal and cubic phase of LLZO for comparison. All patterns are normalized in intensity and are shifted in y–direction by 0.1 a.u. for better visibility.

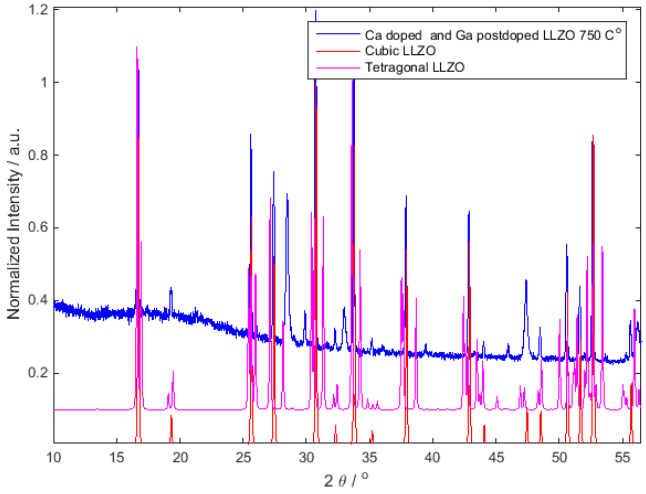

Figure 7.6.: XRD of the two times at 750°C calcined Ca doped and Ga postdoped LLZO powder and the XRD pattern of the tetragonal and cubic phase of LLZO for comparison. All patterns are normalized in intensity and are shifted in y–direction by 0.1 a.u. for better visibility.

7.3.2. $Li_{6.9}Ga_{0.2}Ca_{0.5}La_{2.8}Zr_2O_{12}$

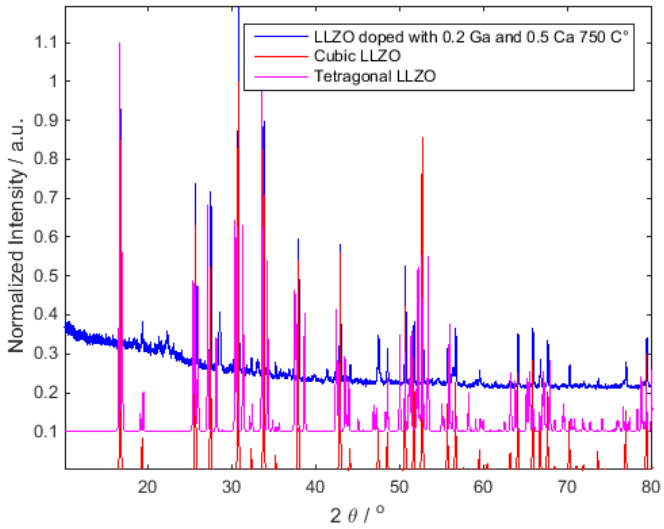

Figure 7.7.: XRD of the calcined $Li_{6.9}Ga_{0.2}Ca_{0.5}La_{2.8}Zr_2O_{12}$ powder at $750°C$ and the XRD pattern of the tetragonal and cubic phase of LLZO for comparison. All patterns are normalized in intensity and are shifted in y–direction by 0.1 a.u. for better visibility

For $Li_{6.9}Ga_{0.2}Ca_{0.5}La_{2.8}Zr_2O_{12}$ the dopant elements were added right from the start of the synthesis in form of $Ca(NO_3)_2$ and Ga_2O_3. Since the same chemical as a Ca–source was used as in the experiment described above, impurities are found in the product too.

The resulting product is a LLZO with cubic phase, as can be seen in Figure 7.7. The reflexes are sharp which indicates big crystallites.

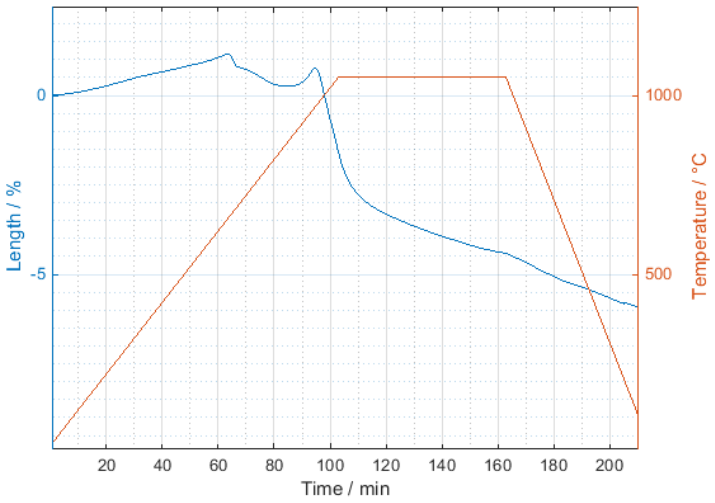

Figure 7.8.: Dilatometry data of a pellet of $Li_{6.9}Ga_{0.2}Ca_{0.5}La_{2.8}Zr_2O_{12}$. The powder for the dilatormatry was pressed from powder calcined at 650°C.

In Figure 7.8 the data from the dilatometry of a pellet made with powder calcined at 750°C is shown. The sintering process, where the pellet is getting smaller, starts at around 700°C. The peak near 900°C can indicate a phase transition which is combined with a volume expansion. After this peak the length of the pellet decreases steadily and the pellet is sintering. In further studies there should be more attention paid to the phase transition. In literature it is known that cubic LLZO can exist in two slightly different forms, a low–temperature and a high–temperature one. The result of the dilatometry is indicating that there is this kind of transition at around 900°C.

7.3.3. $Li_6Ga_{0.5}Ca_{0.5}La_{2.5}Zr_2O_{12}$

$Li_6Ga_{0.5}Ca_{0.5}La_{2.5}Zr_2O_{12}$ was synthesised similar to $Li_{6.9}Ga_{0.2}Ca_{0.5}La_{2.8}Zr_2O_{12}$ in one step using $Ca(OH)_2$ as a precursor to induce Ca to the structure. Therefore the end product also is not fully pure phase. The calcination was done at 765°C and leads to a cubic phase with sharp reflexes. The XRD pattern does not change even after the sintering process at 925°C. The XRD pattern in Figure 7.9 shows the pattern of the cover powder near the pellet after sintering at 925°C.

To find out if the Ca and the Ga are distributed evenly in the synthesized powder, EDX was performed on the calcined powder. In Figure 7.10 the result of the measurement is shown. The left and the middle image show the distribution of Ca and Ga respectively while the right picture shows the EDX where the signals of the elements O(blue), Ca(pink), Ga(yellow), Zr(green) and La(red) are plotted in the same image. From Figure

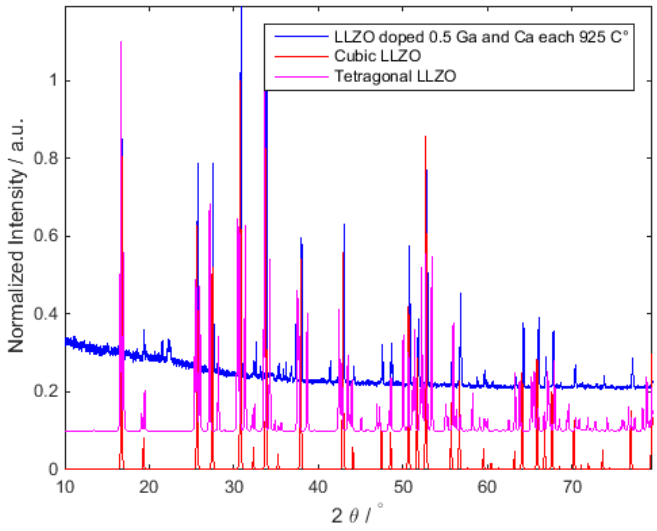

Figure 7.9.: XRD of the sintered $Li_6Ga_{0.5}Ca_{0.5}La_{2.5}Zr_2O_{12}$ powder at $925°C$ and the XRD pattern of the tetragonal and cubic phase of LLZO for comparison. All patterns are normalized in intensity and are shifted in y–direction by 0.1 a.u. for better visibility.

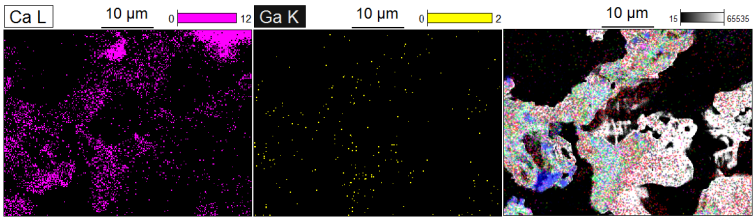

Figure 7.10.: EDX of the calcined $Li_6Ga_{0.5}Ca_{0.5}La_{2.5}Zr_2O_{12}$ powder.

7.10it becomes evident, that the elements Ga and Ca are evenly distributed.

In Figure 7.11 the powder after calcining at $765°C$ is shown. The crystallite size is in the order of micrometers which explains the sharp peaks in the XRD pattern. The surface of the grains are normally smooth but on some grains there are impurities visible on top of the grains. These impurities are most likely the ones seen in the XRD pattern.

Figure 7.12 shows the result of the dilatometry measurement of a pellet made out of $Li_{6.9}Ga_{0.2}Ca_{0.5}La_{2.8}Zr_2O_{12}$. Up to around $900°C$ the sample shows regular heat expansion. Afterwards, up to $1050°C$, the sintering process is taking place. Then the length is getting bigger again, indicating a phase transition or change in the sample, and settles down at -8% of length change. The decrease in length happening afterwards is the normal process of thermal contraction when the sample is cooling down. It is possible that

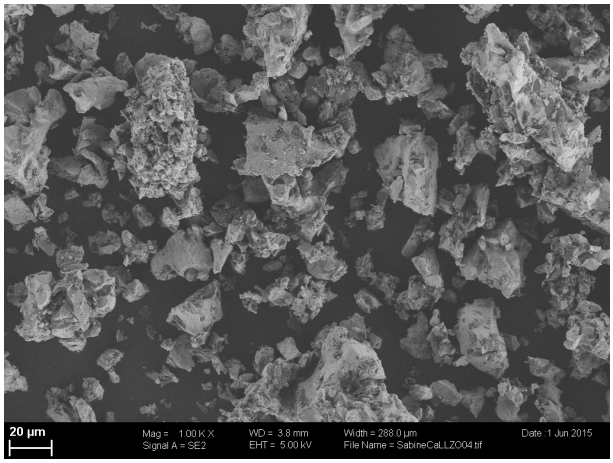

Figure 7.11.: SEM of the calcined $Li_6Ga_{0.5}Ca_{0.5}La_{2.5}Zr_2O_{12}$ powder.

the observed phase transition is caused by the impurities in the powder. Through the information gained by the dilatometry, a temperature above $900°C$ but less than $1050°C$ should be chosen for sintering.

A pellet made out of $Li_6Ga_{0.5}Ca_{0.5}La_{2.5}Zr_2O_{12}$ was sintered at $925°C$ for 8 h. The theoretical density was 79,98 %, which is not as high as desired. The impurities are probably the cause for the pellet being not dense. It is possible that they prevent the complete sintering by blocking the process at the grain boundaries.

This pellet was used for determining the activation energy by measuring the impedance at different temperatures from room temperature up to $250°C$ in steps of around $25°C$ or $50°C$. The bulk resistance was determined with the help of an equivalent circuit and the inverse temperature was plotted against the logarithm of the conductivity times temperature. In Table 7.1 the raw data used to make the Figure 7.14 is given.

The impedance data was fitted with the circuit in Figure 7.13. The resistance *R1* is in this case equivalent to the bulk resistance. The error for this circuit element after fitting was normally below 3 %. The fitting of the data recorded while the sample was cooling down could be fitted better than the data taken when heating the sample. The error was smaller.

R2, *R3*,*CPE 2* and *CPE 3* represent the grain boundaries and diffusion controlled processes. The error for fitting these elements was generally high, up to 30 %. Since the semicircles in this sets of data were always overlapped greatly, this amount of error was expected. The single processes could not be separated sufficiently, therefore they were not used for elevation. The constant phase element *CPE 4* represents the phase boundary towards the electrode.

The activation energy calculated from this set of data is 0.31 eV for the data measured while heating the sample and 0.34 eV for the data measured while cooling the sample.

Table 7.1.: Data of the Arrhenius plot.

Heating		Cooling	
Temperature(K)	Resistance(Ω)	Temperature(K)	Resistance(Ω)
21,6	1050,0	263,6	9,4
21,6	1015,0	263,2	9,4
21,6	1016,0	263,0	9,5
53,0	521,8	207,5	24,7
53,0	534,7	207,5	24,7
53,0	513,9	207,5	24,6
101,1	153,2	153,9	51,3
101,1	154,9	153,9	51,3
101,1	156,7	153,9	51,3
157,8	52,4	98,9	137,3
157,8	52,5	98,8	137,1
157,8	52,7	98,9	136,5
210,9	23,6	52,8	556,8
210,9	23,6	51,8	578,4
210,9	23,7	50,3	602,5
263,6	9,4	30,5	1172,0
263,2	9,4	30,1	1189,0
263,0	9,5	29,6	1207,0

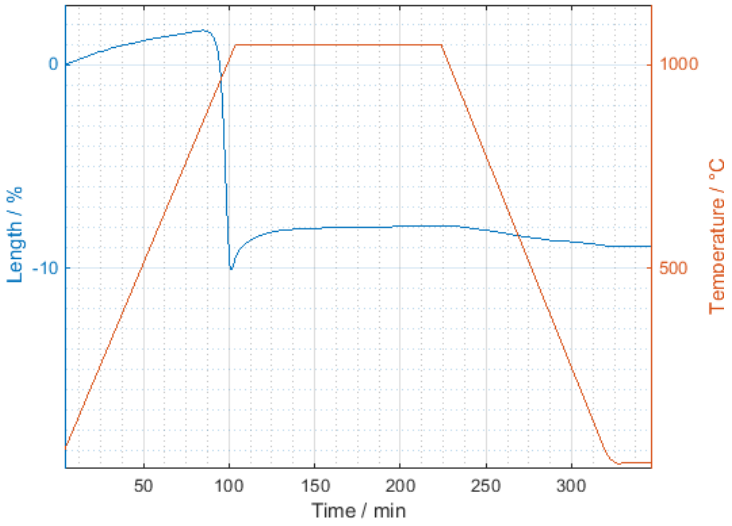

Figure 7.12.: Dilatometry data of a pellet of $Li_{6.9}Ga_{0.2}Ca_{0.5}La_{2.8}Zr_2O_{12}$. The powder for the dilatormatry was pressed from powder calcined at 765°C.

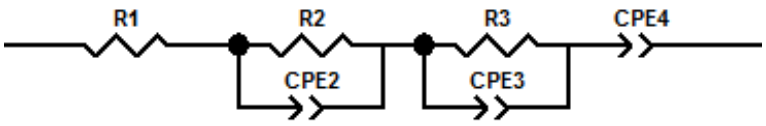

Figure 7.13.: Circuit used for fitting the impedance data.

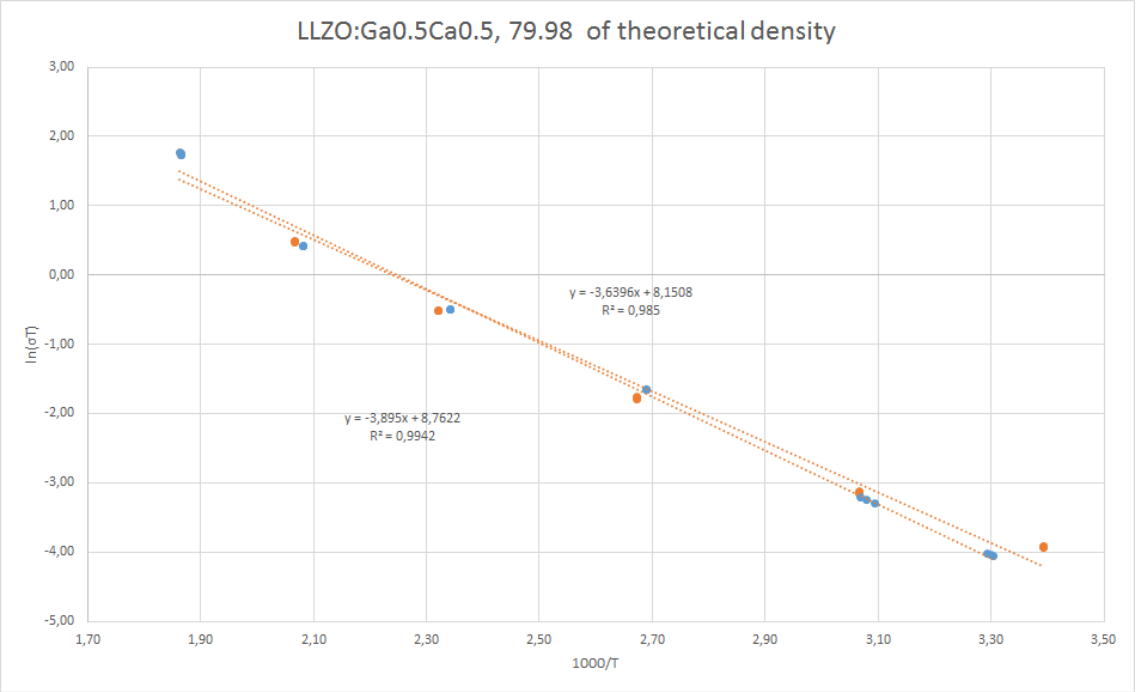

Figure 7.14.: Arrhenius plot from a pellet made out of $Li_6Ga_{0.5}Ca_{0.5}La_{2.5}Zr_2O_{12}$. The bulk resistance $R1$ was used for calculation.

7.4. Batteries

For the production of solid state batteries LLZO post–doped with 0.2 Ga per formula unit was used. For this LLZO without any doping was produced and post–doped after calcining at 670°C with Ga_2O_3 like described in the experimental part in the work–flow. The powder was then pressed into a pellet with a diameter of 13 mm.

The temperature for sintering the pellets was varied and is given for the pellets individually later on. None of the pellets was getting dense, the density was always much less than 80 %. After sintering, an XRD of the powder scratched from the surface of the pellet was made to ensure the quality of the pellet. The pellets always showed pure cubic phase like in Figure 7.15.

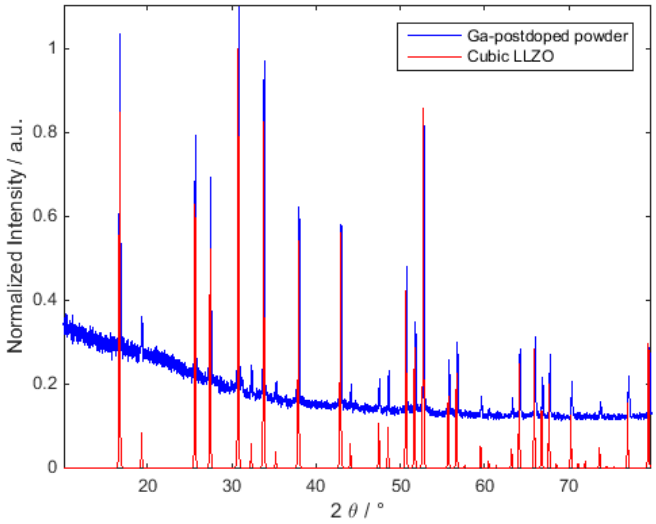

Figure 7.15.: Examplary XRD of the sintered powder.

The density was calculated by measuring the thickness, the diameter and the mass of the pellet and using the formula:

$$Density = Mass/((Diameter/2)^2 * \pi * Thickness) \tag{7.1}$$

Diameter and thickness of the pellet were given in cm, the mass was given in g.

Afterwards the pellet was thinned with the use of sandpaper(P1800) from both sides till the remaining thickness was around 0,5 mm. Before treating it further, the pellet was dried for at least one hour at 50°C and 13 mbar and the weight was measured once more after cooling down to room temperature.

For the electrode of the solid state battery a slurry made out of electrode material, post–doped LLZO(same material as the pellet), PVDF (polyvinylidene fluoride) and SuperCarb (activated carbon) was used. The following procedure was used to produce the composite slurry:

→ 50 mg electrode material, 50 mg post–doped LLZO, 10 mg PVDF and 10 mg SuperCarb were mixed thoroughly in a mortar. The exact weight used of every component was written down and the composite was given into a glass flask.

→ Around 1 mL of a solvent(normally a mixture of THF and toluene(4:1)) was added to the composite and the slurry was stirred with the tip of the glass pipette.

→ The gas area in the glass flask was filled with nitrogen and the flask was closed air–tight.

→ The sealed flask was put in an ultrasonic bath at room temperature for 45–60 min.

To produce the solid state batteries the slurry was given on top of the thinned and dried pellet and after around 30 seconds the slurry on top of the pellet was pressed to the pellet with the thumb through a layer of weighting paper. Afterwards, the pellet with the slurry on top was dried at $50°C$ and 13 mbar for at least one hour. The weight of the pellet was than measured after the pellet cooled down to room temperature. From the difference in mass here and from the weighing before the slurry was applied, the mass of the slurry on the pellet was determined. Also, the active mass(electrode material) on the pellet could be calculated.

The assembling of the battery happened in the glove box in an oxygen– and water–free argon atmosphere. In Figure 7.16 the cell used for the battery assembly is shown. The red contact at the bottom is the cathodic contact, the green one on top is the anodic contact. The steps for assembling the battery are listed below:

→ With a cutter(Nr.6) a disk was cut out of a Li–foil

→ The Li–disk was then flattened by pressing it with the help of a knife and then cleaned by scratching the surface on both sides of the Li–disk till the Li was shiny and not dull any more.

→ The Li–disk was put centric on the anodic stamp and pressed to the stamp till it would not fall off any more. The Li–foil on the stamp needed to be flat.

→ The pellet was placed on top of the Li–disk on the stamp with the side toward the Li–foil where no slurry was placed.

→ The current collector for the cathodic side was placed on one end of a plastic cylinder and this construction was put over the stamp. The current collector was touching the slurry.

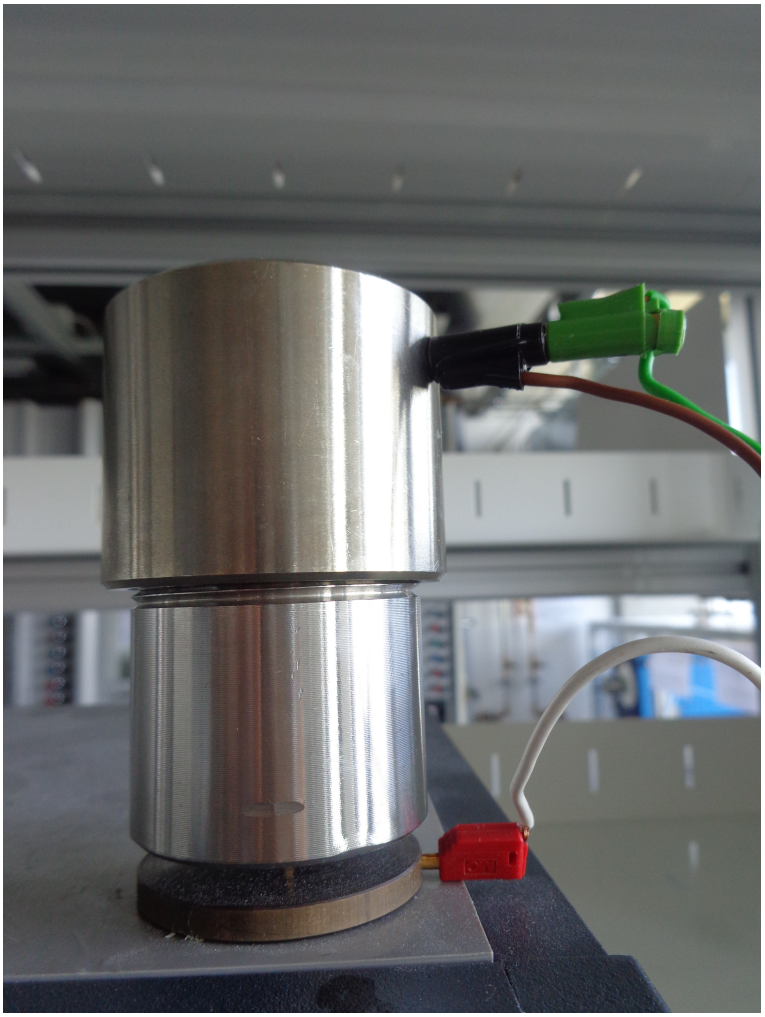

Figure 7.16.: Cell used for assembly of the battery.

→ The stamp was put in the cell up–side–down. The current collector was now on the bottom and the stamp was on top.

→ A spring was attached on top of the stamp and a plastic isolation was put on top of the bottom part of the cell. Afterwards, the cell was closed tightly.

After assembling, the cell was measured with the help of the program Battery Cycler. First, cycling at room temperature was tried. If this was not possible, the battery was heated to $95°C$ and measured at this temperature.

7.4.1. $LiCoO_2$ as cathode material

The well-known cathode material $LiCoO_2$ has a theoretical energy density of 140 mAh/g[36].

Battery 1(SRSA07)

The pellet for this battery was sintered at $1010°C$ for 15 hours. From the mass loss of the pellet, loss of Li is expected. The density after sintering was only $2.74g/cm^3$, which is around 54 % of the theoretical density of $5.1g/cm^3$.

The pellet and the slurry were completely compared outside of the glove box. The solvent was evaporating fast and fine cracks could be seen on the surface of the half–dried slurry. After pressing the slurry with the weighting paper and the thumb, the cracks were not visible any more. After drying, the total amount of slurry on the pellet was 3 mg, 1.25 mg of this being the active material $LiCoO_2$.

The OCV(open circuit voltage) at room temperature was fluctuating strongly and charging the battery was not possible. Since this effect was most likely caused by the high resistance of the battery, the whole battery was heated up to $95°C$ to lessen the resistance. At $95°C$ charging and discharging the battery was possible.

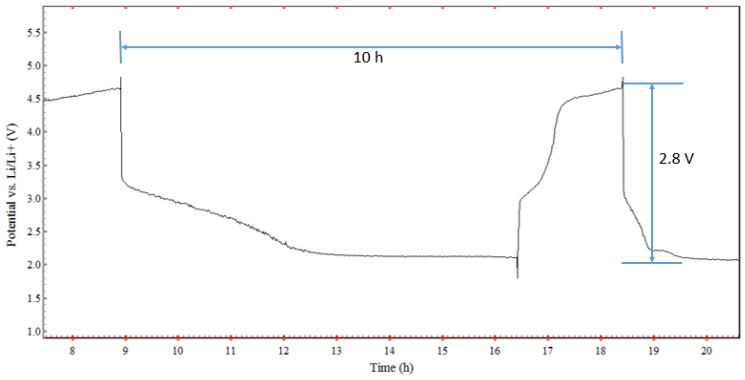

Figure 7.17.: First cycle of the battery at $95°C$.

Figure 7.17 shows the first cycle of the battery at $95°C$. The battery was cycled in the range of 2.0 V to 4.8 V against Li/Li^+ with 3.125 $\mu A and -3.125 \mu A respectively. A full charge needed 10 hours.$

After cycling the battery, impedance measurements were performed at $95°C$. The measurement was done when the battery was charged and discharged respectively. Figure 7.18 shows representative measurement data. The black line belongs to the charged state of the battery, while the red one belongs to the discharged state. The biggest difference between these two states is visible at the right side of the figure in the area where the interface towards the electrode takes effect. This measurement was only analysed qualitatively.

It is possible that on this interface a space–charge is formed. This would explain why the imaginary resistance is so much higher in case the battery is charged. For a capac-

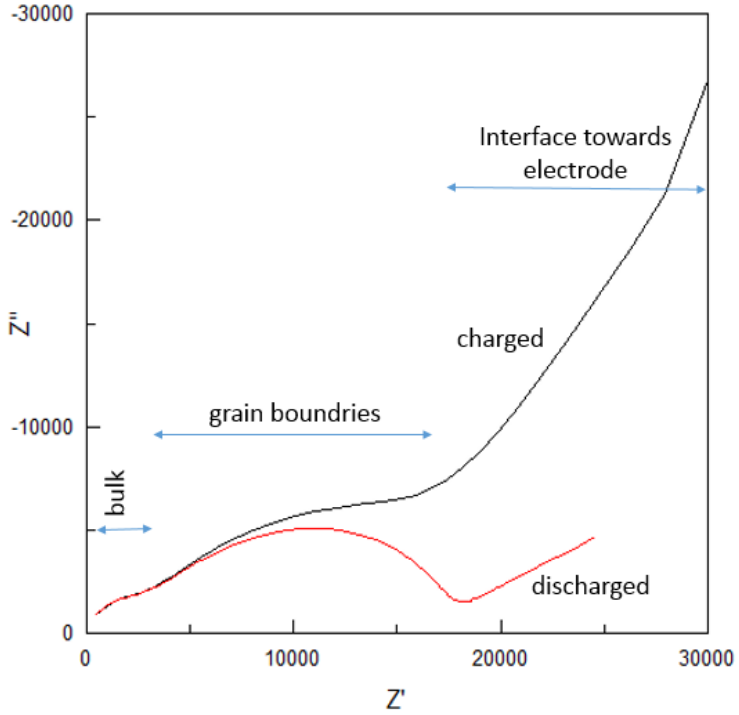

Figure 7.18.: Impedance result measured at 95°C.

itor the imaginary resistance is high, while an ohmic resistor only has a real resistance. Similar to a capacitor the charges are separated in this space–charge along the boundary of the electrode and the electrolyte.

In literature, the formation of a high resistance interface of Li_2CO_3 is mentioned. After the cycling of the battery and impedance measurements, the pellet was retrieved from the battery and analysed in SEM. For this analysis the pellet was broken in two pieces and the interface was analysed.

In Figure 7.19 one half of the pellet is shown. Marked with the red square is the composite on top of the pellet. On the right side of the slurry the pellet itself is seen. It is clearly visible that the structure of composite and pellet are different. The slurry is one mass without much air trapped while the pellet is porous. This was expected since the pellet only had a density of around 54 %. Normally dense pellets are preferred but in this case the porous surface of the pellet could have helped to make the interaction surface of pellet and composite bigger. Since the composite stayed on top of the pellet even after cycling, the adhesion between composite and pellet was good.

In case of this battery, no Li_2CO_3-Layer between composite and pellet could be found. It would be visible as a layer in a different shade of grey in the SEM picture. This was

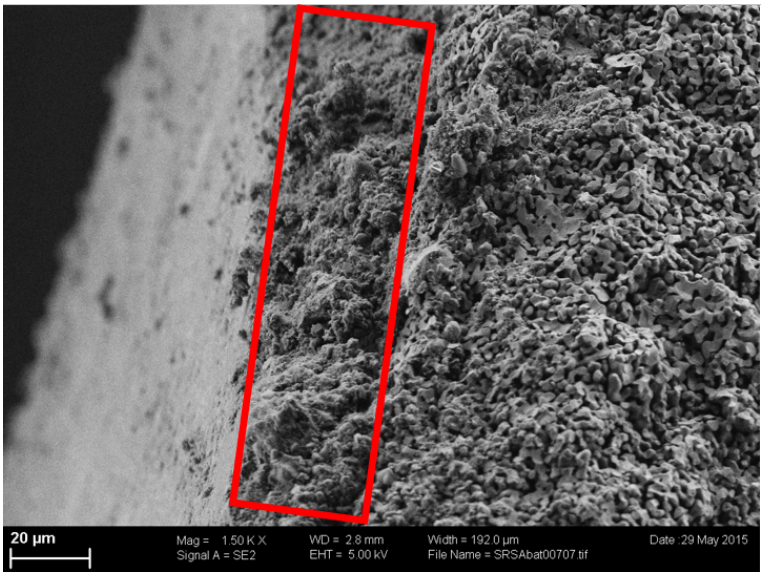

Figure 7.19.: SEM picture of the pellet after cycling in the battery.

not observed.

All in all, the proof of concept that all solid state batteries could be made is done with this battery. The battery was also able to light a LED after the cycling and impedance measurements were performed!

Battery 2(SRSA11P4)

The pellet for this battery was sintered at $975°C$ for 8 hours. Afterwards the pellet had a density of $3.63 g/cm^3$, which is round 71 % of the theoretical density.

The pellet was thinned in the glove box. The slurry was done like described above, but NMP was used as solvent. This solvent was chosen since it evaporates slower than the mixture of THF and toluene. When the slurry contains the solvents THF and toluene, the slurry cracks on top of the pellet while drying. To avoid this, a solvent that is evaporating slower might help. For this reason, NMP was tested on this pellet. Even though the drying process was now slower, the cracking was still occurring. There was no visible improvement in comparison to the mixture of THF and toluene.

Applying the slurry on top of the pellet was done outside of the glove box. After drying, the total amount of slurry on the pellet was 6 mg, 2.56 mg being the active material $LiCoO_2$.

The battery showed a fluctuating OCV(open circuit voltage) of around 2.9 V at room

temperature and a stable open circuit voltage of 2.7870 V at $95°C$. The battery was cycled between 2 V and 4.8 V with 2.560 $\mu A and -1.280 \mu A. The battery needed 4.3 hours to fully charge for the fir$

One reason for this could be that the pellet for this battery had a higher density and was not as porous as the previous one. This could lead to less charge exchange area between composite and pellet. It could also be that the solvent used for the slurry had an influence on the final performance of the battery. This could be done by changing the composite structure, for example when different components of the composite had different solubility. Then the components of the composite would be separated and the idea behind the composite would not be met any more.

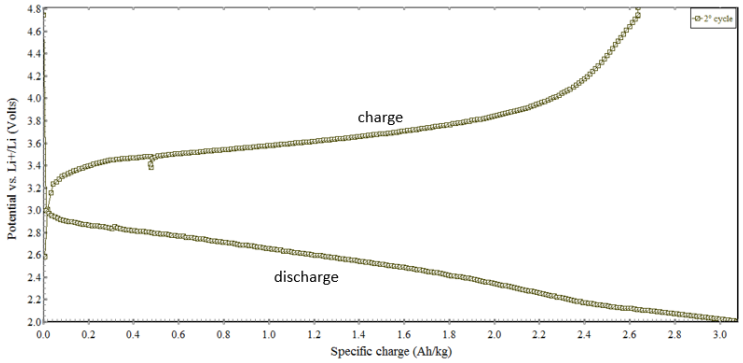

Figure 7.20.: Potential(vs. Li/Li^+) against specific charge.

In Figure 7.20 a typical cycle of the battery is shown.

Heat treatment after applying the slurry

If Li_2CO_3 was formed and would make the resistance at the boundary electrolyte to electrode higher, then heating the pellet up to at least $732°C$ and no more contact to CO_2 afterwards would increase the performance of the battery.

This idea did not work out as can be seen in Figure 7.21. The side where the composite was applied is not visible. On the side, where no composite was applied, the pellet was coloured light blue, a colour cobalt ions can take in the oxidation state of $II+$.

7.4.2. $LiFePO_4$ as cathode materials

The second material used for the batteries was $LiFEPO_4$, which is also known to literature and has a theoretical energy density of 170 mAh/g[36].

Battery 3(SRSA08)

The pellet for this battery was sintered at $985°C$ for 10 hours. Afterwards the pellet had a density of $3.79 g/cm^3$, which is round 73 % of the theoretical density.

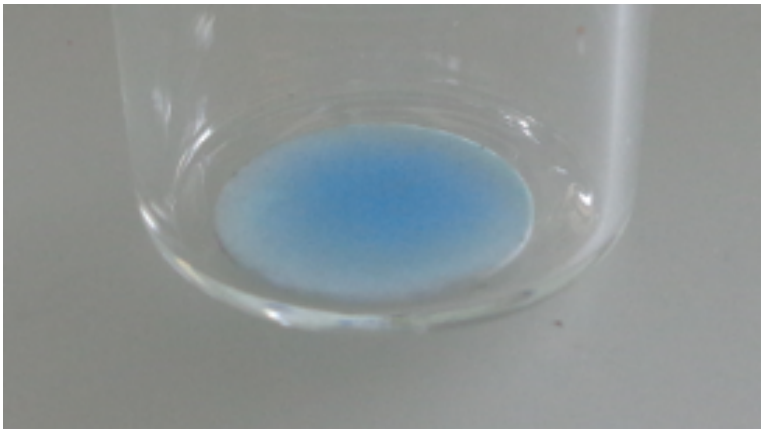

Figure 7.21.: Picture of pellet with composite after heating. The composite was applied to the side not visible in the picture.

The pellet was thinned in the glove box and applying the slurry on top of the pellet was done in the glove box as well. The surface of the pellet was never exposed to air during the process of battery making. After drying, the total amount of slurry on the pellet was 1 mg, 0.4 mg being the active material $LiCoO_2$.

This battery was the first battery to work even at room temperature since the OCV was relatively stable at 2.9394 V at room temperature and charging the battery was possible. The cycling of the battery at room temperature gave improvable results. The charge at room temperature was done with $1.25\ \mu A to 4.8V and with -0.7\mu A to 1.8V$.

For getting the specific charge, the battery was cycled at $95°C$ between 2 V and 4.8 V with $1\ \mu A and -0.5\mu A. In comparison to the other batteries, the proportion of current to active material is diff e$ $3mg the other batteries are having.$

The battery needed 2 hours to fully charge the first time at $95°C$, therefore the energy density is 5.5 mAh/g. This result is very small. One reason could be the fast charging because of the in comparison high current.

Battery 4(SRSA11P1)

The pellet for this battery was sintered at $975°C$ for 8 hours. Afterwards the pellet had a density of $3.74 g/cm^3$, which is about 73 % of the theoretical density.

Applying the slurry on top of the pellet was done in the glove box. After drying, the total amount of slurry on the pellet was 5.8 mg, 2.44 mg being the active material $LiCoO_2$.

The battery was cycled between 2 V and 4.8 V with 2.4 A and -2.4 A respectively.

The first full charge of the battery needed 11.7 hours, leading to a energy density of 11.7 mAh/g.

8. Conclusion and Outlook

In total, this work gave good results. One kind of new doping was found for LLZO and a working solid state battery was prepared. Not working were the doping wit Na and the new synthesis.

The sol–gel synthesis did not work at all. The result was the synthesis of a material which could not be identified. It could not be found if it was a single compound or more. Since the Pechini method is a derivation of this method and does work, it is likely that something in this synthesis went wrong. It is a fact that the chemicals used were old and standing open for some time. There could be changes in the chemicals which made them react different than expected. Maybe the synthesis would be a success with newer chemicals.

The Na–doped LLZO had tetragonal phase which was expected, since one necessary requirement for changing to the cubic phase is to have Li–vacancies. Sodium would only increase the lattice parameter. Since there are other ways to increase the lattice parameter and to introduce Li–vacancies, Sodium as a doping will not be very interesting.

For calcium and gallium doped LLZO, even though the material could not be produced in a pure phase, it could be seen, that calcium in a concentration of 0.2 mol per formula unit is not able to change the phase of LLZO to a cubic one. Post–doping with gallium made the phase change from the tetragonal phase to the cubic phase. The insoluble precursor Ga_2O_3 could even be added to the synthesis in the beginning, leading to a cubic faced product.

The EDX showed an even distribution of dopant gallium and calcium throughout the sample. This, together with the XRD pattern, which shows a cubic LLZO, indicates that the synthesis of the bi–doped LLZO was a success. SEM pictures showed rather big grains with impurities on the surface of the LLZO grains.

The sintering temperature of LLZO doped with gallium and calcium depends strongly on the concentration of the dopant. $Li_{6.9}Ga_{0.2}Ca_{0.5}La_{2.8}Zr_2O_{12}$ starts sintering at temperatures as low as $700°C$, while $Li_6Ga_{0.5}Ca_{0.5}La_{2.5}Zr_2O_{12}$ starts to sinter at $900°C$. Since the gallium content was the only variation, there must be a connection between gallium content and starting temperature for the sintering process. To be sure, various more concentrations of gallium should be tested.

For the material $Li_6Ga_{0.5}Ca_{0.5}La_{2.5}Zr_2O_{12}$ an Arrhenius plot was measured. The impedance was measured at different temperatures from room temperature up to $250°C$ and the data obtained was fitted with the help of an equivalent circuit. Generally the fitting was difficult because the semi–circles were not resolved. The activation energy

obtained from this measurements were 0.31 eV and 0.34 eV respectively.

From the batteries, the first battery where the pellet only had 50 % of the theoretical density was the best in terms of energy density. All the batteries were cycled at $95°C$ and worked would light a LED even after cycling. This is a big achievement, since solid state batteries in this form were not done before.

The performance is still much behind the performance of batteries with liquid electrolyte. From the impedance data measured from battery 1 it can be seen, that the interface between electrolyte and electrode has a high resistance. Much research needs to be done on this interface to understand why it is blocking exactly and how this problem can be solved. If the problem is the space–charge alone, then there is already an approach known.

Between the two cathode materials a better one could not be decided on because the performance in total was not good and the number of experiments(only four batteries) were too little. Since cobalt tends to diffuse at higher temperatures, $LiFePO_4$ will be better for high temperature applications. In addition, $LiFePO_4$ has a higher energy density than $LiCoO_2$.

Danksagung

Zum Schluss möchte ich mich bei allen bedanken, die diese Arbeit möglich gemacht haben. Es ist unmöglich, euch alle namentlich aufzuzählen. Ich hoffe trotzdem, dass ihr euch angesprochen füht.

Danke an meine Bürokollegen und die Mitarbeiter des Bereichs Electrochemie. Durch euch fühlt man sich an der Uni zu Hause. Besonderer Dank gilt dir, Sandra, weil du mir gezeigt hast wie man Elektroden baut und wie man den Aufbau richtig betreibt. Bei Günter möchte ich mich für die lehrreichen Ausführungen zur Theorie der Zyklovoltammetrie bedanken.

Danke an die Forschungsgruppe "Electrochemical Materials" der ETH Zürich, bei der ich den zweiten Teil meiner Arbeit machen durfte. Ohne euch wäre der Auslandsaufenthalt nur halb so lustig gewesen. Ihr habt mir viele interessante Einblicke rund um das Thema des keramischen Elektrolyten LLZO gegeben.

Besonderer Dank gebührt Silvia und Markus. Ihr habt mir geholfen, die Arbeit fertig zu stellen. Durch dich, Silvia, habe ich den Sprung vom Schulenglisch zum (hoffentlich) wissenschaftlichen Englisch geschafft. Danke für die Verbesserungen. Bei dir, Markus, möchte ich mich vor allem für das Kochen von unzähligen Abendessen bedanken. Man arbeitet doppelt so effizient, wenn man sich auf gutes Essen freuen kann.

Zum Abschluss möchte mich mich bei meinen Eltern bedanken. Durch euch war ein Studium überhaupt erst möglich. Danke für eure Unterstützung.

List of Figures

1.1. Domains of corrosion, immunity and passivation of copper, at 25 °C [14]. . 12
1.2. Potential–pH equilibrium diagram for the system copper–water at 25 °C. . 14

2.1. Schematic representation of a typical potential cycle between two selected potentials (E_1 and E_2). 15
2.2. Image of two self–made electrodes. 17

3.1. Tasks to be performed. 19
3.2. A characteristic .dat file opened with MATLAB's import data function . . 20
3.3. Tafel plot with raw data and smoothed data with different iN. 22
3.4. The Potential which changes linearly during the measurement. The slope between the extrema is strictly monotonic – normally a characteristic for cyclic measurements in voltammetry. 23
3.5. Raw data and fitted data measured in tap water. 27
3.6. Fitted data curve (black) with areas of regression (blue), regression lines (red) and point of intersection. Data measured in tap water. 28
3.7. Exemplary plots for tab water The plots for every single fit alone from (b) are shown in Figure 3.8. 29
3.8. The plots show the smoothed cure in the back(black), the areas used for the interpolation (blue) and the fits(red), that lead to the point of intersection. The corresponding numerical results are listed in Table 3.3 Experiment 4. 32
3.9. Exemplary plot of 0.1 M NaCl–solution treated with oxygen. The two groups of the points of intersection are clearly visible. 34
3.10. 0.1 M NaCl solution treated with oxygen. The corresponding numerical results are listed in Table 3.6 Experiment 2. 35
3.11. Examplary plot of 0.1 M NaCl–solution treated with nitrogen. The raw data of two curves is curvy on the right (anodic) branch. 37
3.12. 0.1 M NaCl solution treated with nitrogen. The corresponding numerical results are listed in Table 3.7 Experiment 3. 38
3.13. Exemplary plot for 1 M NaCl solution treated with oxygen. 41
3.14. 1 M NaCl solution treated with oxygen. The corresponding numerical results are given in Table 3.6. 42
3.15. Exemplary plot for 1 M NaCl solution treated with nitrogen. 44
3.16. 1 M NaCl solution treated with nitrogen. The corresponding numerical results are given in Table 3.6. 44
3.17. Exemplary plot for 0.1 M ascorbic acid treated with oxygen. 48

3.18. 0.1 M ascorbic acid treated with oxygen. The corresponding numerical results are given in Table 3.14. 49
3.19. Exemplary plot for 0.1 M ascorbic acid treated with nitrogen. 50
3.20. 0.1 M ascorbic acid treated with nitrogen. The corresponding numerical results are given in Table 3.15. 51
3.21. Exemplary plot for 0.1 M ZnO suspension treated with oxygen. 55
3.22. 0.1 M ZnO suspension treated with oxygen. The corresponding numerical results are given in Table 3.18. 56
3.23. Exemplary plot for 0.1 M ZnO suspension treated with nitrogen. 57
3.24. 0.1 M ZnO suspension treated with nitrogen. The corresponding numerical results are given in Table 3.19. 58
3.25. Exemplary plot for 10 mM 4–Methylimidazole–solution treated with oxygen. 63
3.26. 10 mM 4–Methylimidazole–solution treated with oxygen. The corresponding numerical results are given in Table 3.23 Experiment 1. 64
3.27. Exemplary plot for 10 mM 4–Methylimidazole–solution treated with oxygen. 65
3.28. 10 mM 4–Methylimidazole–solution treated with nitrogen. The corresponding numerical results are listed in Table 3.23 Experiment 1. 66

6.1. Theoretic principle of XRD. 78
6.2. Nyquist Plot 80

7.1. XRD of the calcined sol–gel powders and the XRD pattern of the tetragonal phase of LLZO for comparison. All patterns are normalized in intensity and the sol–gel powders and are shifted in y–direction by 0.1 a.u. for better visibility. 82
7.2. XRD of the calcined Na doped LLZO powder at two different temperatures and the XRD pattern of the tetragonal and cubic phase of LLZO for comparison. All patterns are normalized in intensity and are shifted in y–direction by 0.1 a.u. for better visibility. 84
7.3. XRD of the calcined Ca doped LLZO powder at $750°C$ and the XRD pattern of the tetragonal and cubic phase of LLZO for comparison. All patterns are normalized in intensity and are shifted in y–direction by 0.1 a.u. for better visibility. 85
7.4. XRD of the two times at $750°C$ calcined Ca doped and Ga postdoped LLZO powder and the XRD pattern of the tetragonal and cubic phase of LLZO for comparison. All patterns are normalized in intensity and are shifted in y–direction by 0.1 a.u. for better visibility. 86
7.5. XRD of the calcined Ca doped LLZO powder at $750°C$ and the XRD pattern of the tetragonal and cubic phase of LLZO for comparison. All patterns are normalized in intensity and are shifted in y–direction by 0.1 a.u. for better visibility. 87

7.6. XRD of the two times at 750°C calcined Ca doped and Ga postdoped LLZO powder and the XRD pattern of the tetragonal and cubic phase of LLZO for comparison. All patterns are normalized in intensity and are shifted in y–direction by 0.1 a.u. for better visibility. 87
7.7. XRD of the calcined $Li_{6.9}Ga_{0.2}Ca_{0.5}La_{2.8}Zr_2O_{12}$ powder at 750°C and the XRD pattern of the tetragonal and cubic phase of LLZO for comparison. All patterns are normalized in intensity and are shifted in y–direction by 0.1 a.u. for better visibility 88
7.8. Dilatometry data of a pellet of $Li_{6.9}Ga_{0.2}Ca_{0.5}La_{2.8}Zr_2O_{12}$. The powder for the dilatormatry was pressed from powder calcined at 650°C. 89
7.9. XRD of the sintered $Li_6Ga_{0.5}Ca_{0.5}La_{2.5}Zr_2O_{12}$ powder at 925°C and the XRD pattern of the tetragonal and cubic phase of LLZO for comparison. All patterns are normalized in intensity and are shifted in y–direction by 0.1 a.u. for better visibility. 90
7.10. EDX of the calcined $Li_6Ga_{0.5}Ca_{0.5}La_{2.5}Zr_2O_{12}$ powder. 90
7.11. SEM of the calcined $Li_6Ga_{0.5}Ca_{0.5}La_{2.5}Zr_2O_{12}$ powder. 91
7.12. Dilatometry data of a pellet of $Li_{6.9}Ga_{0.2}Ca_{0.5}La_{2.8}Zr_2O_{12}$. The powder for the dilatormatry was pressed from powder calcined at 765°C. 93
7.13. Circuit used for fitting the impedance data. 93
7.14. Arrhenius plot from a pellet made out of $Li_6Ga_{0.5}Ca_{0.5}La_{2.5}Zr_2O_{12}$. The bulk resistance $R1$ was used for calculation. 94
7.15. Examplary XRD of the sintered powder. 95
7.16. Cell used for assembly of the battery. 97
7.17. First cycle of the battery at 95°C. 98
7.18. Impedance result measured at 95°C. 99
7.19. SEM picture of the pellet after cycling in the battery. 100
7.20. Potential(vs. Li/Li^+) against specific charge. 101
7.21. Picture of pellet with composite after heating. The composite was applied to the side not visible in the picture. 102

List of Tables

1.1. Some standard electrode potentials at 25 °C (part of table in [4, p.77]) . . 11

3.1. Mean values for x_POI and y_POI for nitrogen treated tap water. 31
3.2. Mean values for x_POI and y_POI for oxygen treated tap water. 31
3.3. Results for tap water as electrolyte. k, d and COD for the fits and x and y of the POI are given. 33
3.4. Mean values for x_POI and y_POI for oxygen treated 0.1 M NaCl–solution. 36
3.5. Mean values for x_POI and y_POI for nitrogen treated 0.1 M NaCl–solution. 36
3.6. The results of the measurement with electrolyte being 0.1 M NaCl in water treated with oxygen. One point of intersection in the first paragraph was not found. 39
3.7. The results of the measurement with electrolyte being 0.1 M NaCl in water treated with nitrogen. One point of intersection in the first paragraph was not found. 40
3.8. Mean values for x_POI and y_POI for oxygen treated 1 M NaCl–solution. . 43
3.9. Mean values for x_POI and y_POI for nitrogen treated 1 M NaCl–solution. 43
3.10. The numerical results of the data measured with an electrolyte of 1 M NaCl in water treated with oxygen. One point of intersection in the first paragraph was not found. 45
3.11. The numerical results of the data measured with an electrolyte of 1 M NaCl in water treated with oxygen. One point of intersection in the first paragraph was not found. 46
3.12. Mean values for x_POI and y_POI for oxygen treated 0.1 M ascorbic acid solution. 48
3.13. Mean values for x_POI and y_POI for nitrogen treated 0.1 M ascorbic acid solution. 50
3.14. Numerical results of the 0.1 M ascorbic acid solution treated with oxygen. 52
3.15. Numerical results of the 0.1 M ascorbic acid solution treated with nitrogen. 53
3.16. Mean values for x_POI and y_POI for oxygen treated ZnO suspension. . . . 55
3.17. Mean values for x_POI and y_POI for nitrogen treated ZnO suspension. . . 57
3.18. Numerical results of the 0.1 M ZnO suspension treated with oxygen. . . . 59
3.19. Numerical results of the 0.1 M ZnO suspension treated with nitrogen. . . 60
3.20. Mean values for x_POI and y_POI for oxygen treated 4–Methylimidazole solution. 62
3.21. Mean values for x_POI and y_POI for nitrogen treated 4–Methylimidazole solution. 62

3.22. Numerical results of the 10 mM 4–Methylimidazole–solution treated with oxygen. 67
3.23. Numerical results of the 10 mM 4–Methylimidazole–solution treated with nitrogen. 68

7.1. Data of the Arrhenius plot. 92

Bibliography

[1] E. Wiberg A.F. Hollenan and N. Wiberg. *Lehrbuch der Anorganischen Chemie*. Walter de Guyer Co., 2007.

[2] Richard Beatty. *Copper*. The elements. Marshall Cavendish Corporation, New York, 2001.

[3] Jeff Doebrich. Fact sheet 2009-3031 copper. Factsheet of U.S. Department of the Interior and U.S. Geological Survey, May 2009.

[4] David E.J. Talbot and James D.R. Talbot. *Corrosion Science and Technology*. CRC Press Taylor Francis Group, Boca Raton, 2nd edition edition, 2007.

[5] R.S. Goncalves A. Spinelli F.S. de Souza, C.Giacomelli. Adsorption behaviour of caffeine as a green corrosion inhibitor for copper. *Materials Science and Engineering C*, 32:2436–2444, 2012.

[6] X.M. He L.-X. Gao D.-Q. Zhang, Q.-R. Cai and G.S. Kim. Corrosion inhibition and adsorption behavior of methionine on copper in hcl and synergistic effect of zinc ions. *Material Chemistry and Physics*, 114:612–617, 2009.

[7] X.M. He L.-X. Gao D.-Q. Zhang, Q.-R. Cai and G.D. Zhou. Inhibition effect of some amino acids on copper corrosion in hcl solution. *Materials Chemistry and Physics*, 112:353–358, 2008.

[8] Richard G. Compton and Craig E. Banks. *Understanding Voltammetry*. Imperial Collage Press, London, 2nd edition edition, 2011.

[9] Helmut Kaesche. *Die Korrosion der Metalle*. Springer-Verlag, Berlin Heidelberg, 3. auflage (nachdruck) edition, 2011.

[10] P.W. Atkins and J. de Paula. *Kurzlehrbuch Physikalische Chemie*. WILEY–VCH Verlag GmbH Co. KGaA, 2008.

[11] G. Wedler. *Lehrbuch der Physikalischen Chemie*. WILEY–VCH Verlag GmbH Co. KGaA, 2004.

[12] Carl H. Hamann and Wolf Vilstich. *Elektrochemie*. WILEY-VCH Verlag GmbH Co. KGaA, Weinheim, 4., vollständig überarbeitete und aktualisierte auflage edition, 2005.

[13] Wikipedia. Chemical potential. `http://en.wikipedia.org/wiki/Chemical_potential`, Acsessed on 22.01.2015.

[14] M. Pourbaix. *Atlas of Electrochemical Equilibria in Aqueous Solutions*, chapter IV Copper. National Association of Corrosion Engineers, 1974.

[15] w. Allertshammer P. Linhardt. Korrosion. Lecture Notes (VO 308.880, WS 2014/15).

[16] Python. Python documentation. `https://www.python.org/doc/`, Acsessed on 22.01.2015.

[17] D. Louis. *Programmieren LErnen mit Visual C# 2013*. O'Reilly Verlag GmbH Co. KG, 2014.

[18] R. Salghi M. Mihit B. Hammouti A. Albourine S. El Issami K. Barouni, L. Bazzi. Some amino acids as corrosion inhibitors for copper in nitric acid solution. *Materials Letters*, 62:3325–3327, 2008.

[19] M.M. Antonijevic and M.B. Petrovic. Copper corrosion inhibitors. a review. *Int. J. Electrochem. Sci.*, (3):1–28, 2008.

[20] I.M. Ghayad R.M. Abdullah F.M.Al Kharafi, N.A. Al-Awadi and M.R. Ibrahim. Corrosion protection of copper using azoles applied on its surface at high temperature under vacuum. *Int. J. Electrochem. Sci.*, (6):1562–1571, 2011.

[21] A.P.I. Popoola and O.S.I.Fayomi. Zno as corrosiom inhibitor for dissolution of zinc electrodeposited mild steel in varying hcl concentration. *International Journal of the Physical Sciences*, 2011.

[22] R. Winston Revie and Herbert H. Uhlig. *Corrosion and Corrosion Control*. WILEY-INTERSCIENCE John Wiley Sons, Inc., Publication, New Jersey, 4th edition edition, 2008.

[23] Wikipedia. Energy crisis. `http://en.wikipedia.org/wiki/Energy_crisis`, 2015.

[24] T.S. Murty M.L. Khandekar and P. Chittibabu. The global warming debate: A review of the state of science. *Pure and Applied Geophysics*, (162):1557–1586, 2005.

[25] K. Ide H. Yamasaki T. Kato T. Saito F. Sagane C. Yada, A. Ohmori and Y. Iriyama. Dielectric modifi cation of 5v–class cathodes for high–voltage all–solid–state lithium batteries. *Advanced Energy Materials*, 4:1301416, 2014.

[26] Royal Society of Chemistry. Periodic table: Lithium. `http://www.rsc.org/periodic-table/element/3/lithium`, 2015.

[27] J.-M. Tatascon and M.Armand. Issues and challenges facing rechargabe lithium batteries. *Nature*, 414:359–367, 2001.

[28] *Intercalation Compounds for Battery Materials*, chapter 25 Years of Intercalation Chemistry for Battery Materials, pages 21–28. Electrochemical Society, Inc., 2000.

[29] J.-K. Park, editor. *Principles and Applications of Lithium Secondary Batteries*, chapter 3.1.1 Development History of Cathode Materials. Wiley–VCH Verlag Co.KGaA, 2012.

[30] D.W. Shin J.-W. Choi D.-S. Paik A. Patil, V. Patil and S.-J. Yoon. Issue and chalanges facing rechargable thin film lithium batteries. *Materials Research Bulletin*, 43:1913–1942, 2008.

[31] M.S.Whittingham. Lithium batteries and cathode materials. *Cem.Rev.*, 104:4271–4301, 2004.

[32] C. Sequeira and D. Santos, editors. *Polymer electrolytes Fundamentals and applications*, chapter 1.2.1 Lithium polymer electrolytes. Woodhead Publishing Limited, 2010.

[33] R. Korthauer, editor. *Handbuch Lithium–Ionen–Batterien*, chapter 2 Übersicht zu Lithium–Ionen–Batterien. Springer Verlag, 2013.

[34] I. Belharouak, editor. *Lithium Ion Batteries – New Developments*, chapter 5 New Developments in Solid Electrolytes for Thin–Film Lithium Bateries. InTech, 2012.

[35] J.M.Tarascon and M. Armand. Issues and challenges facing recharchable lithium batteries. *Nature*, 414(15):359–367, 2001.

[36] K.C. Kam and M.M. Doeff. Electrode materials for lithium ion batteries. *Material Matters*, 7(4), 2012.

[37] S. Narayanan V. Thangadurai and D. Pinzaru. Garnet–type solid–state fast li ion conductors for li batteries: critical review. *Chem. Soc. Rev.*, 43:4714, 2014.

[38] S. Berendts A. Kuhn P. Bottke-M. Wlikening P. Heitjans A. Senyshyn H. Ehrenberg A. Lotnyk V. Duppel L. Kienle H. Bushmann, J. Dölle and J. Janek. Structure and dynamics of the fast lithium ion conductor $li_7la_3zr_2o_{12}$. *Phys.Chem.Chem.Phys.*, 13:19378–19392, 2011.

[39] J. Wolfenstine E. Rangasamy and J. Sakamoto. The role of al and li concentration on the formation of cubic garnet solid electrolyte of nominal composition $li_7la_3zr_2o_{12}$. *Solid State Ionics*, 2011.

[40] J.M.L. del Amo A. Aquadero F. Aquesse C. Bernuy-Lopez, W. Manalastas Jr. and J.A. Kilner. Atmosphere controlled processing of ga–substituded garnets for high li–ion conductivity ceramics. *Chem. of Mater.*, 2014.

[41] F. Krumeich S. Afyon and L.M. Rupp. A shortcut to garnet–type fast li–ion conductors for all solid state batteries. *Journal of Materials Chemistry A*, 2015.

[42] H.E. Shinawi and J. Janek. Stabilization of cubic lithium-stuffed garnets of the type "$li_7la_3zr_2o_{12}$" by addition of gallium. *Journal of Power Sources*, 225:13–19, 2013.

[43] E. Kendrick K.S. Knight D.C. Anderson M.A. Howard, O. Clemens and P.R. Slater. Effect of ga incorporation on the structure and li ion conductivity of $la_3zr_2li_7o_{12}$. *Dalton Trans.*, 41, 2012.

[44] B. Lopez-Bermudez K. Page W.G. Zeier, S. Zhou and B.C. Melot. Dependence of the li–ion conductivity and activation energies on the crystal structure and radii in $li_6mla_2ta_2o_{12}$. *Applied Materials and Interfaces*, 2014.

[45] M. Tribus-P. Tropper D. Rettenwander, C.A. Geiger and G. Amthauer. A synthesis amd crystal chemical study of the fast ion conductor $li_{7-3x}ga_xla_3zr_2o_{12}$. *Inorganic Chemistry*, 2014.

[46] N. Bernstein and M.D. Johannes. Origin of the structural phase transition in $li_7la_3zr_2o_{12}$. *Phys.Rev.Lett,*, 109, 2012.

[47] H. Kim-Y. Kim J. Sakamoto, E. Rangasamy and J. Wolfenstine. Synthesis of nano–scale fast ion conducting $li_7la_3zr_2o_{12}$. *Nanotechnology*, 24, 2013.